

PE&RS

January 2020

Volume 35, Number 1

PHOTOGRAMMETRIC ENGINEERING & REMOTE SENSING The official journal for imaging and geospatial information science and technology

QUEENSLAND

■ Gold Coast

NEW
SOUTH
WALES

■ Coffs Harbour

■ Port Macquarie

■ Newcastle

■ Sydney

GEO WEEK 2020

Washington, DC | March 23-25, 2020
<http://conferences.asprs.org/geoweek-2020/>

WORKSHOP ANNOUNCEMENT

March 23, 2019

Streamlined Photorealistic Textured Mesh and True Orthophoto Generation from Aerial Imagery

Thomas Widmer, Trimble and Mohsen Miri, Trimble

Highly accurate 3D meshes provide virtual navigation of real-world environments in desktop and web platforms. These products are used in city modeling, construction and simulation purposes. Modeling of 3D surfaces with sharp edges and high quality textured meshes can be performed in a modern and precise methods. These meshes can be used to produce true orthophotos, simplifying planimetric mapping and the overlay of other GIS data, especially in urban mapping applications. This workshop will explore the methods used to create these products using Trimble INPHO MATCH-3DX software.

Digital Aerial Triangulation using Imagery from Multi-Head Systems

Mohsen Miri, Trimble and Thomas Widmer, Trimble

Current aerial mapping technologies lead to capturing a large number of images, not only at nadir but also in oblique viewing directions. The number and variety of multi-head oblique platforms available on the market is continuously growing. This workshop presents a stable and simplified workflow for the complex multi-head imagery for higher production efficiencies. This workshop will explore the workflow and the matching strategies for such systems using Trimble INPHO MATCH-AT software.

Best Practices for Managing, Editing, Visualizing, and Sharing Lidar in 2D and 3D

Nicholas Giner, Esri and Lindsay Weitz, Esri

Although lidar data has been collected and processed for over 20 years, the global lidar market continues to rapidly expand as demand for 3D imagery in consumer, commercial, and government applications increases. Federal, state, and local government agencies are acquiring lidar data for use in applications such as floodplain mapping, urban planning and design, resource and environmental management, law enforcement, natural resource exploration, archeology, and emergency response. This session will teach best practices for working with Light Detection and Ranging (lidar) data. Attendees of this session will learn lidar basics and fundamentals, as well as the best practices for managing, editing, visualizing, and sharing it in 2D and 3D. Attendees will also learn several workflows for deriving useful information products from lidar data, as well as performing 2D and 3D analysis on lidar-derived products.

Using USGS/ASPRS Data Quality Measure (DM) Software for Validation of Airborne Lidar Point Clouds

Barry Miller, USGS and Ajit Sampath, USGS

This workshop provides an in-depth look at the USGS/ASPRS Data Quality Measure (DQM) software. DQM provides an ability to determine the relative accuracy, or geometric quality, of overlapping swaths of lidar point clouds using a point-to-plane measurement technique. DQM calculates vertical and horizontal differences between swaths in a point cloud tile, which allows better analysis of the quality of a lidar project. Attendees will see a demonstration on how to use the tool and interpret the results with several real-world examples. The workshop will also show how to obtain the software, which is a government-furnished freeware for public use.

UAS Lidar for Precision Mapping

Mohamed Mostafa, Microdrones Canada Inc.

Professional grade lidar systems are currently being used onboard unmanned aerial systems for high precision mapping applications. This workshop is intended for the unmanned airborne lidar user community including mapping professionals, land surveyors, managers, and decision makers to understand the underlying concepts of lidar from the technical and business perspective, in the form of theory and practice, using real data sets from around the world.

Fundamentals of Image Analysis in Google Earth Engine

Ge (Jeff) Pu, SUNY-ESF

Cloud-based image processing platforms like the Google Earth Engine (GEE) bring unprecedented possibilities for education, research, and outreach. This workshop will focus on an interactive exploration of GEE capabilities, the repository of all of publicly available aerial and satellite data, and user upload of imagery for analysis. The workshop will begin with a presentation of examples of GEE projects with a focus on education, undergraduate research, and outreach followed by hands-activities.

Preparation for ASPRS Certification – Lidar

Karen Schuckman, Penn State University

This workshop provides an in-depth review of content contained in the ASPRS Airborne Topographic Lidar Manual. It is valuable for those planning to take the examination for ASPRS Certified Mapping Scientist-Lidar, Certified Technologist-Lidar, or Intern. Workshop participants will answer practice questions and discuss answers in an interactive session. The workshop is also valuable for practitioners wishing to further their mastery of the theory and practice of topographic mapping with lidar.

Practical Approach to Using the ASPRS Positional Accuracy Standards for Digital Geospatial Data

Qassim Abdullah, Woolpert, Inc. and

Claire Kiedrowski, Cornerstone Energy Services, Inc.

This workshop provides an in-depth look at the ASPRS Positional Accuracy Standards to categorize positional accuracy of products derived from digital aerial cameras, manned and unmanned aerial systems, and all types of lidar including terrestrial, mobile, and airborne. The workshop will explain the basis for each accuracy measure adopted in the standards. Instructors will demonstrate practical application of these standards. Attendees will apply these standards to real-world examples.

Object Based Image Analysis Made Easy and Flexible

Keith Peterson, Trimble, and

Jarlath O'Neil-Dunne, University of Vermont

This workshop will provide an informative introduction to the fundamental concepts and technologies in object-based image analysis and its combination with computer vision methods, machine-learning and pixel-based operations. Attendees will use eCognition Developer to employ a comprehensive range of analysis tools utilizing diverse data sources, from medium to high resolution satellite data, very high-resolution aerial and UAV imagery, GIS, lidar, radar, and even hyperspectral data.

Combining Deep Learning with Object Based Image Analysis (OBIA)

Keith Peterson, Trimble, and Christian Weise, Trimble

Recently, deep learning (DL) has become the fastest growing trend in data analysis and has been widely and successfully applied to various feature extraction tasks. In the context of remote sensing the combination of DL with OBIA (object-based image analysis) offers the flexibility to select the optimal working method inside the complete feature extraction workflow. This workshop will explore the accelerated usage of deep learning with object-based image analysis using Trimble eCognition Developer software.

Spreadsheet Demonstration of Analytical Photogrammetry

Paul Pope, Global Geoinformatics Inc.

Photogrammetry is often explained by describing the collinearity condition and showing examples of final products. The intermediate steps are rarely illustrated in detail. This workshop aims to make analytical photogrammetry accessible to the layperson by using spreadsheet calculations to 1) solve for the exterior orientation parameters of a framing camera, and 2) determine the dimensions of an object using stereo imagery.

Generic Sensor Models for Photogrammetric Applications

Henry Theiss, Integrity Applications Incorporated

The workshop conveys the importance of rigorous sensor modeling, data adjustment, and covariance propagation in meeting the absolute geolocation, relative mensuration, and multi-sensor fusion objectives of the end-user. It proceeds with an overview of the Community Sensor Model (CSM) Application Programming Interface (API) which facilitates integration of multi-modality imagery and point-cloud products into geospatial exploitation tools. It provides an overview of generic sensor models for frame-sequences, linear-array scanners, SAR, and lidar.”

Total Propagated Uncertainty (TPU) and Absolute Accuracy Assessment of 3D Lidar Point Cloud

Minsu Kim, USGS

Total Propagated Uncertainty (TPU) is the statistical estimate of lidar positional uncertainty for each lidar point. Theoretical details of the TPU and its application to the airborne lidar data will be presented. Assessment of the 3D absolute accuracy of the lidar point cloud is an important priority in USGS 3DEP program. TPU is an important factor that affects the absolute accuracy of the lidar point cloud data. Techniques for the 3D absolute accuracy assessment using various geometric features and its inherent relationship with TPU will be discussed in the workshop.

Machine and Deep Learning Image Classification

Amr Abd-Elrahman, University of Florida

This workshop teaches participants how to (1) conduct pixel- and object-based image classification using traditional (Support Vector Machine and Random Forests) machine learning algorithms; (2) build models for data preparation and experiment with different classification parameters; (3) use the deeplab deep learning architecture for image segmentation (classification). Participants will be briefly introduced to necessary theoretical background information as well as practical implementation using ArcGIS Pro. Real world examples of wetland land cover classification will be used in the demonstration.

Preparation for ASPRS Certification

- General Knowledge

Robert Burtch, Ferris State University

This workshop covers the common knowledge areas comprising a large portion of exam content for ASPRS Certification. It is valuable preparation for those who have never taken an ASPRS exam, as well as for those who have expertise in a particular specialty, such as lidar or UAS, but feel less prepared for the general knowledge component of the exam. This workshop will also explain the certification application process and the importance of certification in career development.

Aerial Triangulation and Data Processing for the Unmanned Aerial System (UAS)

Qassim A Abdullah, Woolpert, Inc. and

Riadh Munjy, CSU Fresno

This workshop teaches participants to successfully design, plan and execute an aerial mission using unmanned aerial systems (UAS) and GPS-based aerial triangulation, including flight planning, ground control placement, camera calibration, and product generation. Participants will be introduced to mathematical basis of simultaneous bundle block adjustment. Practical examples will be presented.

REGISTER FOR WORKSHOPS ON THE CONFERENCE REGISTRATION SITE!

If you have already registered for the conference and wish to add a workshop, call 508-743-8501.

If you wish to register for a workshop without registering for the conference, call 508-743-8501.

For additional information, see

<http://conferences.asprs.org/geoweek-2020/> or contact programs@asprs.org



EQUIPMENT

DARWin SP Data Acquisition software adds first and second derivatives capabilities — DARWin SP Data Acquisition software is included with every **SPECTRAL EVOLUTION** spectrometer and spectroradiometer. The software controls the instruments and provides additional capabilities via pull down menus. Now, DARWin SP Data Acquisition software offers first and second derivatives calculations.

Derivatives are typically used as signal pre-treatments applied to spectra data. They help to resolve peak overlap, enhance resolution of spectral features and eliminate noise & spectral drift between samples. DARWin SP features one-touch operation and easy, intuitive menus for fast, effortless operation. In addition to derivatives, DARWin SP also offers easy access to 19 vegetation indices, mineral reflectance, solar simulation, colorimetry, and energy measurement.

For more information on DARWin derivatives, visit: <https://spectralevolution.com/products/software/software-applications>.

CALENDAR

- 9-11 February 2020, **CALGIS**, Long Beach, California. For more information, visit <https://www.urisa.org/calgis>.
- 10-12 February 2020, **ESRI Federal GIS Conference**, Washington DC. For more information, visit: <https://www.esri.com/en-us/about/events/federal-gis-conference/overview>
- 23-25 March 2020, **Geo Week**, Washington, DC. For more information, visit <https://www.lidarmap.org/geoweek/>.
- 7-9 May 2020, **GISTAM 2020—6th International Conference on Geographical Information Systems Theory, Applications and Management**, Prague, Czech Republic. For more information, visit: <http://www.gistam.org/>.
- 20-22 May 2020, **AutoCarto 2020—the 23rd International Research Symposium on Computer-based Cartography**, Redlands, California. For more information, visit <https://cartogis.org/autocarto/>.
- 15-22 August 2020, **43rd COSPAR Scientific Assembly**, Sydney, Australia. For more information, visit <https://www.cospar-assembly.org/>.

EVENTS

The California **URISA** Chapters and the California Geographic Information Association (CGIA) are pleased to announce that registration is open for CalGIS 2020, taking place February 9-11, 2020 at the Hilton Long Beach.

CalGIS is honored to announce that Governor Martin O'Malley will be the opening keynote speaker! Attendees may purchase Governor O'Malley's "Smarter Government: How to Govern for Results in the Information Age" from Esri Press at a discounted price when they register, and get it signed at CalGIS 2020.

The complete program is detailed online at <https://calgis2020.sched.com/>.

International Lidar Mapping Forum Announces 2020 Conference Program — The **International Lidar Mapping Forum (ILMF)** has released its 2020 conference program featuring a robust and diverse lineup of keynote presentations, case studies, and panel discussions lead by industry experts. This year marks the 20th anniversary of ILMF, the premier event for surveying and mapping technologies including airborne, mobile, and bathymetric lidar as well as other remote sensing technologies.

The 2020 conference, the first to take place in Washington, DC, will feature heavy representation from government organizations that employ surveying and mapping technologies. These presentations will explore topics such as national mapping programs, statewide projects, updates from the U.S. Geological Survey (USGS), and the 3D Elevation Program (3DEP). The program will also cover a wide array of specific areas of application such as topo-bathy mapping, forestry, indoor mapping, and much more.

The 20th edition of International Lidar Mapping Forum (ILMF), produced by Diversified Communications, will be held from March 23-25 at the Walter E. Washington Convention Center in Washington, DC. It will take place together with the ASPRS Annual Conference and the MAPPs Federal Programs Conference, as part of Geo Week. The conference is critical to anyone who needs to stay on top of the latest technology and developments in the rapidly changing geospatial technology market.

Registration for 2020 International Lidar Mapping Forum is now open.

URISA and the International Association of Assessing Officers (IAAO) are pleased to announce the program details for the 2020 GIS/Valuation Technologies Conference in Louisville, Kentucky, March 23-26. Formerly known as GIS/CAMA, the event has been re-branded to take into account the abundance of technologies that, when integrated with GIS, make valuation and assessment more accurate, efficient and applicable for jurisdictions of all sizes. For more than twenty years, the organizations have hosted a conference to discuss the importance of data and the analysis of location information for better decision-making within a jurisdiction.

For more information, visit <https://gisvaltech2020.sched.com/>.

Be a part of ASPRS Social Media:



facebook.com/ASPRS.org



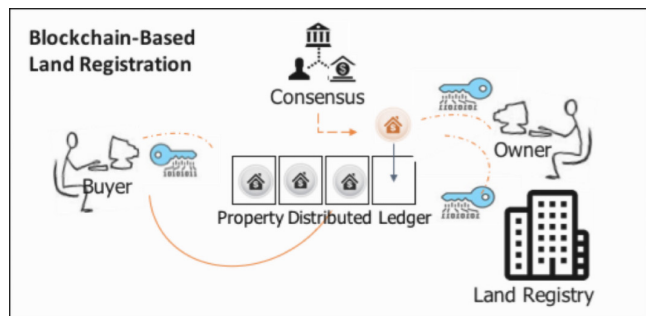
linkedin.com/groups/2745128/profile



twitter.com/ASPRsOrg



youtube.com/user/ASPRS



5 Blockchain Applications in Geographical Information Systems

Arif Furkan Mendi and Alper Çabuk

PEER-REVIEWED ARTICLES

17 Application of PCA Analysis and QR Decomposition to Address RFM's Ill-Posedness

Amin Alizadeh Naeini, Sayyed Hamed Alizadeh Moghaddam, Mohammad Moein Sheikholeslami, and AliReza Amiri-Simkooei

Rational function model (RFM) is the most widely used sensor model in the remote sensing community. However, it suffers from ill-posedness, challenging its feasibility. This problem is mainly caused due to highly correlated coefficients of the RFM, which magnifies any small perturbations of observations, such as noise and instrumental error. This paper outlines a novel two-step method, called principal component analysis (PCA)-RFM, based on the integration of PCA and QR decomposition.

23 3D Iterative Spatiotemporal Filtering for Classification of Multitemporal Satellite Data Sets

Hessah Albanwan, Rongjun Qin, Xiaohu Lu, Mao Li, Desheng Liu, and Jean-Michel Guldmann

The current practice in land cover/land use change analysis relies heavily on the individually classified maps of the multi-temporal data set. Due to varying acquisition conditions (e.g., illumination, sensors, seasonal differences), the classification maps yielded are often inconsistent through time for robust statistical analysis. 3D geometric features have been shown to be stable for assessing differences across the temporal data set. In this article, the use of a multi-temporal orthophoto and digital surface model derived from satellite data for spatiotemporal classification is investigated.

33 Robust Pose Estimation and Calibration of Catadioptric Cameras with Spherical Mirrors

Sagi Filin, Grigory Ilizirov, and Bashar Elnashef

Catadioptric cameras broaden the field of view and reveal otherwise occluded object parts. They differ geometrically from central-perspective cameras because of light reflection from the mirror surface. To handle these effects, a new pose-estimation and reconstruction models for imaging through spherical mirrors is presented. A closed-form equivalent to the collinearity principle via which three methods are established to estimate the system parameters: a resection-based one, a trilateration-based one that introduces novel constraints that enhance accuracy, and a direct and linear transform-based one is derived.



45 Preview of the Manual of Remote Sensing 4th Ed.

COLUMNS

- 11 GIS Tips & Tricks
- 13 Book Review – *LiDAR Remote Sensing and Applications*

ANNOUNCEMENTS

- 1 Geo Week 2020 — ASPRS Workshops Announced
- 15 New ASPRS Members
Join us in welcoming our newest members to ASPRS.
- 15 Headquarters News

DEPARTMENTS

- 2 Industry News
- 2 Calendar
- 22 Who's Who in ASPRS
- 32 ASPRS Media Kit

See the Cover Description on Page 4

COVER DESCRIPTION



Three weeks into November 2019, springtime bush fires continued to blaze across southern and eastern Australian states. As of November 20, government agencies counted 45 fires in South Australia and 49 in New South Wales, and dangerously dry and windy weather was fanning flames in Victoria and Queensland.

The fires have sent smoke rising high into the atmosphere and half-way around the world, with satellites detecting aerosols and other smoky pollutants crossing the Pacific and moving over the South Atlantic Ocean. Locally, the smoke has blanketed the Sydney metropolitan area, significantly degrading air quality.

On November 19, 2019, the Moderate Resolution Imaging Spectroradiometer (MODIS) on NASA's Aqua satellite acquired a natural-color image (cover image) of thick smoke plumes rising from New South Wales (NSW) and Queensland.

According to researchers, the smoke plumes from the Australian fires have risen as high as 12 to 13 kilometers (7 to 8 miles) in the atmosphere. That is unusually high for wildfires. "This event is interesting because we still don't have a confirmed pyrocumulonimbus cloud to explain the lofting," said Mike Fromm, a fire researcher at the U.S. Naval Research Laboratory. "In spite of this being a well-observed plume event, it is still not clear how so much smoke got so high so fast."

As wildfires consume wood, vegetation, homes, and other materials, they emit many gases and particles, including carbon monoxide, carbon dioxide, hydrocarbons, nitrogen oxides, organic carbon, and fine particulate matter (PM2.5). Black carbon is a type of aerosol that is especially harmful to humans and animals because the particles are small enough to enter the lungs and bloodstream.

When such pollutants rise high into the atmosphere, their effects can spread across oceans and continents and can linger for weeks to months. Beyond health effects on the ground, black carbon and other debris can darken snow and ice, accelerating melting. In the atmosphere, the particles and gases can absorb or block sunlight, affect cloud formation, and increase or reduce rainfall. When lofted in great quantities, smoke plumes might have an impact on climate.

"Events like these are like natural experiments to study atmospheric air mass movements," said Santiago Gasso of NASA's Goddard Space Flight Center. "Like a volcanic eruption, there is so much material in these smoke plumes that you can track the air for thousands of kilometers. It is like releasing a tracer and following where it goes over the South Pacific, an area that is notoriously under-observed."

Occasionally, smoke even causes odd problems for pilots. "Dense smoke far from its source can create problems, especially if it is encountered without knowing what it is," said Fromm. "For instance, airliners have occasionally made emergency landings because smoke outside was detected inside the aircraft."

At 12:25 Universal Time (11:25 p.m. local time) on November 17, the Operational Land Imager on Landsat 8 acquired this nighttime image of fires raging near Port Macquarie, New South Wales. The image, pictured above, was made from a combination of shortwave and near-infrared data (bands 7-6-5) to reveal hot spots through the smoke and clouds. The infrared data is overlaid on a base map created with imagery from before the fires began.

For more information and to view the animation that depicts the abundance and direction of black carbon blowing through the atmosphere from November 1-18, visit <https://landsat.visibleearth.nasa.gov/view.php?id=145898>.

NASA Earth Observatory images and video by Joshua Stevens, using GEOS-5 data from the Global Modeling and Assimilation Office at NASA GSFC, MODIS data from NASA EOSDIS/LANCE and GIBS/Worldview, and Landsat data from the U.S. Geological Survey. Story by Michael Carlowicz and Adam Voiland.



PHOTOGRAMMETRIC ENGINEERING & REMOTE SENSING

JOURNAL STAFF

Publisher ASPRS
Editor-In-Chief Alper Yilmaz
Assistant Editor Jie Shan
Assistant Director — Publications Rae Kelley
Electronic Publications Manager/Graphic Artist
Matthew Austin

Photogrammetric Engineering & Remote Sensing is the official journal of the American Society for Photogrammetry and Remote Sensing. It is devoted to the exchange of ideas and information about the applications of photogrammetry, remote sensing, and geographic information systems. The technical activities of the Society are conducted through the following Technical Divisions: Geographic Information Systems, Photogrammetric Applications, Lidar, Primary Data Acquisition, Professional Practice, and Remote Sensing Applications. Additional information on the functioning of the Technical Divisions and the Society can be found in the Yearbook issue of *PE&RS*.

Correspondence relating to all business and editorial matters pertaining to this and other Society publications should be directed to the American Society for Photogrammetry and Remote Sensing, 425 Barlow Place, Suite 210, Bethesda, Maryland 20814-2144, including inquiries, memberships, back issues, changes in address, manuscripts for publication, advertising, subscriptions, and publications. The telephone number of the Society Headquarters is 301-493-0290; the fax number is 225-408-4422; web address is www.asprs.org.

PE&RS. *PE&RS* (ISSN0099-1112) is published monthly by the American Society for Photogrammetry and Remote Sensing, 425 Barlow Place, Suite 210, Bethesda, Maryland 20814-2144. Periodicals postage paid at Bethesda, Maryland and at additional mailing offices.

SUBSCRIPTION. For the 2020 subscription year, ASPRS is offering two options to our *PE&RS* subscribers — an e-Subscription and the print edition. E-subscribers can plus-up their subscriptions with printed copies for a small additional charge. Print and Electronic subscriptions are on a calendar-year basis that runs from January through December. We recommend that customers who choose both e-Subscription and print (e-Subscription + Print) renew on a calendar-year basis.

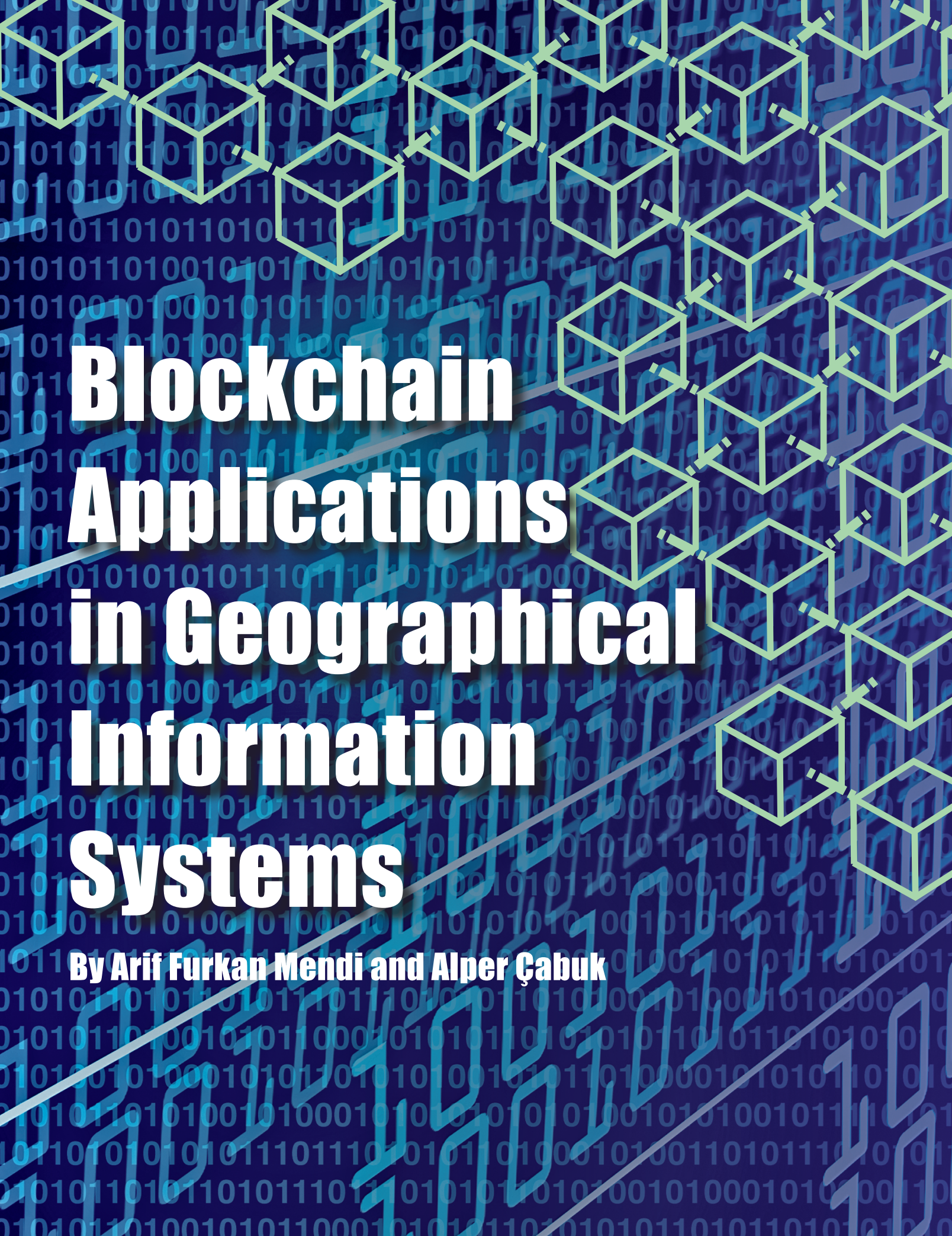
The rate of the e-Subscription (digital) Site License Only for USA and Non-USA is \$1000.00 USD. e-Subscription (digital) Site License Only for Canada* is \$1049.00 USD. e-Subscription (digital) Plus Print for USA is \$1365.00 USD. e-Subscription (digital) Plus Print for Canada* is \$1424.00 USD. e-Subscription (digital) Plus Print for Non-USA is \$1395.00 USD. Printed-Subscription Only for USA is \$1065.00 USD. Printed-Subscription Only for Canada* is \$1124.00 USD. Printed-Subscription Only for Non-USA is \$1195.00 USD. *Note: e-Subscription/Printed-Subscription Only/e-Subscription Plus Print for Canada include 5% of the total amount for Canada's Goods and Services Tax (GST #135123065). **PLEASE NOTE: All Subscription Agencies receive a 20.00 USD discount.**

POSTMASTER. Send address changes to *PE&RS*, ASPRS Headquarters, 425 Barlow Place, Suite 210, Bethesda, Maryland 20814-2144. CDN CPM #40020812

MEMBERSHIP. Membership is open to any person actively engaged in the practice of photogrammetry, photointerpretation, remote sensing and geographic information systems; or who by means of education or profession is interested in the application or development of these arts and sciences. Membership is for one year, with renewal based on the anniversary date of the month joined. Membership Dues include a 12-month electronic subscription to *PE&RS*. Or you can receive the print copy of *PE&RS* Journal which is available to all member types for an additional fee of \$60.00 USD for shipping USA, \$65.00 USD for Canada, or \$75.00 USD for international shipping. Dues for ASPRS Members outside of the U.S. will now be the same as for members residing in the U.S. Annual dues for Regular members (Active Member) is \$150.00 USD; for Student members \$50.00 USD for USA and Canada \$58.00 USD; \$60.00 USD for Other Foreign members. A tax of 5% for Canada's Goods and Service Tax (GST #135123065) is applied to all members residing in Canada.

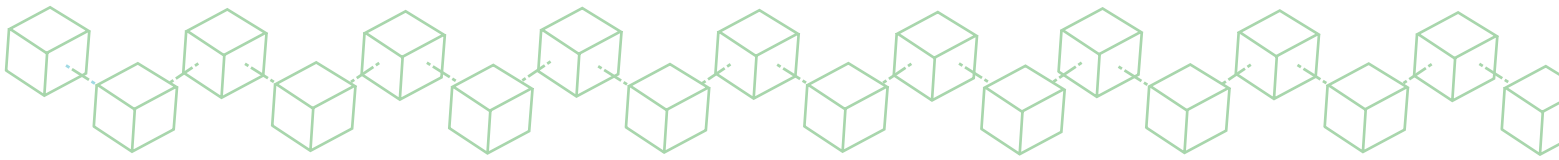
COPYRIGHT 2020. Copyright by the American Society for Photogrammetry and Remote Sensing. Reproduction of this issue or any part thereof (except short quotations for use in preparing technical and scientific papers) may be made only after obtaining the specific approval of the Managing Editor. The Society is not responsible for any statements made or opinions expressed in technical papers, advertisements, or other portions of this publication. Printed in the United States of America.

PERMISSION TO PHOTOCOPY. The appearance of the code at the bottom of the first page of an article in this journal indicates the copyright owner's consent that copies of the article may be made for personal or internal use or for the personal or internal use of specific clients. This consent is given on the condition, however, that the copier pay the stated per copy fee of 3.00 USD through the Copyright Clearance Center, Inc., 222 Rosewood Drive, Danvers, Massachusetts 01923, for copying beyond that permitted by Sections 107 or 108 of the U.S. Copyright Law. This consent does not extend to other kinds of copying, such as copying for general distribution, for advertising or promotional purposes, for creating new collective works, or for resale.

The book cover features a dark blue background with a repeating pattern of binary code (0s and 1s) in a lighter blue color. Overlaid on this are several light green, 3D wireframe cubes arranged in a grid-like pattern, some appearing to float or be connected by faint lines. A diagonal grey line runs from the bottom left towards the top right. The title is written in large, bold, white sans-serif font, centered on the cover.

Blockchain Applications in Geographical Information Systems

By Arif Furkan Mendi and Alper Çabuk



INTRODUCTION

Blockchain technology is one of today's most popular technologies. Blockchain, which we can define as a decentralized distributed database system, technically combines all records in the block structure and unites them as an integral chain that stores them from the first block. The main advantage of Blockchain technology is that the information obtained is precise and cannot be changed.

Blockchain technology enables clients and providers to operate directly with each other without the need for authentication by a third party. All transactions are held in a distributed database using cryptography to ensure that the transaction between the client and the provider can be done safely. To make changes to this distribution structure, the corresponding change must be saved on all computers in the system. In order for a cyberattack to be successful, the corrupted data must be verified by at least 50% of the users within the whole network, which makes the success of an attack almost impossible. Advantages such as more security, agentless processing, and transparency in data tracking make Blockchain technology attractive for geographical information systems.

Today we see the popularity of Blockchain technology in financial transactions such as Bitcoin. However, Blockchain is a system that can be programmed to record the value of almost everything, not just financial transactions. Blockchain technology is an emerging technology that meets the need of buyers and sellers to exchange data in a digital environment resistant to cyberattacks without the need of any third-party intermediaries.

Since 2015, applications have been developed in many areas using Blockchain technology including geographical information systems. Yli-Huumo argues that Blockchain applications are not limited to cryptocurrency applications and Blockchain will provide diversity and knowledge to work in various areas of smart ownership (Yli-Huumo, Ko, Choi, Park, & Smolander, 2016). This arena is one of the significant areas that can use Blockchain technology. There are valuable applications of GIS-Blockchain usage in land registration (currently used in Brazil, Honduras and Sweden), detection of border violations, and food tracking systems. In this paper, the use of Blockchain infrastructure in geographical information systems will be examined.

Photogrammetric Engineering & Remote Sensing
Vol. 86, No. 1, January 2020, pp. 5–10.
0099-1112/20/5–10

© 2020 American Society for Photogrammetry
and Remote Sensing
doi: 10.14358/PERS.86.1.5

SMART CONTRACTS

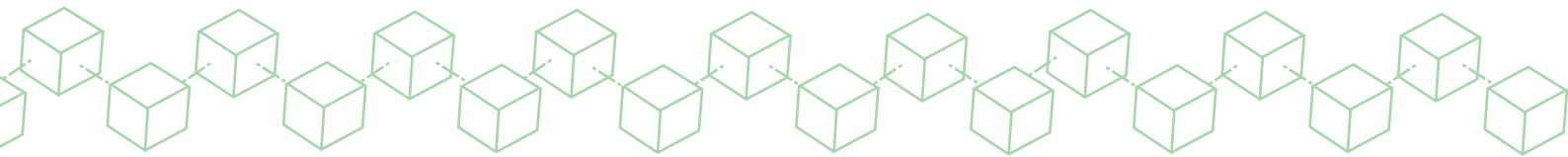
Bitcoin crypto currency has obscured Blockchain technology due to its popularity in the financial field. However, Bitcoin is actually an application developed using Blockchain technology and has gained much more stature than Blockchain technology. Many people who do not know Blockchain technology are quite knowledgeable about Bitcoin. However, Blockchain technology can also be applied to many other areas. For example, in a cloud service using Blockchain technology, an environment can be created for smart contracts and peer-to-peer data sharing (Swan, 2015). Data integrity, which is the strong point of Blockchain technology, is the reason its use has spread to other services and applications.

Blockchain technology enables the participants in the network to execute transactions without third-party validation, even if the parties do not have mutual interests. Therefore, an agreement between a buyer and a seller can be achieved faster by eliminating intermediaries. When the data on the chains are encrypted, there is no need for central authority. Blockchain smart contracts automatically execute files or named scripts that are integrated with each other evenly in a smooth manner (Christidis & Devetsikiotis, 2016). Within the framework of the agreement made with the application of the Blockchain smart contracts, payment terms, conditions and processing steps are determined, then all these steps are implemented without additional third-party verification.

The idea of smart contracts was first proposed by Nick Szabo in 1997 (Nick Szabo, 2018). However, the idea of using Blockchain to track ownership status and transfer of ownership was first described by Mike Hearn in the article "Smart Property" (Mike Hearn, 2018). After Blockchain technology became increasingly widespread, Blockchain smart contracts gained popularity and many applications emerged. Ethereum and Hyperledger are the most popular applications of smart contracts and numerous applications can be developed using these platforms.

Ethereum

When we look at the popular applications that offer smart contract infrastructure, Ethereum is the most notable example. Ethereum is crypto money like Bitcoin and is based on a decentralized structure using Blockchain technology. The main difference between Ethereum and Bitcoin is that Ethereum allows a number of smart contracts (Founder & Gavin, 2017). Ethereum, designed and coded by Vitalik Buterin and his team, was first launched at the Bitcoin Conference on July 30, 2015. Ethereum offers the most widely used smart contract infrastructure. Various studies have been done with this useful application and experts have emphasized that Ethereum can be transformed into a platform for smart contracts (Huh et al., 2017).



Hyperledger

One of the main problems of implementing Blockchain technology is that standardization does not occur. A standard has not been established because many different software groups construct the systems differently. In order to solve this problem, an open source community called Hyperledger was established. Large technology companies like IBM, Cisco, Fujitsu as well as financial institutions such as Morgan and Accenture were involved in this community (“Hyperledger,” 2018). In July 2017, Hyperledger Fabric 1.0 was released. In February 2018, Hyperledger Sawtooth 1.0 was released. The Hyperledger community aims to create a mature version after receiving users’ feedback on these different versions.

REPRESENTATIVE EXAMPLES

The advantages of Blockchain such as enhanced security, speed, transparency, and agentless processing are attractive for application developers. Companies can use their own platforms for the applications they want or use platforms such as Ethereum and Hyperledger. Blockchain applications are preferred in many areas in order to obtain more transparent and highly secured processes at reduced cost by the removal of intermediaries. Geographic information system applications are one of these areas.

Ylii-Huumo points out that it is possible to work on smart property blockchains, and emphasizes that they have identified prototype applications (Yli-Huumo et al., 2016). Land registration information, boundary violation detection, and food tracking applications are examples.

Land Registry

A land registration system is one of the areas where Blockchain can be considered as a potential star candidate. Ylii Huumo emphasizes the impact of increasing Blockchain research on the development of the system and uses a decentralized database to illustrate the idea that companies can sell their properties in a virtual environment, which may represent a revolutionary solution (Yli-Huumo et al., 2016). Carrying out land registration procedures through a Blockchain will help to reduce or eliminate the intermediaries and provide a safe and transparent way of conducting transactions.

In a similar approach, Lamieux argues that Blockchain is

a new technology with the potential to radically change the registration of land and real property transactions. The author emphasized applications using Blockchain technology in Brazil, Georgia, Ghana, India, Japan, and Sweden (Lemieux, 2017). The application is being implemented as a pilot but it is envisaged that the number of full-time transitions will increase.

Spielman argues that the Blockchain land registration system is the future of land registration, and its advantages will be evident over the current land registry system. Land registration through Blockchain can increase processing efficiency, prevent fraud in property exchange, add security levels, accountability and transparency, and lower sensitivity to natural or man-made disasters (Spielman, 2016). The basic workflow of Blockchain based land registry systems is shown on Fig 1.

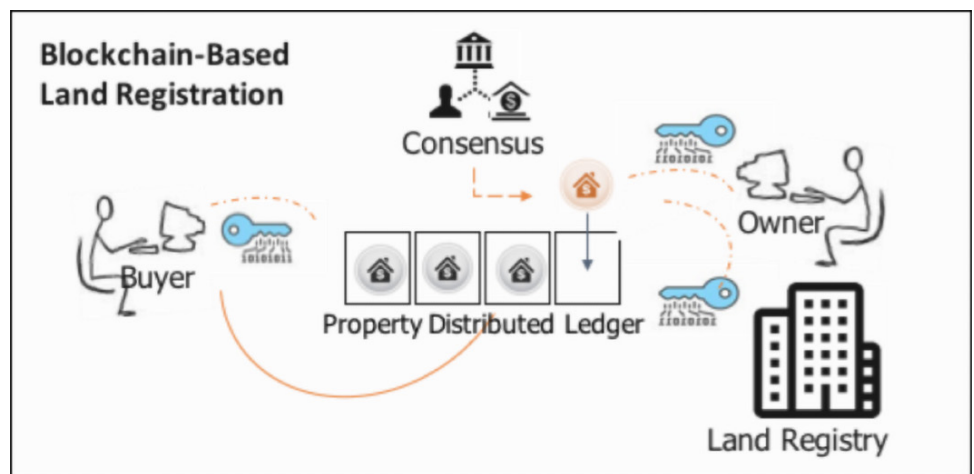
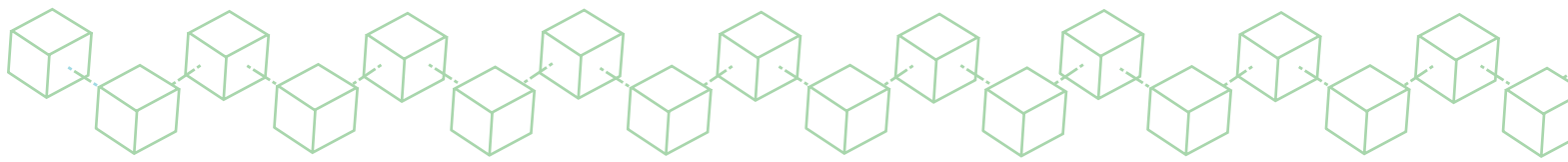


Figure 1. Basic Work Flow of Blockchain Land Registry Systems (eSatya, 2019).

Even with these advantages, some issues need to be clarified before a land registration system is built using Blockchain. Documents provided through the system should contain legal evidence in the case of dispute, ensuring that the system is accurate. . At this point, issues such as how to transfer old records into the system and how to manage legislation through the system should also be clarified. Otherwise, the applicability of the system will be low (Lemieux, 2017).

When we look at examples of land registry, we see that applications in Brazil, Honduras, and Sweden come to the forefront. Factom, a US-based Blockchain technology company, has developed a Blockchain based land registration solution for Honduras. Honduras’ application was the first one using Blockchain technology for land registration. Much of the data collected between November 2015 and January 2016 was found in whitepapers. Honduras wanted to switch to a Blockchain-based system was due to the irregularities in the land registration process. The Honduran government aimed at reforming the system by enacting a number of laws to prevent



irregularities during land registration, but these new regulations were also vulnerable to manipulation, including de facto counterfeiting. For this reason, they have agreed with Factom to implement a Blockchain-based system (Lemieux, 2017).

Another Blockchain land registration project was implemented in the Rio Grande do Sul Province of Brazil, Pelotas Municipalities, and Morro Redondo between May and July 2017 by Ubitquity. The aim of the project was to create a pilot program for official land registration in the region, to reduce costs, and to increase the accuracy, security and transparency of land records. Before this system was implemented, the transfer of ownership was carried out in 13 steps. In explaining the pilot, Ubitquity CEO Nathan Wosnack said they would carry out the Blockchain solution in a fair and transparent manner to address property and land disputes, with the intention that the system will prevent fraud in land registration. (Lemieux, 2017). After evaluating the data obtained through the Blockchain application, errors in the registration system were reduced and there has been a significant ease in archiving (Allison, 2018).

Sweden is another country that has moved its land registration processes into a Blockchain-based system. In the “World Bank Business Index” data, Sweden is among the most accurate in the world for property registration, so its move toward Blockchain technology was not due to fraud or irregularity in its processes as in Brazil and Honduras. The cadastral opera-

tions are done separately but integrated with each other. The transfer process is completed in seven steps, and a notary lawyer does not participate in the project. The pilot project data was collected between July and October 2017. And the application developed by Chromaway is still in use (Lemieux, 2017). The user interface of the application is seen in Figure 2.

With the success of the practice in Sweden, Ukraine announced in October 2017 that it will transport the country’s land registration system to Blockchain in order to provide transparency in the processes (“Ukrainian Blockchain Land Registry,” 2018). In a similar fashion Andre Pradesh, a state in India, announced in October 2017 that the land registration system of Chromaway will also be used for a pilot (“Indian Blockchain Land Registry,” 2018).

Considering that the technology is relatively new and the application includes many different stakeholders, the specific uses require time to reach maturity. Even with the advantages of the application, clarifying any risks such as the fact that the data may be used as legal evidence after a lengthy period, is of great importance to ensure the continuity of the system. . These issues are mostly subject to regional regulations and their implementation architecture, and a single solution in the international market is not realistic. The local laws of all countries differ; and, as a result, there is a need to make local specialization. When the projects completed so far are examined, we expect to say that the application offered

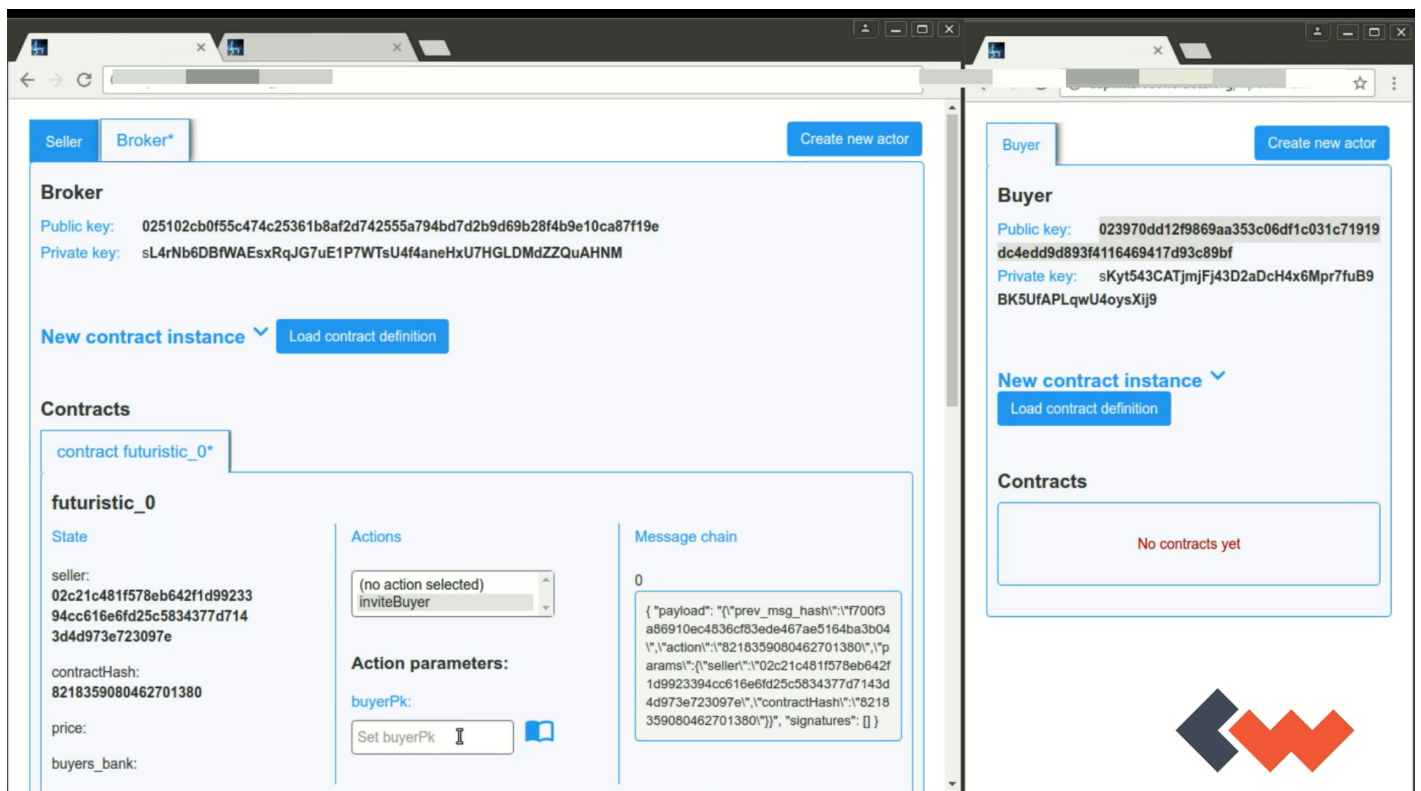
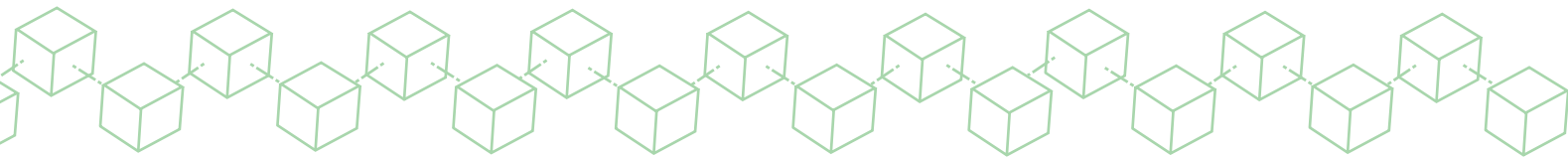


Figure 2. A Screenshot of Chromaway Land Registry Application (“ChromaWay Land Registry,” 2018).



by Chromaway has gained the most popularity with its user interfaces and system design. With this success, the number of regions that are using the application has grown and the number of uses may increase with greater speed as the advantages of Blockchain land registration systems are publicized.

Border Violation Detection

Another Blockchain GIS application is for boundary detection violations. This cadastral Blockchain work, which was developed in Turkey/Kirsehir, was presented by Abdulvahit Torun. The problem of inconsistent demarcation between successful cadastral surveys emerged in that country and a method based on a hierarchical Blockchain model has been proposed to prevent such situations. After presenting two separate physical boundary overlap studies represented as accurate, an effective Computer-aided design (CAD) GIS method based on Blockchain technology was proposed to prevent such incidents in Kirsehir. In the proposed method, there is no border change operation in the land registry unless the joint approval of all stakeholders is received (Torun, 2018). Torun stated in his study that the main purpose of using the Blockchain in the cadastre is to manage the process of determining any boundaries that cause conflicts. The author proposed that with Blockchain technology, land registration procedures will be decentralized, transparent, and open to everyone. In addition, with the common participation of all stakeholders and supervision of the official authorities, property transactions could be managed safely (Torun, 2018). The purpose of digitization of the processes is similar to Blockchain land registration applications in Brazil, Honduras, and Sweden. In addition, considering that the purpose for the transition of Honduras and Brazil to Blockchain includes the elimination of the irregularities in the existing systems throughout the countries, the objective of more efficient land registration is achieved.

Food Tracking Systems

In October 2018, IBM announced the commercial availability of a Blockchain-based electronic distributed ledger that can track and trace food supply chain data from farm to store (IBM, 2018). IBM's Food Trust ledger, which was created using Hyperledger Fabric infrastructure, will allow food retailers, suppliers and growers to see supply chain data in near real time, enabling a more transparent and efficient method of determining the origin and safety of products.

In September 2018, retail giant Walmart announced that it would begin requiring its suppliers to implement the system to track bags of spinach and heads of lettuce. Walmart says it now has a better system for pinpointing which batches

of leafy green vegetables may be contaminated. After a two-year pilot project, the retailer announced that it would be using a Blockchain to keep track of the produce (Corkery & Popper, 2018).

In similar manner, Carrefour, one of the leaders in food traceability, through the gradual application of Blockchain technology to its quality line products, has joined other participants involved in building the IBM Food Trust platform. The companies stated that the objective of this collaboration is to implement a global food traceability standard from producers through to market (Carrefour Group, 2018).

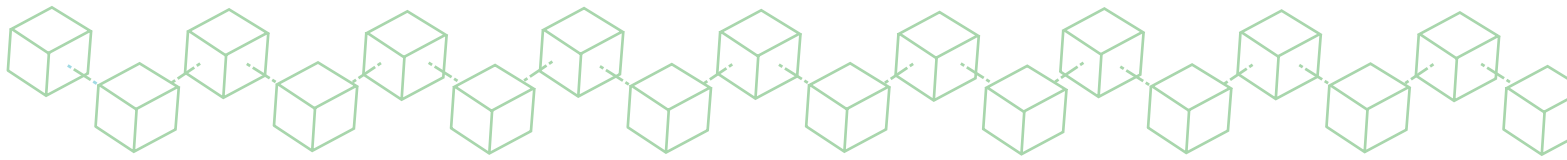
CONCLUSION

Advantages such as enhanced security, agentless processing and transparency in data tracking make Blockchain technology attractive. The GIS-Blockchain applications will mature through increased usage, and updating the applications once any feedback is received from long-term use. After the elimination of risks arising mostly from the diversity of local laws, the advantages of GIS-Blockchain applications will begin to emerge and the number of uses will increase. With the expectation that land registration applications will stand out among Blockchain-based applications, then the boundary violation detection systems can be implemented easily.

In addition, the advantages of traceability and increased security may appeal to big companies and lead them to invest in developing food-tracking applications through Blockchain. As successful results increase, there will be more diversity in the number of GIS applications of Blockchain technology.

References

- Allison, I. (2018). Blockchain-based Ubitquity pilots with Brazil's land records bureau. <https://www.ibtimes.co.uk/blockchain-based-ubitquity-pilots-brazils-land-records-bureau-1615518>. (last date accessed 1 April 2018)
- Carrefour Group. (2018). Food traceability: Carrefour, a blockchain pioneer in Europe, has joined the IBM Food Trust platform to take action on a global scale. <http://www.carrefour.com/current-news/food-traceability-carrefour-a-blockchain-pioneer-in-europe-has-joined-the-ibm-food>. (last date accessed 22 November 2019).
- Christidis, K., & Devetsikiotis, M. (2016). Blockchains and Smart Contracts for the Internet of Things. *IEEE Access*, 4, 2292–2303. <https://doi.org/10.1109/ACCESS.2016.2566339>.
- ChromaWay Land Registry. (2018). <https://chromaway.com/landregistry/>. (last date accessed 26 May 2018).
- Corkery, M., & Popper, N. (2018). From Farm to Blockchain: Walmart Tracks Its Lettuce - The New York Times.. <https://>



www.nytimes.com/2018/09/24/business/walmart-blockchain-lettuce.html. (last date accessed 18 March 2019).

eSatya. (2019). Land Registry Powered by Blockchain (Demo) - Blockchain in Nepal | eSatya. <https://esatya.io/news/land-registry-powered-by-blockchain/>. (last date accessed 15 August 2019).

Founder, G. W., & Gavin, E. (2017). Ethereum: A Secure Decentralised Generalised Transaction Ledger, 1–32.

Hearn, M. (2018). Smart Property - Bitcoin Wiki. https://en.bitcoin.it/wiki/Smart_Property. (last date accessed 31 March 2018).

Huh, S., Cho, S., & Kim, S. (2017). Managing IoT devices using blockchain platform. *International Conference on Advanced Communication Technology*, ICACT, 464–467. <https://doi.org/10.23919/ICACT.2017.7890132>.

Hyperledger. (2018). <https://www.hyperledger.org/>. (last date accessed 19 May 2018).

IBM. (2018). Blockchain in Food Safety: IBM Blockchain Blog. <https://www.ibm.com/blogs/blockchain/category/blockchain-in-food-safety/>. (last date accessed 18 March 2019).

Indian Blockchain Land Registry. (2018). <https://www.coindesk.com/andhra-pradesh-partners-with-chromaway-to-develop-blockchain-land-registry/>. (last date accessed 7 April 2018).

Lemieux, V. L. (2017). Evaluating the Use of Blockchain in Land Transactions: An Archival Science Perspective. *European Property Law Journal*, 6(3), 392–440. <https://doi.org/10.1515/eplj-2017-0019>.

Spielman, A. (2016). Blockchain: Digitally Rebuilding the Real Estate Industry. <https://dci.mit.edu/research/avi-spielman-blockchain-real-estate>. (last date accessed 22 November 2019)

Swan, M. (2015). *Blueprint for a new economy*. O'Reilly Media, Inc. <https://doi.org/10.1017/CBO9781107415324.004>

Szabo, Nick. (2018). The Idea of Smart Contracts. <http://www.fon.hum.uva.nl/rob/Courses/InformationInSpeech/CDROM/Literature/LOTwinterschool2006/szabo.best.vwh.net/idea.html>. (last date accessed 31 March 2018).

Torun, A. (2018). Hierarchical Blockchain Architecture for a Relaxed Hegemony on Cadastre Data Management and Update : A Case Study for Turkey. https://www.researchgate.net/publication/321485252_Hierarchical_Blockchain_Architecture_for_a_Relaxed_Hegemony_on_Cadastre_Data_Management_and_Update_A_Case_Study_for_Turkey. (last date accessed 22 November 2019).

Ukrainian Blockchain Land Registry. (2018). <https://www.coindesk.com/ukrainian-government-to-start-blockchain-land-registry-trial-in-october/>. (last date accessed 7 April 2018)

Yli-Huumo, J., Ko, D., Choi, S., Park, S., & Smolander, K. (2016). Where is current research on Blockchain technology? - A systematic review. *PLoS ONE*, 11(10), 1–27. <https://doi.org/10.1371/journal.pone.0163477>.



ASPRS
Rising Star
PROGRAM

Meet Our Rising Stars!

Chris Stayte
Sponsored by Woolpert, Inc.

Corey Ochsman
Sponsored by Woolpert, Inc.

Collin Hutcheson
Sponsored by Merrick & Company

Charles Krugger
Sponsored by Stahl Sheaffer Engineering, LLC

Kristine Taniguchi-Quan, Ph. D.
Sponsored by Pacific Southwest Region of ASPRS

The Rising Star program is focused on mentorship of tomorrow's leaders within ASPRS and the geospatial and remote sensing community. Geospatial companies, agencies, and ASPRS regions can all benefit by participation in the program through the advancement and professional development of their employees or associates through the process of sponsorship.

For more information go to www.asprs.org/rising-star-program.

Authors

Arif Furkan Mendi, System Engineer, Training and Simulation Technologies, HAVELSAN A.Ş., Ankara, Turkey, afmendi@havelsan.com.tr.

Alper Çabuk, Prof. Dr., Faculty of Architecture and Design Eskişehir Technical University, Eskişehir, Turkey, acabuk@eskisehir.edu.tr.

New to Python? Here’s how to get started.

Although some computer programming languages come and go in popularity (think BASIC from the 1980’s and 1990’s), others gain in popularity and spread to accommodate many different niches. The Python language has now gone through three major upgrades and numerous interim revisions. The current version, Python 3.7.4, was released in July 2019 and has been widely accepted across many computational disciplines, including physics and astronomy, mathematics, gaming and graphic modeling, and geographic information systems (GIS), and across many hardware platforms.

However, for some GIS practitioners, getting started with Python may be intimidating. There are thousands of pages of documentation, thousands of web-pages (see <https://www.python.org>), and likely more than 100 different “python editors,” including on-line versions. So, where is a novice to start?

If you are working in the Esri or QGIS GIS environments, the answer is simple. Use ModelBuilder or Graphical Modeler in ArcGIS or QGIS respectively, to construct your workflow, and then export that model to Python. These are the simple steps you can take to build a custom Python script; (1) construct an Esri ModelBuilder (or QGIS Graphical Modeler) workflow, (2) export the model to a Python script, and (3) use any text editor to customize that Python script. The following illustrates the Esri workflow, but the workflow in QGIS is nearly identical.

Suppose you have two TIF rasters, East.tif and West.tif, that you would like to clip to a 1500 meter x 1500 meter grid and merge into a single raster for easier analysis. Knowing this simple set of parameters, you can build a workflow in ModelBuilder by adding two Clip operations—one for East.tif and one for West.tif, with a Clipping_Grid.shp shapefile used by each—and having the result of each operation input into the Mosaic to New Raster tool. The model might look like Figure 1.

Python 3.7.4, was released in July 2019 and has been widely accepted across many computational disciplines, including physics and astronomy, mathematics, gaming and graphic modeling, and geographic information systems (GIS), and across many hardware platforms.

This ModelBuilder model will clip the two rasters and mosaic them together into a single output TIFF file. But suppose you have a long list of rasters for which you want to accomplish the same task. There are ways to do this in ModelBuilder, but they are time-consuming or more complex than the alternative, which is to add just a couple of lines of simple code to the model you have just built.

Start by clicking “Model” in the upper left corner of the ModelBuilder window. From the menu, select “Export,” then “To Python Script...” This action will save the script as a .py file to the directory of your choosing. You can open this

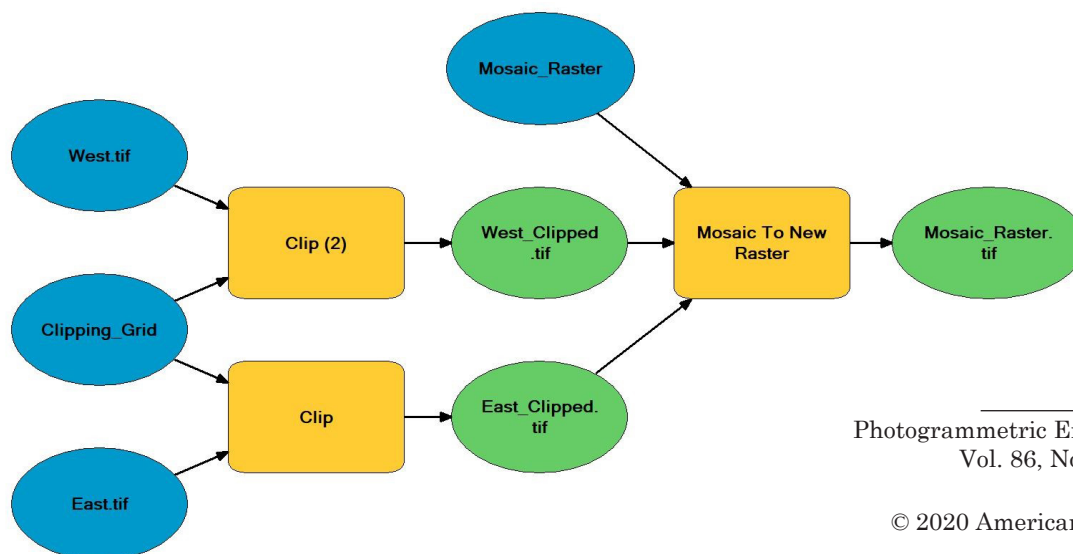


Figure 1.

file with a script editor, such as IDLE or with Microsoft's™ Notepad. The exported script for the model above looks like Figure 2.

When the script is exported from ModelBuilder, it has simple comments (denoted by a “#”) indicating the list of variables (inputs and outputs) and where in the processing workflow, each GIS tool is called (=used). This information is a great guide for seeing how the variables are defined and the order in which Python reads and executes operations. In this example, all the variables are hard-coded to the specific files and file paths used as inputs and outputs by the ModelBuilder model. In other words, the variables are not variable.

To make the model more flexible, you can start by defining a file path (instead of a singular file) where the input rasters are located. Setting this as the workspace (an environment variable) also allows you to perform any analytical, array, or list operations on the files in that folder without setting additional file path variables. You can then define your local variables, which in this case are the clipped rasters and merged raster output folders, clipping grid, and a list of the rasters in the input folder. Remember that it is always a good idea to leave informative comments in your code so that you or others can come back to it and know what each step is doing.

The new list of variables, with comments for reference, is displayed in Figure 3.

From here, you can use the same Clip process as in the original exported Python script. However, instead of setting it up to run on specific files, you can wrap it into a simple “for” loop, which clips each raster in the list of rasters created earlier, Figure 4.

You can now execute the Mosaic to New Raster function using the same techniques already mentioned. To ensure you are manipulating the clipped rasters and not the originals, you can change the workspace environment variable to the folder location where the clipped rasters are stored. Then create a new list of the clipped rasters. Because the Mosaic to New Raster tool is set up to handle multiple files, a “for” loop

```
# Import arcpy module
import arcpy

# Local variables:
East_tif = "East.tif"
Clipping_Grid = "Clipping_Grid"
East_Clipped_tif = "C:\Script_Test\Clipped_Rasters\East_Clipped.tif"
Mosaic_Raster_tif = East_Clipped_tif
West_tif = "West.tif"
West_Clipped_tif = "C:\Script_Test\Clipped_Rasters\West_Clipped.tif"
Mosaic_Raster = "C:\Script_Test\Mosaic_Raster"

# Process: Clip
arcpy.Clip_management(East_tif, "604500 3550500 700500 3745500", East_Clipped_tif, Clipping_Grid, "256", "ClippingGeometry", "NO_MAINTAIN_EXTENT")

# Process: Clip (2)
arcpy.Clip_management(West_tif, "604500 3550500 700500 3745500", West_Clipped_tif, Clipping_Grid, "256", "ClippingGeometry", "NO_MAINTAIN_EXTENT")

# Process: Mosaic To New Raster
arcpy.MosaicToNewRaster_management("C:\Script_Test\Clipped_Rasters\East_Clipped.tif;C:\Script_Test\Clipped_Rasters\West_Clipped.tif",
Mosaic_Raster, "Mosaic_Raster.tif", "", "8_BIT_UNSIGNED", "", "1", "LAST", "FIRST")
```

Figure 2.

```
# Import arcpy module
import arcpy

# Copy and paste the file path to the folder containing the rasters that you wish to clip.
arcpy.env.workspace = r"C:\Script_Test\Original_Rasters"

# Local variables:
# Copy and paste the file path to the folder where you want the clipped rasters to go.
out = r"C:\Script_Test\Clipped_Rasters"

# Copy and paste the file path to the extent shapefile that you want the rasters clipped by.
Clipping_Grid = r"C:\Script_Test\Tile_Grid\Clipping_Grid.shp"

# Copy and paste the file path to the merged raster output.
mosaic_out = r"C:\Script_Test\Mosaic_Raster"

# Make a variable that lists all of the rasters within your current workspace, defined above.
rasters = arcpy.ListDatasets("","Raster")
```

Figure 3.

```
# Process: Clip
# Iterates through and clip each of rasters in the "rasters" list variable. This step also adds "Clipped_" to the beginning
# of each clipped raster file name and prints a message after each raster is successfully clipped.
for r in rasters:
    arcpy.Clip_management(r, "",out+ "\\" + "Clipped_" + str(r), Clipping_Grid, "256", "ClippingGeometry", "NO_MAINTAIN_EXTENT")
    print(r + " successfully clipped.")
```

Figure 4.

```
# Process: Mosaic To New Raster
# Set the workspace to the location of the clipped rasters, which will become the input (as a list)
# for the "Mosaic to New Raster" tool.
arcpy.env.workspace = out

clipped_rasters = arcpy.ListDatasets("","Raster")

arcpy.MosaicToNewRaster_management(clipped_rasters, mosaic_out, "Mosaic_Raster.tif", "", "8_BIT_UNSIGNED", "", "1", "LAST", "FIRST")
```

Figure 5.

is not required for this function. Instead, you can simply set the input as the list variable you just created and run the script, Figure 5.

This is just the beginning of how you can get creative with Python and ModelBuilder and/or Graphical Modeler. You can tweak parameters for an individual tool or process, add error checks or multiple iterations, print statements to show you the progress of the script, define styles, integrate tools from other geospatial software packages, and so much more.

If you would like a copy of the final Python script or any other additional instructions, please contact us at geospatial@dewberry.com.

Chris Griesbach, Andrew Collins, and Al Karlin, Ph.D., CMS-L, GISP are with Dewberry’s geospatial and technology services group in Tampa, Florida, and Denver, Colorado. Chris manages many aspects of lidar production and imagery analysis for Dewberry. Andrew is part of the quality management team, ensuring data integrity and developing streamlined procedures for all stages of elevation data production and delivery. As a senior GIS professional, Al works with all aspects of lidar, remote sensing, photogrammetry, and GIS-related projects.

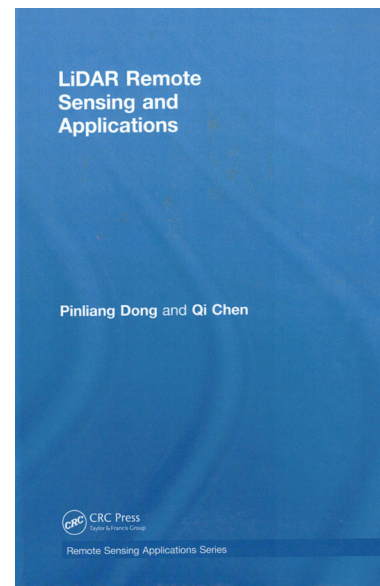
LiDAR Remote Sensing and Applications, by Dr. Pinliang Dong and Dr. Qi Chen, CRC Press, 2018, introduces the fundamentals of lidar remote sensing and is intended as a textbook for the undergraduate and graduate student in the fields of geography, forestry, ecology, geographic information science, remote sensing, and photogrammetric engineering.

The book consists of a total of six chapters, reference section, and index. For most of the book, the hands-on exercise projects and references follow the text in the chapters. It also includes an index map of lidar data used in the exercises and a list of abbreviations.

Commencing with the lidar Data Index Map, chapter 1, a Brief Overview of Remote Sensing, the authors discuss the history of remote sensing, basic concepts and methods or technologies of passive and active remote sensing that are introduced in separate sections. This is a short chapter with only 21 pages, but with easily understood diagrams, colorful pictures and mathematical formulas. The authors provide thoughtful explanations in straight forward language, allowing a reader to master some basic information and concepts of remote sensing.

In chapter 2, Principles of LiDAR Remote Sensing, the authors focus on lidar remote sensing by introducing the “Basic Components of LiDAR,” “Physical Principles of LiDAR,” “LiDAR Accuracy,” “LiDAR Data Formats,” “LiDAR Systems” and “LiDAR Resources.” Though a short chapter, it is probably the most important chapter in the book. The authors provide considerable information about lidar remote sensing technology. Though some more detailed information and deeper theories behind lidar technology could have been added, the chapter is definitely very helpful, especially for busy professionals working on lidar data production on a daily basis, who might lack the time to sift through a heavy, complex text. The lidar data resource and free software listed in lidar resources provides handy information for those who want to learn more about the lidar data, master or improve lidar processing skills with limited resources. At the end of the chapter, three hands-on project exercises are provided. In these exercises, the authors introduce the data used for the project, the methodology in the data processing and the purpose of the project. The step-by-step instructions should help a reader complete the project exercises with ease.

Chapter 3, Basics of LiDAR Data Processing, is another important chapter in the book. The authors introduce the basic workflow of lidar processing. In the Introduction section, two of the basic and then the most important steps of processing lidar data are introduced: classification of laser points and interpolation of discrete points into a continuous surface. The products of the classification and interpolation are also mentioned, for example, DTM (digital terrain model), DSM (digital surface model), DHM (digital height model) and TIN (triangulated irregular network). The flowchart of lidar point data



LiDAR Remote Sensing and Applications

Pingliang Dong and Qi Chen

CRC Press, 2018. ISBN: 978-1-482-24301-7. Pages: 200

Review by Connie Li Krampf, CP, CMS, MSCS, Project Manager - Photogrammetry, Weston & Sampson, Cary, North Carolina

processing on page 42 helps a reader understand the major steps of lidar point data processing. The section on filtering explains the filtering algorithm used in processing, while the subsections TIN-based methods and raster-based methods explain the methods used in the processing, which provides important information for a reader to understand how these methods apply in the real lidar data production world. The section, Classification of Non-Ground Points, provides the reference information in the processing. In the section, Spatial Interpolation, the authors make extra effort to explain how the spatial interpolation works through detailed pictures, diagrams, and mathematical formulas. Following the section, two hands-on project exercises -- Creating DTM, DSM, and DHM from LiDAR Data, and -- Creating A Terrain Dataset using LiDAR Data, are provided. Readers should find the exercises interesting and helpful for understanding the discussions in the chapter.

Chapter 4 presents LiDAR for Forest Applications. The

Photogrammetric Engineering & Remote Sensing
Vol. 86, No. 1, January 2020, pp. 13–14.

0099-1112/20/13–14

© 2020 American Society for Photogrammetry
and Remote Sensing

doi: 10.14358/PERS.86.1.13

authors show how lidar has become a revolutionary remote sensing technology compared with the conventional optical and radar remote sensing technologies. The chapter introduces several topics in lidar applications in forest studies. Figure 4.1 lists the categories of lidar for forest applications based on sensor type, footprint size, and information extraction method, which provides very useful information in a simple manner. In the section on Canopy Surface Height Modeling and Mapping, the authors focus on one particular type of vegetation height product: a raster grid that stores the upper surface height of vegetation canopy, i.e. canopy height model (CHM). The section outlines the CHM generation processes, the challenges in processing and approaches and methods to address those challenges and problems by giving examples with detailed explanations. Readers of the book will find the flowcharts, diagrams and formulas in the section helpful for their understanding of the discussions in this section. LiDAR Metrics for Vegetation Analysis discusses lidar-based metrics for predicting the forest attributes in the vegetation analysis with a specific example of 22 metrics for vegetation modeling. Individual Tree Isolation and Mapping covers a lot of details about Grid-Based Tree Mapping and Point-Based Tree Mapping. This section also discusses Remaining Challenges in Tree Mapping and introduces A Simulation Study For Tree Isolation that I found very interesting. Area-Based Modeling and Mapping explains how after-based approaches are used in a larger project area. In the Modeling, Mapping and Estimating Biomass section, the authors point out that "...forest biomass is a key climate variable for the global carbon cycle and has attracted the attention of both scientists and policymakers" and "...is also an attribute that is very difficult to estimate". Because of this, the authors describe lidar that "has emerged as the most promising technology for biomass estimation". In this section, the authors discuss the existing studies on area-based approaches using lidar with great technical details. Both the student and the industry practitioner will appreciate the useful information provided in this section. Following the chapter, two hands-on projects, Extraction Canopy Heights from Leaf on and Leaf Off LiDAR Data and Identifying Disturbances from Hurricanes and Lightning Strikes to Mangrove Forests using LiDAR Data in Everglades National Park are very helpful. Questions in the projects are designed to help readers think through the exercise.

Chapter 5, LiDAR for Urban Applications, discusses the lidar applications used in Road Extraction, Building Extraction and 3D Reconstruction, Population Estimation, Change Detection, Assessment of Post Disaster Building Damage, and Assessment of Post Disaster Road Blockage. In each section, the authors describe the lidar technology in each application with detailed background information, techniques used in the processing, and mathematical theories of the technology. Most of the sections include a flowchart of the application and expla-

nations of major steps with pictures and diagrams, which help readers follow the line of thought the authors convey in the chapter. Following the chapter, project exercises, Locating 3D LiDAR Points Near a Powerline in the City of Denton, TX, USA and Small Area Population Estimation using Count, Area and Volume of Residential Building Extraction from LiDAR Data in Denton, TX, provide additional opportunities to get hands-on exercises to better understand the chapter content.

The final chapter, LiDAR for Geoscience Applications, I found to be the most interesting section of the book. The chapter focuses on lidar applications in the study of six major features/phenomena in geosciences: Aeolian Landforms, Fluvial Landforms, Surface Hydrology, Volcanic and Impact Landforms, Tectonic Landforms, and Lithology and Geologic Structures. Similar to the previous chapters, the authors use pictures, diagrams, flowcharts and detailed explanations to discuss the lidar technologies used in a variety of landform studies. Following the chapter, two hands-on project exercises Measuring Sand Dune Migration using Multi-temporal LiDAR Data in White Sands Dune Fields, NM, and Deriving Trend Surfaces of Simple Fold using LiDAR Data in Raplee Ridge, UT, USA, are quite helpful for understanding the chapter better and also demonstrate a very interesting use of the technologies.

LiDAR Remote Sensing and Applications is well written and well organized. The data for hands-on exercises are properly selected, step-by-step instructions, content, and questions in the project exercises are very helpful and thoughtfully constructed for readers to learn through hands-on learning. The book can function as a reference book as well as a textbook, not only for readers, but also for the geospatial professional who produce or use lidar data on a daily base. The authors present their own work and findings while introducing other expert and scholarly studies and research in the lidar application. The user will benefit from studying the contents, checking out the references provided, and working with the hands-on project exercises.

Just like anything else, the book is not perfect. Some suggestions might include a better-coordinated coloring/contrast of some of the illustrations to better present the information. Fonts in the book could be a little bit larger. The questions in the project exercises are only found in chapters 4 through 6, where it might be better to provide questions for every project to maintain consistency for the learning process. The picture (black & white) in Figure 4.34 on page 100 should be presented in blue and green, based on the illustration's description. Nevertheless, the book is highly recommended for its rich information and well-presented contents.

JOURNAL STAFF

Editor-In-Chief

Alper Yilmaz, Ph.D., PERSeditor@asprs.org

Associate Editors

Rongjun Qin, Ph.D., qin.324@osu.edu

Michael Yang, Ph.D., michael.yang@utwente.nl

Petra Helmholtz, Ph.D., Petra.Helmholtz@curtin.edu.au

Bo Wu, Ph.D., bo.wu@polyu.edu.hk

Clement Mallet, Ph.D., clemallet@gmail.com

Vasit Sagan, Ph.D., Vasit.Sagan@slu.edu

Jose M. Pena, Ph.D., jmpena@ica.csic.es

Prasad Thenkabil, Ph.D., pthenkabil@usgs.gov

Ruisheng Wang, Ph.D., ruiswang@ucalgary.ca

Desheng Liu, Ph.D., liu.738@osu.edu

Valérie Gouet-Brunet, Ph.D., valerie.gouet@ign.fr

Yury Vizilter, Ph.D., viz@gosniias.ru

Dorota Iwaszczuk, Ph.D., dorota.iwaszczuk@tum.de

Qunming Wang, Ph.D., wqm11111@126.com

Filiz Sunar, Ph.D., fsunar@itu.edu.tr

Norbert Pfeifer, Ph.D., np@ipf.tuwien.ac.at

Jan Dirk Wegner, Ph.D., jan.wegner@geod.baug.ethz.ch

Hongyan Zhang, Ph.D., zhanghongyan@whu.edu.cn

Zhenfeng Shao, Ph.D., shaozhenfeng@whu.edu.cn

Dongdong Wang, Ph.D., dddwang@umd.edu

Assistant Editor

Jie Shan, Ph.D., jshan@ecn.purdue.edu

Contributing Editors

Grids & Datums Column

Clifford J. Mugnier, C.P., C.M.S., cjmce@lsu.edu

Book Reviews

Sagar Deshpande, Ph.D., bookreview@asprs.org

Mapping Matters Column

Qassim Abdullah, Ph.D., Mapping_Matters@asprs.org

Sector Insight

Lucia Lovison-Golob, Ph.D., lucia.lovison@sat-drones.com

Bob Ryerson, Ph.D., FASPRS, bryerson@kimgeomatics.com

Project Management Column

Raquel Charrois, PMP, CP, CMS, PMP@asprs.org

ASPRS Staff

Assistant Director — Publications

Rae Kelley, rkelly@asprs.org

Electronic Publications Manager/Graphic Artist

Matthew Austin, maustin@asprs.org

Advertising Sales Representative

Bill Spilman, bill@innovativemediasolutions.com

Candidates for ASPRS Vice-President Announced

The ASPRS Governance Committee Chair, Immediate Past President Anne Hillyer, has announced the candidates for Vice-President for the 2020-2021 term:

- Soe Myint, Professor, School of Geographical Sciences and Urban Planning, Arizona State University and
- Christopher Parrish, Associate Professor, School of Civil and Construction Engineering, Oregon State University

For more information, contact office@asprs.org.

NEW ASPRS MEMBERS

ASPRS would like to welcome the following new members!

Alaska

Curtis Bernard
Jacobie Lynn Gable

At Large

Surya Adhikari
Zolana Rui João
Suraj Bahadur KC
Prof. Xiran Zhou
Ben Paynter

Central New York

Sarina Adeli
Chad Chambers
Haifa Tamiminia
Atef Alla Eddine Amriche
Shahriar Shah Heydari
Jin Xu
Dameng Yin

Eastern Great Lakes

Patricia Ann Horkan
Dr. Shawana Patrice Johnson, GISP
Tongxi Hu

Florida

Ronaldo Blanco
Ali Gonzalez Perez, PLS
Emily Labbate

Heartland

Rachel Jones
Neha Patel

Mid South

Rebecca Mary Hahn
CE Dallas Hoffman
Brian Kloer
Yvonne Swindel Leslie
George S. Mercier
Grayson Morgan
Andong Ma

North Atlantic

Mohammad Abdul Qadir Khan
Johannes Renke Krause
John Majoris

Pacific Southwest

Dr. Indumathi Jeyachandran

Potomac

Megan Coffey
Xiaojie Gao
Elizabeth Hanwell
Ian McGregor

Rocky Mountain

Chris Schaefer
Abigail Gettinger
Anneliese Lilje

Western Great Lakes

Amir Masoud Forati
Bo Peng

FOR MORE INFORMATION ON ASPRS MEMBERSHIP, VISIT

[HTTP://WWW.ASPRS.ORG/JOIN-NOW](http://www.asprs.org/join-now)

Your Path To Success In The Geospatial Community

Digital Elevation Model Technologies and Applications: The DEM Users Manual, 3rd Edition

Edited by David F. Maune, PhD, CP
and Amar Nayegandhi, CP, CMS

To order, visit
<https://www.asprs.org/dem>

The 3rd edition of the DEM Users Manual includes 15 chapters and three appendices. References in the eBook version are hyperlinked. Chapter and appendix titles include:

1. Introduction to DEMs
*David F. Maune, Hans Karl Heidemann,
Stephen M. Kopp, and Clayton A. Crawford*
 2. Vertical Datums
Dru Smith
 3. Standards, Guidelines & Specifications
David F. Maune
 4. The National Elevation Dataset (NED)
*Dean B. Gesch, Gayla A. Evans,
Michael J. Oimoen, and Samantha T. Arundel*
 5. The 3D Elevation Program (3DEP)
*Jason M. Stoker, Vicki Lukas, Allyson L. Jason,
Diane F. Eldridge, and Larry J. Sugarbaker*
 6. Photogrammetry
J. Chris McGlone and Scott Arko
 7. IfSAR
Scott Hensley and Lorraine Tighe
 8. Airborne Topographic Lidar
Amar Nayegandhi and Joshua Nimetz
 9. Lidar Data Processing
Joshua M. Novac
 10. Airborne Lidar Bathymetry
Jennifer Wozencraft and Amar Nayegandhi
 11. Sonar
Guy T. Noll and Douglas Lockhart
 12. Enabling Technologies
*Bruno M. Scherzinger, Joseph J. Hutton,
and Mohamed M.R. Mostafa*
 13. DEM User Applications
David F. Maune
 14. DEM User Requirements & Benefits
David F. Maune
 15. Quality Assessment of Elevation Data
Jennifer Novac
- Appendix A. Acronyms
Appendix B. Definitions
Appendix C. Sample Datasets

This book is your guide to 3D elevation technologies, products and applications. It will guide you through the inception and implementation of the U.S. Geological Survey's (USGS) 3D Elevation Program (3DEP) to provide not just bare earth DEMs, but a full suite of 3D elevation products using Quality Levels (QLs) that are standardized and consistent across the U.S. and territories. The 3DEP is based on the National Enhanced Elevation Assessment (NEEA) which evaluated 602 different mission-critical requirements for and benefits from enhanced elevation data of various QLs for 34 Federal agencies, all 50 states (with local and Tribal input), and 13 non-governmental organizations.

The NEEA documented the highest Return on Investment from QL2 lidar for the conterminous states, Hawaii and U.S. territories, and QL5 IfSAR for Alaska.

Chapters 3, 5, 8, 9, 13, 14, and 15 are "must-read" chapters for users and providers of topographic lidar data. Chapter 8 addresses linear mode, single photon and Geiger mode lidar technologies, and Chapter 10 addresses the latest in topobathymetric lidar. The remaining chapters are either relevant to all DEM technologies or address alternative technologies including photogrammetry, IfSAR, and sonar.

As demonstrated by the figures selected for the front cover of this manual, readers will recognize the editors' vision for the future – a 3D Nation that seamlessly merges topographic and bathymetric data from the tops of the mountains, beneath rivers and lakes, to the depths of the sea.

Co-Editors

David F. Maune, PhD, CP and
Amar Nayegandhi, CP, CMS

PRICING

Student (must submit copy of Student ID)	\$50 +S&H
ASPRS Member	\$80 +S&H
Non-member	\$100 +S&H
E-Book (only available in the Amazon Kindle store)	\$85

Application of PCA Analysis and QR Decomposition to Address RFM's Ill-Posedness

Amin Alizadeh Naeini, Sayyed Hamed Alizadeh Moghaddam, Mohammad Moein Sheikholeslami, and AliReza Amiri-Simkooei

Abstract

Rational function model (RFM) is the most widely used sensor model in the remote sensing community. However, it suffers from ill-posedness, challenging its feasibility. This problem, i.e., ill-posedness, is mainly caused due to highly correlated coefficients of the RFM, which magnifies any small perturbations of observations, such as noise and instrumental error. This paper outlines a novel two-step method, called principal component analysis (PCA)-RFM, based on the integration of PCA and QR decomposition. In the first step, the PCA-RFM reduces the observational perturbations from the design matrix using the PCA. In the next step, the RFM's coefficients are estimated using a QR decomposition with column pivoting and least square method. According to the results, the PCA-RFM is less sensitive than its rivals to the changes of the ground control point (GCPs) distribution. Geometrically speaking, in addition, PCA-RFM is more accurate than recently established methods even in the presence of the small number of GCPs.

Introduction

Rational function model (RFM) is the most famous mathematical model that precisely defines the mathematical relation between the two-dimensional image and three-dimensional world coordinate systems. This model is convenient due to its simplicity, generality, and ease of implementation (Cao *et al.* 2017). However, the RFM generally faces ill-posedness and overparameterization problems mainly due to the existence of unnecessary and highly correlated RFM's parameters, known as rational polynomial coefficients (RPCs) (Moghaddam *et al.* 2018b).

Addressing the overparameterization and ill-posedness problems of the RFM has gained lots of attention in the literature. The existing methods in this context can be broadly categorized as regularization-based techniques and variable selection methods. ℓ_2 -norm regularization technique, called Tikhonov or Ridge estimation (RE) method, is one of the first methods applied by Tao and Hu (2001) to overcome the problem of ill-posedness in the RFM. ℓ_1 -norm regularization technique is another regularization-based technique, which was presented by Long, Jiao, and He (2015) in the context of the RFM. This technique, which is based on convex optimization algorithms, results in a vector of RPCs with some nonzero elements.

In addition to the abovementioned regularization-based techniques, some variable selection methods have been introduced in the literature. Although all these methods pursue an identical objective to select an optimal subset of RPCs, they

apply different methodologies. In this regard, we can mention the methods based on nested regression (Tengfei, Weili, and Guojin 2014), stepwise-then-orthogonal regression (Li *et al.* 2017), statistical solutions (Moghaddam *et al.* 2017; Moghaddam *et al.* 2018b), and metaheuristic optimization algorithms (Gholinejad, Naeini, and Amiri-Simkooei 2018; Li *et al.* 2018; Moghaddam, Mokhtarzade, and Moghaddam 2018a; Naeini *et al.* 2017).

In addition to the aforementioned methods, some methods have been proposed that do not belong to the variable selection and regularization-based categories. In this regard, Zhou, Jiao, and Long (2012) replaced the least-squares (LS) estimation method with a Levenberg-Marquardt algorithm. Recently, Cao and Fu (2018) put forward a method based on a truncated singular value decomposition and the LS method. In that method, the design matrix is firstly decomposed into one diagonal matrix and two orthogonal matrices. Then the LS method is applied to estimate the unknown RPCs.

The problem of ill-posedness is quite severe when experimental data is inexact (e.g., noisy), which is always the case in practice because observational errors are inherent in the data. In the case of ill-conditioning, any small perturbation of data results in a significant error in the solution. In other words, the ill-posedness problem can magnify minor errors in the observations (Aytas, Afacan, and Tuna 2017).

Keeping this in mind, we propose a novel two-step method, based on the integration of principal component analysis (PCA) and QR decomposition. The proposed method mitigates mainly the ill-conditioning problem of the RFM by reducing the effects of data perturbation on the design matrix. To this end, in the first step, PCA initially transforms the design matrix to the principal component (PC) space. Secondly, in the PC space, the unnecessary components that have a considerably small variance are excluded. This makes the design matrix noise-reduced because the excluded components contain almost noise and have no essential information. Then, the noise-reduced design matrix is transformed back to its original space utilizing an inverse PCA transformation. Finally, this design matrix is used to estimate the unknown RPCs.

Because the exclusion of the unnecessary components causes the noise-reduced design matrix to be rank deficient, a novel estimation method is applied in the second step of the method. This estimation method, which is based on a LS method and the QR decomposition with column pivoting, handles not only the rank deficiency but also the problem of overparameterization.

Because the effects of the noise are reduced in the design matrix, the estimated RPCs are less affected by the ill-conditioning problem. From now on, we call the proposed method PCA-RFM.

Amin Alizadeh Naeini is with the Dept. of Earth and Space Science and Engineering, York University, 4700 Keele St, Toronto, ON M3J1P3, Canada (naeini@yorku.ca)

Mohammad Moein Sheikholeslami and AliReza Amiri-Simkooei are with the Department of Geomatics Engineering, Faculty of Civil Engineering and Transportation, University of Isfahan, Isfahan 8174673441, Iran.

Sayyed Hamed Alizadeh Moghaddam is with the Faculty of Geodesy and Geomatics Engineering, Khajeh Nasir Toosi University of Technology, Tehran 1996715433, Iran.

Photogrammetric Engineering & Remote Sensing
Vol. 86, No. 1, January 2020, pp. 17–21.
0099-1112/20/17–21

© 2020 American Society for Photogrammetry
and Remote Sensing
doi: 10.14358/PERS.86.1.17

Methodology

The RFM is expressed as follows (Ma 2013; Tao and Hu 2001):

$$l = \frac{P_1(E, N, h)}{P_2(E, N, h)}, \quad s = \frac{P_3(E, N, h)}{P_4(E, N, h)} \quad (1)$$

where P_i is a third-order polynomial, (l, s) are the image coordinates of a point and (E, N, h) are its coordinates in the object space. Note that the zero-order term in P_2 and P_4 are considered to be "1", and the coordinates of the points are commonly normalized in the range of $[-1, 1]$ in both image and object spaces. Equation 1 is commonly reformulated as follows (Long, Jiao, and He 2015):

$$P_1(E, N, h) - lP_2(E, N, h) = 0 \quad (2)$$

$$P_3(E, N, h) - sP_4(E, N, h) = 0 \quad (3)$$

The unknown RPCs (\mathbf{x}), can be estimated using the ordinary least-squares (OLS) regression as $\mathbf{x} = (A^T A)^{-1} A^T \mathbf{y}$, where A is the design matrix and \mathbf{y} is the vector of observations. However, the OLS solution is affected by the problems of ill-posedness and overparameterization.

Addressing the previously mentioned problems, we put forward the PCA-RFM method. The PCA-RFM generally consists of two steps. In the first step, which itself consists of two phases, the design matrix (A) is initially transformed into a new space, namely, PCs. Then, in the final phase, some inessential PCs of A , containing almost noise, are excluded, and a new noise-reduced design matrix is reconstructed. In the last step, this reconstructed design matrix is used to solve the unknown RPCs. To do this, we apply the QR decomposition with column pivoting and the LS method (Golub and Van Loan 2012) because the reconstructed design matrix is rank deficient. The steps of the proposed method are delineated below.

Step 1: Construct the design matrix $A_{m \times n}$, applying GCPs. $m = 2k$ is the total number of observation equations, where k is the number of applied GCPs, and $n = 78$ is the total number of unknown RPCs. See Long, Jiao, and He (2015), and Moghaddam *et al.* (2018b) for more information of how the design matrix is calculated.

Step 2: Transform the matrix A to the PC space as follows:

Step 2-1: Compute the mean-centered \bar{A} to facilitate the further calculation (see Equation 7).

$$\bar{A} = A_i - \text{mean}(A_i) \quad (7)$$

where A_i is the i th column of the design matrix A , i.e., $A = [A_i]$.

Step 2-2: Calculate the covariance matrix (C) of the new design matrix \bar{A} by applying Equation 8:

$$C = \frac{\bar{A}^T \bar{A}}{m-1} \quad (8)$$

Step 2-3: Conduct an eigen value decomposition on C :

$$C = V \Omega V^T \quad (9)$$

$$V = [\mathbf{v}_1, \mathbf{v}_2, \dots, \mathbf{v}_n]_{n \times n} \quad (10)$$

$$\Omega = \text{diag}([\lambda_1, \lambda_2, \dots, \lambda_n]) \quad (11)$$

where V is a matrix in which the columns are eigen vectors (\mathbf{v}_i) of C , and Ω is a diagonal matrix that contains the corresponding eigen values (λ_i), i.e., $\Omega_{ii} = \lambda_i$. Note that $\lambda_1 \geq \lambda_2 \geq \dots \geq \lambda_n \geq 0$.

Step 2-4: Transform the mean-centered \bar{A} to the PC space to get S as follows:

$$S = \bar{A} V \quad (12)$$

Step 3: Partition the matrices S and V in Equation 12 as follows:

$$S = [S_1 : S_2] = \bar{A} [V_1 : V_2] = [\bar{A} V_1 : \bar{A} V_2] \quad (13)$$

where the $78 \times r$ matrix V_1 contains r eigen vectors that their corresponding eigen values are larger than a threshold t . Moreover, the matrix V_2 contains the remaining eigen vectors having eigen values smaller than the threshold.

The columns of S_2 are the PCs with considerable small variances (i.e., eigen value). These PCs contain almost unnecessary information (such as noise) and can exert a remarkable influence on the derived products in the presence of the ill-posedness problem. Therefore, PCA-RFM weeds out the S_2 and only considers $S_1 = \bar{A} V_1$. In this paper, we empirically set $t = 0.01$.

Step 4: Back-transform S_1 to its original space using an inverse PCA transformation, and reconstruct the noise-reduced design matrix \bar{A}_{nr} as follows:

$$\bar{A}_{nr} = S_1 V_1^T = \bar{A} V_1 V_1^T \quad (14)$$

The LS estimation step demands the real noise-reduced design matrix. To get that, the columns of \bar{A}_{nr} are required to be decentered because \bar{A}_{nr} is a mean-centered matrix (see Step 2-1). This is conducted by adding the corresponding mean values, which are calculated in Step 2-1.

$$A_{nr_i} = \bar{A}_{nr_i} + \text{mean}(A_i) \quad (15)$$

The matrix A_{nr} has a rank of r . This indicates that some of the columns of the new design matrix A_{nr} are strictly dependent, resulting in a rank deficiency. Therefore, we have faced with a rank deficient LS problem if we use A_{nr} as the design matrix.

Step 5: Estimate the unknown RPCs utilizing the "basic solution" of the QR decomposition with column pivoting and the LS method, described in (Golub and Van Loan 2012). Finally, the PCA-RFM results in a vector of RPCs with some nonzero components, which are expected to be less affected by the problems of ill-posedness and overparameterization.

Experiments

Data Sets

In these experiments, nine real data sets (HJ, L5, PL, GE, WV, S1A, S1B, IK, and IRS) from eight different platforms (Table 1) were used to evaluate the performance of the proposed method.

According to Table 1, images with various ground sampling distances (GSDs), ranging from 0.5 m for PL, GE, and WV to 30 m for L5 and HJ were used in the experiments. Regarding the geometric level of correction, all the images except for S1A experienced a primary level of correction, including the correction of distortions introduced by Earth rotation and curvature, resampling of the images to a uniform GSD, and assigning the images to a map projection system. The S1A data set is a geometrically raw image with only a radiometric correction phase.

The control points (CPs) of five data sets, i.e., PL, GE, WV, IK, and IRS, the accuracy of which is better than one meter, were chosen from distinct features of 1:2000 digital reference maps. For the two Spot data sets, a differential global positioning system (DGPS) technique was applied, and finally, for HJ and L5, an automatically matching technique was employed to

extract the CPs from a geo-referenced Landsat-5 image (Long, Jiao, and He 2015).

Competing Methods

Since the proposed method has some prominent qualities, and due to its remarkable performance, we chose methods which can compete with the proposed method in different aspects, including 1) the capability in dealing with the ill-posedness and overparametrization problems, and 2) the applicability in the presence of a small number of GCPs (e.g., ten GCPs). Accordingly, the competing methods, ranging from classical to the cutting-edge, were selected, and their abbreviations to increase the convenience and concision, are brought as follows:

1. OLS: ordinary least squares (Tao and Hu 2001)
2. RE: ridge estimation (Tao and Hu 2001)
3. LM: Levenberg-Marquardt (Zhou, Jiao, and Long 2012)
4. TSVD: truncated singular value decomposition (Cao and Fu 2018)
5. USS-RFM: uncorrelated and statistically significant RFM (Moghaddam *et al.* 2018b)
6. L1LS: ℓ_1 -norm regularized technique with least squares estimation (Long, Jiao, and He 2015)

Regarding the parameter setting of our proposed method, we empirically set the threshold t to 10^{-2} , providing reasonable results for all data sets. The RE and L1LS methods has a regularization parameter that must be set in prior. According to (Long, Jiao, and He 2015, Tao and Hu 2001), we set these parameters to $10^{-5}/k$ (k is the total number of GCPs) and $10^{-2.5}$ for the L1LS and RE, respectively. The parameters of the USS-RFM method were set according to (Moghaddam *et al.* 2018b) as $\gamma = 10^{-6}$ and $\alpha = 0.2$. To implement the L1LS using Lasso via the LARS algorithm, we used the linear `Mmodel` module from the freely available Scikit-Learn Python package (Pedregosa *et al.* 2011).

Discussion and Results

In this section, we give and then discuss the results of different analyses in three separate subsections. The results of the normal case analysis (NCA) are given in the first subsection. The GCP distribution analysis (GDA) results are reported in the second subsection. The results of the limited number of GCP analysis (LGA) are provided in the last subsection.

Normal Case Analysis

In this analysis, 40 GCPs (which is the least number of GCPs for having a positive degree of freedom) of each data set were selected randomly and the rest served as independent check-points (ICPs). Therefore, only data sets with the minimum required GCPs (i.e., 40) could be used. It means that S1A and S1B were not used here. The results of this analysis are more reliable than two other analyses due to its positive degree of freedom. Root-mean-square-error (RMSE) was calculated over the ICPs as a quality assessment measure. Table 2 shows the results of the NCA.

From Table 2, the first point is the results of the OLS, which are not satisfying at all. This unsatisfactory performance of the OLS, in line with (Long, Jiao, and He 2015, Moghaddam *et al.* 2018b), can be justified by the problems of ill-posedness and overparameterization, which challenge the application of the RFM. Note that in the OLS, no actions are taken to address those problems. This also shows that it is necessary to mitigate these pernicious problems before using RFM.

According to Table 2, OLS has the worst performance in terms of accuracy. Meanwhile, the USS-RFM, L1LS, and the PCA-RFM have an excellent performance in all data sets. The arithmetic mean of RMSEs provided by the proposed method is 0.88 pixel that is lower than those of the L1LS (1.09 pixel)

Table 1. Data set specifications, including GSD, number of CPs, and the reference sources of these points.

Data Set	Platform	GSD (m)	Reference data	Area Type	No. of CPs
HJ	HJ-1	30	Landsat-5	Plain	200
L5	Landsat-5	30	Landsat-5	Mountainous, Hilly	200
PL	Pleiades	0.5	Maps	Urban	70
GE	GeoEye-1	0.5	Maps	Urban	70
WV	WorldView-3	0.5	Maps	Urban	65
S1A	Spot-3 1A	10	DGPS	Rural, Mountainous	28
S1B	Spot-3 1B	10	DGPS	Rural, Mountainous	28
IK	IKONOS	1	Maps	Urban	74
IRS	IRS-P5	2.5	Maps	Semiurban	77

Table 2. NCA report of the proposed PCA-RFM and the competing methods, including OLS, RE, LM, TSVD, USS-RFM, and L1LS. The best result in each data set is given in bold.

Data Set	Methods (RMSE/Pixel)						
	OLS	RE	LM	TSVD	USS-RFM	L1LS	PCA-RFM
HJ	46671.2	4.88	7.16	9.37	0.84	0.63	0.64
L5	57588.53	1.27	7.51	1.27	1.56	0.59	0.59
PL	8075.27	1.66	24.65	1.65	0.85	1.13	0.91
GE	1154.6	1.03	130.01	1.29	0.93	0.66	0.95
WV	1071.31	3.76	17.89	2.98	0.72	1.64	0.72
IK	19995.93	0.92	4.22	0.98	1.67	0.85	1.04
IRS	21492.45	5.3	13.16	2.47	1.28	2.14	1.33
Average	22292.76	2.69	29.23	2.86	1.12	1.09	0.88

and the USS-RFM (1.12 pixel). In order to statistically prove the superiority of the PCA-RFM over the L1LS and USS-RFM, we applied a Mann-Whitney U test.

The Mann-Whitney U test is a statistical procedure used to compare two sets of samples. Each of the PCA-RFM, L1LS, and USS-RFM methods was run ten times to generate a statistically sufficient population. Subsequently, the Mann-Whitney U test was used in order to determine whether the RMSE values resulted from PCA-RFM were significantly different from those of the USS-RFM and L1LS methods.

The test proved that the improvement, resulted from the PCA-RFM, is statistically significant over L1LS and USS-RFM even at the 99% confidence interval. This statistical proof, along with the fact that the average RMSE of the PCA-RFM over the data sets is less than those of the USS-RFM and L1LS, verify the superior performance of the proposed method.

A possible reason for the superiority of the proposed method is the proposed noise reduction phase. As previously mentioned, the ill-posedness problem magnifies the small perturbations of data, caused by random noise or instrumental error, for example. PCs with small eigen values contain noise and undesirable data perturbations. In the proposed method, such PCs are excluded from the design matrix, which reduces the effect of the ill-posedness problem. This is in contrast to the other methods where no action is taken to reduce the data perturbations that are magnified without addressing the ill-posedness problem. Additionally, the applied LS method based on the QR decomposition results in a vector of RPCs with few nonzero elements. Thus, the problem of overparameterization is addressed as the proposed method excludes some unnecessary RPCs from the model.

Regarding the computational time, all the methods were equally fast and were run in a small fraction of a second.

GCPs Distribution Analysis

In the GDA, a modified fivefold cross-validation (MFFCV) was applied to comprehensively evaluate the efficiency of the methods in various distributions of GCPs and ICPs. The MFFCV,

firstly, splits the CPs of each data set into five distinct subsets with approximately the same dimension. Then, in each fold, it allocates one of the five subsets as GCPs and the rest as the ICPs. In each one of the folds, RMSE on ICPs is calculated, and eventually, the average RMSE and standard deviation (STD) over the five folds are reported (Table 3).

In contrast to the regular fivefold cross-validation, in the MFFCV, a higher number of ICPs are used in each fold. Hence, we can better analyze and judge the sensitivity of the methods to the GCP distribution changes. Note that similar to the NCA, S1A, and S1B were not used in the GDA. Due to the poor performance of RE, LM, and TSVD methods in the NCA, these methods were not included in the GDA.

As is apparent from Table 3, the PCA-RFM except for three data sets (i.e., HJ, PL, and IK) has the best performance, which indicates its ability to overcome various distributions significantly. For HJ and IK, the L1LS method has a little bit better performance than the PCA-RFM. However, on average of seven data sets, the PCA-RFM leads to respectively 25.89% and 40.01% improvement in terms of the RMSE and the STD, compared to the L1LS. Considering the results of the USS-RFM, the proposed PCA-RFM achieved a decrease in the RMSE values by 17.90%, on average. It can be concluded that, compared to the competing methods, the proposed method has impressive resistance to changes in the distribution of the GCPs and it is less sensitive than its competitors are.

Note that the result of the USS-RFM in GE case study is marked by an asterisk (*). This means that the USS-RFM could not identify an acceptable RFM in some folds of the MFFCV. In this case, the unacceptable folds were discarded. This also shows that the USS-RFM method is more sensitive to the changes in the GCP distribution than the L1LS and PCA-RFM methods.

Table 3. GDA report of the proposed PCA-RFM, USS-RFM, and L1LS. The best result in each data set is given in bold, and the result of the USS-RFM in the GE case study is marked by an asterisk.

Data Set	Methods (mean RMSE in Pixels \pm STD)		
	USS-RFM	L1LS	PCA-RFM
HJ	0.86 \pm 0.05	0.65 \pm 0.09	0.69 \pm 0.09
L5	1.39 \pm 0.47	0.67 \pm 0.08	0.61 \pm 0.03
PL	1.00 \pm 0.15	2.31 \pm 1.39	1.17 \pm 0.22
GE	1.18 \pm 0.21*	1.70 \pm 0.61	0.98 \pm 0.09
WV	1.14 \pm 0.37	4.29 \pm 2.81	1.05 \pm 0.08
IK	1.86 \pm 0.15	0.95 \pm 0.08	1.39 \pm 0.19
IRS	2.02 \pm 1.20	3.95 \pm 1.64	1.69 \pm 0.18
Average	1.35 \pm 0.37	2.07 \pm 0.95	1.08 \pm 0.12

Table 4. LGA report of the proposed PCA-RFM, USS-RFM, and L1LS. The best result in each data set is given in bold, and the result of the USS-RFM in the GE case study is marked by an asterisk.

Data Set	Methods (mean RMSE in Pixel \pm STD)		
	USS-RFM	L1LS	PCA-RFM
HJ	1.14 \pm 0.34*	0.95 \pm 0.05	1.26 \pm 0.12
L5	3.70 \pm 1.22*	1.49 \pm 0.37	1.33 \pm 0.16
PL	1.48 \pm 0.73	1.46 \pm 0.73	1.15 \pm 0.23
GE	1.07 \pm 0.15*	1.45 \pm 0.33	1.15 \pm 0.34
WV	1.71 \pm 0.46	3.70 \pm 2.47	1.23 \pm 0.19
IK	5.11 \pm 3.98	1.22 \pm 0.22	1.49 \pm 0.19
IRS	2.91 \pm 3.28	8.13 \pm 12.95	1.78 \pm 0.30
S1A	1.18 \pm 0.37*	3.83 \pm 3.29	1.14 \pm 0.28
S1B	0.91 \pm 0.01*	2.24 \pm 1.23	1.14 \pm 0.26
Average	2.13 \pm 1.17	2.71 \pm 2.40	1.30 \pm 0.23

Limited Number of GCPs Analysis

The objective of the LGA is to evaluate the performance of the proposed and competing methods when a small number of GCPs are available. To accomplish this, we randomly selected ten GCPs. Furthermore, this selection was made five times to challenge the performance of the methods for changes in the GCP distribution. Results of this analysis are given in Table 4, where mean and STD of RMSEs are reported in mean \pm STD format. Similar to the GDA, RE, LM, and TSVD methods did not take part in the LGA.

From Table 4, on average, the PCA-RFM has shown 29.29% and 39.57% improvement in the average RMSEs and STDs, respectively, compared to the L1LS. Considering the second and fourth columns of Table 4, the PCA-RFM method leads to 20.52% improvement, on average, in terms of the mean RMSE values compared to the USS-RFM. Similar to the previous section, the results of the USS-RFM in some case studies are marked by an asterisk. Because acceptable results could not be achieved by this method in some rounds of the LGA.

In the LGA, the competing methods provided a poor performance in comparison to the PCA-RFM. It supports a conclusion that the PCA-RFM achieves more accurate results than the rivals when few GCPs are available. In addition, the dependency of the proposed method on the GCP distribution is less than the other methods as it resulted in smaller STD values.

Conclusion

In this paper, we have presented a novel two-step method based on the integration of PCA and QR decomposition, mainly attempting to deal with the ill-posedness problem. In the first step, the PCA-RFM method uses the PCA to reduce the noise and other data perturbations from the design matrix, leading to a noise-reduced but rank deficient design matrix. In the second step, the PCA-RFM applies the QR decomposition to solve the rank deficient LS problem and estimate the unknown RPCs.

Evaluating the feasibility of the PCA-RFM, we designed three analyses: NCA, GDA, and LGA. Geometrically speaking, the NCA showed that PCA-RFM was about 7% and 16% more geometrically accurate than the L1LS and USS-RFM methods, respectively. Note that this improvement was statistically significant at a 99% significance level. In the GDA, the method's dependency on GCP distribution was investigated, using a fivefold cross-validation approach. The results proved that the proposed method was less sensitive to changes in the GCP distribution.

Finally, the performance of the PCA-RFM and the other competing methods in the presence of small numbers of GCPs was evaluated in the LGA. LGA's results demonstrated that the PCA-RFM was geometrically 29.29% and 20.52% more accurate than the L1LS and USS-RFM methods, respectively. From the LGA, it can be concluded that the PCA-RFM is a more effective solution in the case that a small number of GCPs are available.

As with any new approach, there are some unresolved issues that may present challenges over time. One might be the setting of the threshold t in the first step of the PCA-RFM. The automatic selection of t could be a topic for future research.

Acknowledgements

The authors would like to thank Dr. T. Long from the Chinese Academy of Sciences, Beijing, China, for his help in the implementation of L1LS method and providing HJ and L5 data sets. They would like to thank Prof. M. J. V. Zoej from the K. N. Toosi University of technology, Tehran, Iran, and Dr. S. Homayouni from the University of Ottawa, Ottawa, ON, Canada for providing some data sets in the case studies.

References

- Aytas, N., E. Afacan and E. Tuna. 2017. Analysis of the incoming signal on the antenna array using singular value decomposition. Pages 18–21 in *Proceedings of ISER 56th International Conference*, held in Rome, Italy.
- Cao, J., J. Fu, X. Yuan and J. Gong. 2017. Nonlinear bias compensation of ZiYuan-3 satellite imagery with cubic splines. *ISPRS Journal of Photogrammetry and Remote Sensing* 133:174–185.
- Cao, J. and J. Fu. 2018. Estimation of rational polynomial coefficients based on singular value decomposition. *Journal of Applied Remote Sensing* 12 (4):044003.
- Gholinejad, S., A. A. Naeini and A. Amiri-Simkooei. 2018. Robust particle swarm optimization of RFMs for high-resolution satellite images based on K-fold cross-validation. *IEEE Journal of Selected Topics in Applied Earth Observations and Remote Sensing*.
- Golub, G. H. and C. F. Van Loan. 2012. *Matrix Computations*. JHU Press.
- Li, C., X. Liu, Y. Zhang and Z. Zhang. 2017. A stepwise-then-orthogonal regression (STOR) with quality control for optimizing the RFM of high-resolution satellite imagery. *Photogrammetric Engineering & Remote Sensing* 83 (9):611–620.
- Li, C., J. Liu, X. Wang, X. Liu and Y. Wu. 2018. Stepwise-then-intelligent algorithm (STIA) for optimizing remotely sensed image rectification. *International Journal of Remote Sensing*: 1–20.
- Long, T., W. Jiao and G. He. 2015. RPC estimation via l_1 -norm-regularized least squares (L1LS). *IEEE Transactions on Geoscience and Remote Sensing* 53 (8):4554–4567.
- Ma, R. 2013. Rational function model in processing historical aerial photographs. *Photogrammetric Engineering & Remote Sensing* 79 (4):337–345.
- Moghaddam, S. H. A., M. Mokhtarzade, A. A. Naeini and Moghaddam, S. A. A., 2017. Statistical method to overcome overfitting issue in rational function models. *International Archives of the Photogrammetry, Remote Sensing & Spatial Information Sciences* 42:23–26.
- Moghaddam, S. H. A., M. Mokhtarzade and S. A. A. Moghaddam. 2018a. Optimization of RFM's structure based on PSO algorithm and figure condition analysis. *IEEE Geoscience and Remote Sensing Letters* 15 (8):1179–1183.
- Moghaddam, S. H. A., M. Mokhtarzade, A. A. Naeini and A. Amiri-Simkooei. 2018b. A statistical variable selection solution for RFM ill-posedness and overparameterization problems. *IEEE Transactions on Geoscience and Remote Sensing* 56 (7):3990–4001.
- Naeini, A. A., S. H. A. Moghaddam, S. M. J. Mirzadeh, S. Homayouni and S. B. Fatemi. 2017. Multiobjective genetic optimization of terrain-independent RFMs for VHSR satellite images. *IEEE Geoscience and Remote Sensing Letters* 14 (8):1368–1372.
- Pedregosa, F., G. Varoquaux, A. Gramfort, V. Michel, B. Thirion, O. Grisel, M. Blondel, P. Prettenhofer, R. Weiss and V. Dubourg. 2011. Scikit-learn: Machine learning in Python. *Journal of Machine Learning Research* 12 (Oct):2825–2830.
- Tao, C. V. and Y. Hu. 2001. A comprehensive study of the rational function model for photogrammetric processing. *Photogrammetric Engineering and Remote Sensing* 67 (12):1347–1358.
- Tengfei, L., J. Weili and H. Guojin. 2014. Nested regression based optimal selection (NRBOS) of rational polynomial coefficients. *Photogrammetric Engineering & Remote Sensing* 80 (3):261–269.
- Zhou, Q., W. Jiao and T. Long. Solution to the rational function model based on the Levenberg-Marquardt algorithm. Pages 2795–2799 in *Proceedings of the 2012 9th IEEE International Conference on Fuzzy Systems and Knowledge Discovery (FSKD)*.

WHO'S WHO IN ASPRS

BOARD OF DIRECTORS

BOARD OFFICERS

President

Thomas Jordan, Ph.D.
University of Georgia

President-Elect

Jeff Lovin
Woolpert

Vice President

Jason M. Stoker, Ph.D.
U.S. Geological Survey

Past President

Anne Hillyer, CP
Bonneville Power Administration (USDOE)

Treasurer

Stewart Walker, Ph.D.

Secretary

Roberta E. Lenczowski

BOARD MEMBERS

Sustaining Members Council – 2019

Chair: Joe Cantz

Vice Chair: TBA

www.asprs.org/About-Us/Sustaining-Members-Council.html

Early-Career Professionals Council – 2020

Chair: Peng Fu

Vice Chair: TBA

Region Officers Council – 2021

Chair: Lorraine B. Amenda, PLS, CP

Vice Chair: Demetrio Zourarakas

Student Advisory Council – 2020

Chair: Victoria Scholl

Vice Chair: TBA

<http://www.asprs.org/Students/Student-Advisory-Council.html>

Technical Division Directors Council – 2020

Chair: John McCombs

Vice Chair: Bandana Kar, Ph.D.

TECHNICAL DIVISION OFFICERS

Geographic Information Systems Division – 2021

Director: Xan Fredericks

Assistant Director: Denise G. Theunissen
www.asprs.org/Divisions/GIS-Division.html

Lidar Division – 2020

Director: Amar K. Nayegandhi, CP, CMS

Assistant Director: Joshua Nimetz, CMS
www.asprs.org/Divisions/Lidar-Division.html

Photogrammetric Applications Division – 2020

Director: Paul C. Bresnahan

Assistant Director: Kurt Rogers
www.asprs.org/Divisions/Photogrammetric-Applications-Division.html

Primary Data Acquisition Division – 2021

Director: Jon Christopherson

Assistant Director: J. Chris Ogier
www.asprs.org/Divisions/Primary-Data-Aquisition-Division.html

Professional Practice Division – 2022

Director: Harold W. Rempel, III, CP

Assistant Director: TBA
www.asprs.org/Divisions/Professional-Practice-Division.html

Remote Sensing Applications Division – 2020

Director: David W. Kreighbaum

Assistant Director: Raechel A. White, Ph.D.
www.asprs.org/Divisions/Remote-Sensing-Applications-Division.html

Unmanned Autonomous Systems (UAS) – 2020

Director: Benjamin Vander Jagt, Ph.D.

Assistant Director: Megan Miller, Ph.D.

REGION PRESIDENTS

Alaska Region

David Parret

<http://www.asprsalaska.org/>

Cascadia Region

TBA

<http://columbia.asprs.org/CRR/>

Central New York Region

John Boland, C.P.

<http://www.esf.edu/asprs/>

Eastern Great Lakes Region

Edward Kunz, GISP

<http://egl.asprs.org/>

Florida Region

Erin McCormick

<http://florida.asprs.org/>

Heartland Region

Paul Manley

<http://heartland.asprs.org/>

Intermountain Region

TBA

<http://asprsimountain.weebly.com/>

Mid-South Region

Dr. David Hughes

<https://www.asprs.org/all-regions/mid-south.html>

New England Region

TBA

<http://neweng.asprs.org/>

North Atlantic Region

Richard W. Carlson, Jr., P.L.S., C.P.

<http://natlantic.asprs.org/>

Pacific Southwest Region

Riadh Munjy, Ph.D.

<https://pswasprs.org/>

Potomac Region

Jackie Carr

<http://www.asprspotomac.org/>

Rocky Mountain Region

Jeffrey M. Young

<http://www.asprs-rmr.org/>

Western Great Lakes Region

Kirk Contrucci, CP

<http://wgl.asprs.org/>

3D Iterative Spatiotemporal Filtering for Classification of Multitemporal Satellite Data Sets

Hessah Albanwan, Rongjun Qin, Xiaohu Lu, Mao Li, Desheng Liu, and Jean-Michel Guldmann

Abstract

The current practice in land cover/land use change analysis relies heavily on the individually classified maps of the multitemporal data set. Due to varying acquisition conditions (e.g., illumination, sensors, seasonal differences), the classification maps yielded are often inconsistent through time for robust statistical analysis. 3D geometric features have been shown to be stable for assessing differences across the temporal data set. Therefore, in this article we investigate the use of a multitemporal orthophoto and digital surface model derived from satellite data for spatiotemporal classification. Our approach consists of two major steps: generating per-class probability distribution maps using the random-forest classifier with limited training samples, and making spatiotemporal inferences using an iterative 3D spatiotemporal filter operating on per-class probability maps. Our experimental results demonstrate that the proposed methods can consistently improve the individual classification results by 2%–6% and thus can be an important postclassification refinement approach.

Introduction

In land cover/land use change mapping, obtaining consistent data and classification results is critical for remote sensing applications and time-series analysis. Varying acquisition conditions—such as meteorological conditions, viewing angles, sun illumination, and sensor characteristics—largely affect the radiometric consistency through different temporal data sets. State-of-the-art satellite imaging platforms, including the Ikonos (1999, decommissioned), GeoEye-1 (2008), and WorldView satellite constellations, are able to collect very-high-resolution (VHR) multispectral images, with a spatial resolution that reaches as high as 0.3 m, which dramatically increases the capability to interpret and monitor land surfaces and urban/natural dynamics at a high level of detail. For instance, VHR imagery is much less affected by mixed-pixel effects than are low-resolution images, allowing information extraction to be carried out on an individual-object basis, such as shapes, sizes, and patterns of buildings, trees, roads, and so on. This certainly brings advantages for manual interpretation, but

Hessah Albanwan and Xiaohu Lu are with the Geospatial Data Analytics Laboratory, Department of Civil, Environmental and Geodetic Engineering, The Ohio State University, Columbus, OH 43210.

Mao Li is with the Department of Electrical and Computer Engineering, The Ohio State University, Columbus, OH 43210.

Rongjun Qin is with the Geospatial Data Analytics Laboratory, Department of Civil, Environmental and Geodetic Engineering, and the Department of Electrical and Computer Engineering, The Ohio State University, Columbus, OH 43210 (qin.324@osu.edu).

Desheng Liu is with the Department of Geography, The Ohio State University, Columbus, OH 43210.

Jean-Michel Guldmann is with the Knowlton School of Architecture, The Ohio State University, Columbus, OH 43210.

Unfortunately the algorithmic development of automatic interpretation has not yet achieved equivalent advancement. As a result, the large volume of data to be robustly interpreted brings a data crisis for operators and decision-makers when enjoying the high resolution. The major technical challenge in classification/detection algorithms on VHR data is to overcome the low intraclass (within-class) similarity and interclass (between-classes) separability (Salehi, Zhang and Zhang 2011). As the spectral ambiguities of VHR images increase, the scene contents become more complex (Qin and Fang 2014)—for instance, as the images are clear enough to reflect individual objects such as buildings, pavements, ground, roads, and so on (Kotthaus *et al.* 2014), it is possible that these object classes may reflect similar spectral responses, since they are mainly made of similar materials (e.g., concrete). Therefore, classification algorithms considering spectral information alone might likely yield misclassifications (Lu, Hetrick and Moran 2010). Shape information of the objects in addition to the spectral responses may bring more discriminative powers, and relevant methods have achieved considerable improvement (Ghamisi, Dalla Mura and Benediktsson 2015; Qin 2015). However, such methods often suffer from unreliable segmentation and inconsistent spectral information, and they can be particularly vulnerable when applied to multitemporal data sets, where the varying spectral responses affect both segmentation and classification.

Existing studies have shown that integrating the spectral and 3D geometric information (e.g., height, depth) reduces the uncertainty of classification and change detection for objects with similar spectral characteristics (Chaabouni-Chouayakh *et al.* 2010; MacFaden *et al.* 2012; Qin, Tian and Reinartz 2016). Unlike image information, where appearances vary over time due to illumination and acquisition conditions, height information is relatively robust, providing more valuable information for multitemporal data comparison. With the growing number of optical satellite sensors in operation, the possibilities for satellites to view an area from multiple angles have dramatically increased. This presents digital surface models (DSMs) generated from such multiview or stereo-view data as common sources for mapping and monitoring. Compared to a typical lidar-based DSM, satellite-derived DSMs are more affordable and can capture images of regions inaccessible by aerial vehicles, but they present a higher level of noise. Thus, to better utilize such DSM data, the uncertainties of the data and the derived results (i.e., classification) need to be well accounted for.

In this article, we introduce a 3D iterative spatiotemporal filter that applies probability inference to refine land cover classification results of VHR multitemporal data. The proposed iterative spatiotemporal filter further extends past work (Albanwan and Qin 2018), which showed that a single-step

Photogrammetric Engineering & Remote Sensing
Vol. 86, No. 1, January 2020, pp. 23–31.
0099-1112/20/23–31

© 2020 American Society for Photogrammetry
and Remote Sensing
doi: 10.14358/PERS.86.1.23

spatiotemporal filter has the capability to improve the spectrum consistency across a multitemporal data set. The proposed method further enhances such capability for multimodal time-series data (i.e., spatial, spectrum, and height) for classification problems, which may achieve higher classification accuracy through inference through a multitemporal data set rather than independently classified images. Our proposed method is applied to per-class probability maps and can adaptively reduce the heterogeneity of the probability maps, leading to more consistent classification results through time. The rest of this work is organized as follows: The next section briefly introduces relevant works and the rationale of our proposed work. After that, we present the proposed 3D iterative spatiotemporal filter. The experimental results and evaluations are shown in the following section. The final section concludes by discussing the effectiveness and limitations of our work, and potential future improvements.

Related Works and Rationale

The proposed work aims to enhance classification accuracy through inferring information across multitemporal data sets, and thus is very relevant to both classification problems and multitemporal data processing in a land use/land cover change (LULCC) context. Therefore, this section briefly summarizes both of these two relevant topics.

Related Works

Classification of VHR Satellite Images

VHR image classification has been intensively investigated in remote sensing (Fauvel *et al.* 2013). Traditional classification methods are categorized into pixel- or object-based methods. In most cases, object-based methods perform reasonably better on VHR images due to the availability of the spatial information that allows use of patterns and local regions, which are often hard to obtain through pixel-based approaches (Weih and Riggan 2010; Chen *et al.* 2011; Keyport *et al.* 2018). The major challenge in classifying multitemporal VHR data sets is obtaining consistent classification maps through time, which can be difficult due to varying factors such as season changes, atmosphere, and acquisition conditions. Object-based methods often require segmentation of the image to extract spatial information (Qin *et al.* 2015). However, improper segmentation parameters can lead to under- or oversegmentation, which affects classification accuracy. Incorporating 3D geometric information (i.e., height) can provide more accurate, robust, and stable solutions, since the height of objects is insensitive to spectral variations (Minh and Hien 2011; MacFaden *et al.* 2012; Qin *et al.* 2016). Including height in the classification involves fusing multisource data (i.e., spectral and height information; Huang, Zhang and Gong 2011; Salehi *et al.* 2011; Kim 2016), which can be performed at either the pixel, feature, or decision level (J. Zhang 2010). One of the challenges in including height in classification is its source and quality. For instance, DSMs are either generated from direct measurements from sensors like lidar or computed using modern photogrammetric techniques (e.g., stereo matching). Although in general lidar data are more accurate, DSMs derived from images are preferred in many studies due to their higher availability and lower cost (Salehi *et al.* 2011). Stereo-matching algorithms used to generate DSMs depend on the quality of the pair of images and their acquisition conditions, and thus may result in certain noises and uncertainties (Minh and Hien 2011). Current approaches mostly adapt statistical assumptions to the noises and either introduce new sources of data by fusing information from multispectral images or perform empirical statistical filtering (e.g., morphological processing; Chaabouni-Chouayakh *et al.* 2010; Moser, Serpico

and Benediktsson 2013; Qin *et al.* 2015), which is capable of reducing certain noises although is still problematic when the content of the scene is complex (Fu 2011; Yan, Shaker and El-Ashmawy 2015).

Spatiotemporal Inferences of Land Use/Land Cover Change Maps

Land use/land cover change products are highly dependent on the quality of land cover classification maps. Inconsistencies and uncertainties in the classification maps due to the varying data spectra can negatively influence applications that directly rely on them, such as time-series analysis, change detection, object recognition, and modeling. In such a context, improving single-date classification may, on one hand, require ad hoc techniques specifically tailored for factors influencing the images and might, on the other hand, not yield optimally consistent classification maps through time. In this regard, spatiotemporal inference approaches applied on the images or classification results can be particularly effective, as they simultaneously homogenize information in both spatial and temporal directions (Floberg and Holden 2013). Current spatiotemporal inference models are categorized into local, nonlocal, and global models.

Local and nonlocal methods are more efficient in terms of computational complexity, since they operate over small pixel neighborhoods and local regions (Floberg and Holden 2013). For instance, Cheng *et al.* (2017) have proposed a spatial and temporal nonlocal filter-based fusion model to predict the land cover class for every pixel based on the spectral values through a weighted sum of the neighboring pixels in the data set. Albanwan and Qin (2018) proposed a local spatiotemporal bilateral filter as a preprocessing step for multitemporal images to enhance their radiometric characteristics and consistency for classification. Global approaches for spatiotemporal inference are mainly based on probabilistic graphical models and Markov random fields, which model each pixel as a statistical variable where local smoothness and global consistency serve as objectives when performing maximal likelihood estimation (Kasetkasem and Varshney 2002; Liu and Cai 2012; Gu, Lv and Hao 2017). Such inference algorithms help to generate more consistent change maps and prevent noise caused by inaccurate classification results. The solution for such inference algorithms usually uses fixed spatial-weight parameters, which might potentially lead to oversmoothing for the change maps. Gu *et al.* (2017) have proposed a linear weighting scheme, where the spatial weights are estimated adaptively for every pixel based on its changed, unchanged, or uncertain-change status. Although global methods used in change detection (such as Markov random fields) provide high-quality results, they involve per-pixel processing, which increases the computational complexity exponentially as the number of pixels and time-series data increase.

Proposed Method and Rationale

The goal of this work is to achieve an efficient spatiotemporal inference model that allows accurate land use/land cover mapping. Inspired by work by Albanwan and Qin (2018), where a 3D spatiotemporal filter was developed for classification of images using spectral, spatial, and temporal knowledge, we propose here a simple but effective extension leading to a 3D iterative spatiotemporal filter. Using global methods for per-pixel classification is a time-consuming process. Krähenbühl and Koltun (2011) suggest using iterative approaches through local filters to approximate global inferences, with the benefit of reducing computational costs. Therefore, we apply here an iterative approach that filters the probability maps along with the corresponding DSMs in an iterative fashion to achieve optimal classification results. Figure 1 illustrates our rationale of using spatiotemporal filtering: Given three per-class probability maps generated from

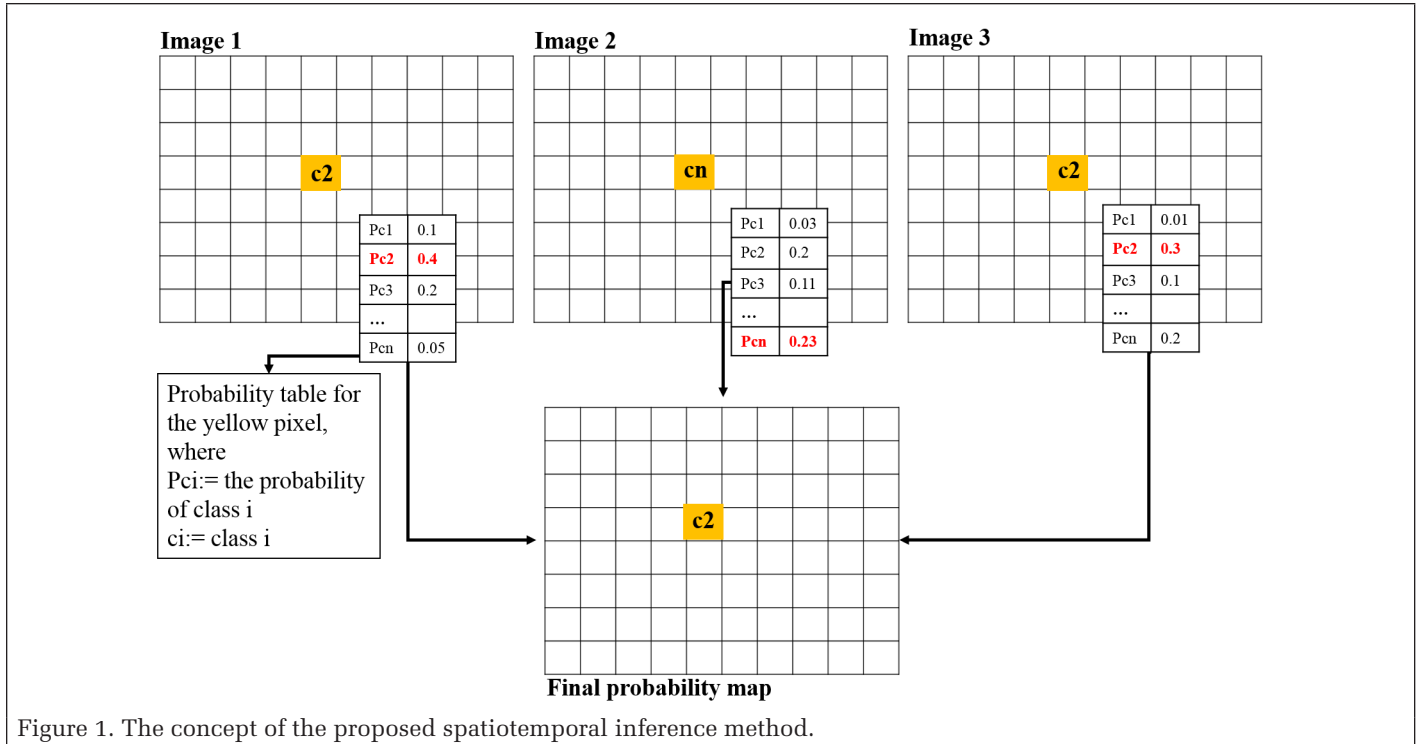


Figure 1. The concept of the proposed spatiotemporal inference method.

three temporal data sets, the highest probability normally determines the class of the pixel (represented as c_i for the i th class). In the first and third images, the yellow pixel is classified as the second class c_2 and the second image is classified as c_n . Knowing that, then if the feature of the central pixel in the second image is dissimilar to that of the first and the third, this central pixel in the second image can be a misclassification. Probability inferences in the temporal direction might help correct such errors by providing higher confidence in the correct class. Our proposed iterative solution is expected to perform such probability inferences in a global sense, to refine and improve the consistency of the classification maps and their accuracy.

Methodology

Our workflow consists of three main steps (Figure 2): data preprocessing of multitemporal stereo satellite images, object-based classification, and 3D iterative filtering for spatiotemporal inference. In this section, we provide an overview of the first two steps and emphasize details of the third, wherein our main technical contribution lies. The preprocessing step mainly consists of DSM and orthophoto generation and registration using stereo satellite images. Once the DSM and orthophotos are registered, we take advantage of their differences to infer training labels from one temporal data set to others, and then utilize these labels to train random-forest classifiers individually to generate initial and per-class probability maps. These probability maps are then fed into our proposed 3D iterative spatiotemporal filter, where probability maps are globally inferred (concept as per described in Figure 1) as the final probability map. We assess the classification results by estimating the overall accuracy of each iteration.

Data Preprocessing

The preprocessing stage involves the generation of the DSM and orthophoto data sets, precise geometric alignment of the data, and normalization to nDSM. We generate high-quality DSMs and orthophotos of the related satellite image pairs using RPC Stereo Processor (Qin 2016), which adopts a hierarchical

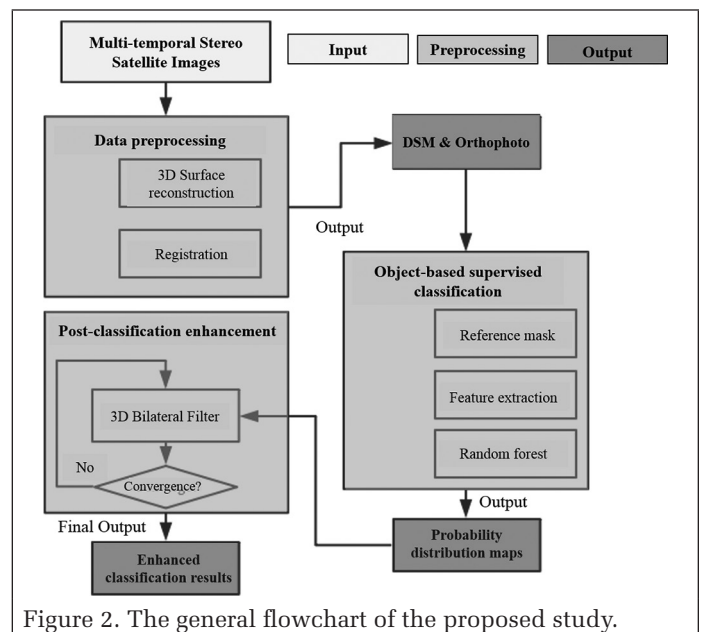


Figure 2. The general flowchart of the proposed study.

semiglobal matching method (Hirschmüller 2005). Hierarchical semiglobal matching offers a great benefit in being computation and time efficient; it reduces memory consumption by searching only a limited number of disparity ranges. Due to systematic satellite positioning error, the generated DSMs and orthophotos may not be well aligned. Co-registration of a DSM requires estimating the transformation parameters (rotation and translation) between the reference and target DSMs, as described by Gruen and Akca (2005). Since the rotation differences for a satellite overview data set are often regarded as negligible (Waser *et al.* 2008), we can then compute only the shift parameters in three directions x , y , and z . Using a simple approximation to least-squares surface matching (Gruen and Akca 2005), we estimate the shift parameters that minimize the sum of squared Euclidean distances. We eliminate the systematic error

by discarding the potential noise and outliers due to the DSM generation process by applying a threshold (in our experiment we used 6 m with an empirical estimation of the height uncertainties), which regards points with an error greater than the threshold as outliers and discards them for error computation. Finally, we generate nDSM using a morphological top-hat reconstruction strategy as explained by Qin and Fang (2014).

Object-Based Classification and Initial Probability-Map Generation

Training Label Generation Through Empirical Inferences

Since generating training labels for every image of different dates is tedious and time-consuming, we simplify this process by propagating training samples for the entire data set through an intuitive and automated training-label mask generation approach. This empirically sets thresholds for image/DSM differences to determine whether or not to keep certain training labels from a labeled image of one date through time: Given a labeled image (i.e., the reference map), our automated method utilizes preliminary features such as nDSM and the normalized difference vegetation index as change indicators and determines if a pixel in the labeled images should be kept in the other temporal data set. The nDSM offers higher robustness against spectral variations that result from different illumination and atmospheric disturbances between the multitemporal data. This is equivalent to an intuitive threshold-based change detection method, where differences in both nDSM and the normalized difference vegetation index are used as indicators. Theoretically, these training labels should be generated manually for each data set, to ensure that they are evenly distributed and well balanced. In our procedure, this is ad hoc and can vary with data sets. However, we do set conservative thresholds to ensure minimal label inference errors, and we are aware that such a labeling mechanism may lead to suboptimal training-label sets. We therefore have verified the training labels generated and have performed the necessary manual refinement.

Feature Extraction, Classification, and Probability-Map Generation

Per-class probability (sometimes called confidence) maps are important to determine the class membership of each data point. This is provided by most of the statistical classifiers: For example, support-vector machines weight the distances of the output to the support boundaries, and random forests compute the probability by counting the votes from all the decision trees forming the forest. In our experiment, we use the random-forest classifier (Breiman 2001) and adopt an object-based classification approach, where mean shift (Comaniciu 2002) is used as the segmentation approach due to its wide use in relevant applications. The spectral feature is computed using principal-component analysis on the spectrum bands. We have also considered spatial features extracted from the DSMs and orthophotos as part of the feature vector, which includes dual morphological profiles and morphological top-hat reconstruction (Qing Zhang 2006; Qin *et al.* 2015). Details of these features are shown in Table 1.

As discussed, the random-forest classifier is an ensemble classifier that decides the labels based on the number of votes per class among the decision trees, and the normalized voting numbers (rationing the total number of votes) are then used as the probability/chance that a segment or pixel belongs to a

specific class; 500 decision trees were used in our experiment, and their per-class probability maps yield in total N (number of classes) probability maps for each temporal data set.

The Proposed 3D Iterative Spatiotemporal Filter for Probability Inference

The proposed filter is based on a 3D spatiotemporal bilateral filter (Albanwan and Qin 2018), the general form of which is represented as

$$P_{\text{new}}(x_j, y_j, t_m) = \frac{1}{N * T} \sum_{j \in N, n \in T} W_{3D}(x_j, y_j, t_n) * P(x_j, y_j, t_n), \quad (1)$$

where N denotes the spatial neighborhood centered on point (x_i, y_i) and T refers to the number of observations (dates) through time; $P(x, y, t_n)$ is the probability of the pixel at location (x, y) in the probability map taken on date t_n ; and W_{3D} are adaptive weights that consider spectral, spatial, and temporal differences in the data sets. Since in our context the DSM data are available and regarded as robust to illumination changes, we hereby take the nDSM differences as means of weighting the temporal coherences for probability inference. Thus, the weight W_{3D} can be decomposed into three components:

$$W_{3D} = W_{\text{spatial}} * W_{\text{spectral}} * W_{\text{nDSM}}, \quad (2)$$

where

$$W_{\text{spatial}}(x_j, y_j, t_n) = e^{-\frac{\|x_i - x_j\|^2 + \|y_i - y_j\|^2}{2\sigma_s^2}} \quad (3)$$

$$W_{\text{spectral}}(x_j, y_j) = e^{-\left(\frac{\|I(x_i, y_i) - I(x_j, y_j)\|^2}{2\sigma_r^2}\right)}. \quad (4)$$

The σ_s , σ_r , and σ_h parameters are the spatial, spectral, and elevation/temporal bandwidths of the weighted filter; $I(x_i, y_i)$ refers to the values of the color image (transformed color space); and nDSM refers to the normalized height values. In the spatial and spectral domains, the pixels are weighted based on their closeness and spectral similarities to the central pixel in a defined window, where larger weights are assigned to spectrally similar and spatially proximate pixels (and vice versa). The value of σ_s is empirically determined based on the size of the window; a large value can lead to an overly smoothed image with blurry edges. The parameter σ_r serves as the spectral bandwidth of a typical bilateral filter to allow edge-aware filtering (Tomasi and Manduchi 1998). CIELAB color is used as the transformed color space for computing the spectral differences, where three bands (near-infrared, red, and green) are used for the color transformation (Joblove and Greenberg 1978; Tomasi and Manduchi 1998). The height variation is class-dependent: For example, the ground class normally has smaller variations, thus it should have a smaller bandwidth to penalize larger weight for incorporating changed areas in the filtering processing. Also, tree classes normally have a higher uncertainty, and thus a larger bandwidth is needed to average out noises. Therefore, the relevant

Table 1. Extracted features used for classification, the light boxes are types of features, and the dark boxes under the same columns provide additional details.

Principal-Component Analysis (PCA)	Dual Morphological Profiles (DMP) and Morphological Top-Hat Reconstruction of Digital Surface Model	Adaptive Structural Elements
All columns from PCA of the spectrum (which includes only the RGB bands) of segment S (Wold <i>et al.</i> 1987; Jolliffe 2005).	The radius sequence of disk shape used in morphological profile reconstruction [24 146 260] pixels.	Used to construct DMP and address the problem of multiscale information of segments (Qian Zhang <i>et al.</i> 2015).
	DMP of the first component from PCA in the first feature.	
	DMP for the color inverse with the first component from PCA in the first feature.	

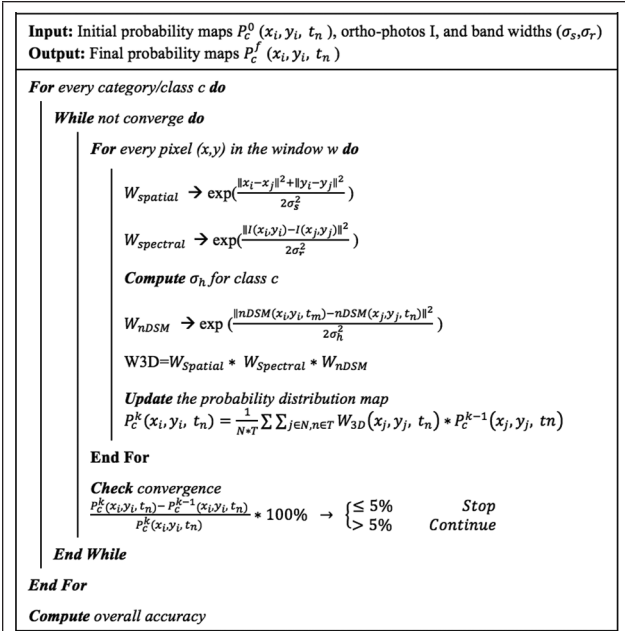


Figure 3. Pseudocode of the proposed 3D iterative spatiotemporal filter.

bandwidth σ_h here is estimated per class to achieve optimal performance. The height range of each class is approximated by the labeled pixels in each of the training labels; for a certain class c , the elevation bandwidth σ_h and the relevant weight are computed using the following equations:

$$\sigma_h = \left(\frac{70\%}{2}\right) * [\text{value range of nDSM of class } c] \quad (5)$$

$$W_{nDSM}(x_j, y_j, t_n) = e^{-\frac{\|nDSM(x_i, y_i, t_m) - nDSM(x_j, y_j, t_n)\|^2}{2\sigma_h^2}} \quad (6)$$

The 70% value comes from the consideration that the height measurements from stereo-matching introduce noise. We therefore take the one-sigma rule to determine σ_h and, by assuming the height-difference variation as a zero-centered Gaussian distribution, compute the one-sigma interval as 68.27% & 70% of the nDSM. These all together give the final form of the 3D weight as

$$W_{3D}(x_j, y_j, t_n) = e^{-\left(\frac{\|x_i - x_j\|^2 + \|y_i - y_j\|^2}{2\sigma_s^2} + \frac{\|I(x_i, y_i) - I(x_j, y_j)\|^2}{2\sigma_r^2} + \frac{\|nDSM(x_i, y_i, t_m) - nDSM(x_j, y_j, t_n)\|^2}{2\sigma_h^2}\right)} \quad (7)$$

This 3D weighted filter performs local spatiotemporal filtering in a limited receptive field for each pixel. To achieve optimal probability maps, we further globalize the inference algorithm through iterative application to probability maps. The iterative filtering is global by means of gradually propagating information from locally processed cells to wider receptive fields. We use the probability maps generated from the random-forest classifier (as described in the previous subsection) as the initial probability maps (see Figure 4) for inference. For each date, there will be in total n (number of classes) probability maps, and the spatiotemporal inference is performed on probabilities of the same classes. In the filtering process, the total weight W_{3D} for each pixel is constant through all iterations, since it is a function of the spectral,

Table 2. List of satellite stereo images used in this work.

Satellite	Date	Resolution (Panchromatic; m)	Resolution (Multispectral; m)
Ikonos	3/22/2007 (on track)	0.82	3.28
GeoEye-1	1/16/2010 (on track)	0.41	1.84
Ikonos	6/6/2010 (on track)	0.82	3.28
Ikonos	12/21/2010 (on track)	0.82	3.28
GeoEye-1	3/8/2012 (on track)	0.41	1.84
GeoEye-1	9/11/2013 (on track)	0.41	1.84
WorldView	7/24/2014 (on track)	0.46	1.84
GeoEye-1	6/23/2015, 7/1/2015	0.41	1.84

spatial, and height information of the image. The probability maps are updated in each iteration:

$$P_c^k(x_i, y_i, t_n) = \frac{1}{N * T} \sum_{j \in N, n \in T} W_{3D}(x_j, y_j, t_n) * P_c^{k-1}(x_j, y_j, t_n), \quad (8)$$

where $P_c^k(x_i, y_i, t_n)$ is the estimated probability of pixel (x_i, y_i) at date t_n , in class c , on the k th iteration, derived from the probability $P_c^{k-1}(x_i, y_i, t_n)$ on iteration $(k - 1)$. We compute this iterative process until the difference between P_c^{k-1} and P_c^k is smaller than a threshold, which in this work is set as 5% of relative changes:

$$\text{convergence criterion} = \frac{P_c^k(x_i, y_i, t_n) - P_c^{k-1}(x_i, y_i, t_n)}{P_c^k(x_i, y_i, t_n)} * 100\% < 5\% \quad (9)$$

We take the processed probability map and determine the class label for every pixel as the one with the highest probability. Using the ground-truth data, we can evaluate the accuracy of the resulting classification maps to understand how the proposed iterative spatiotemporal filter improves the results. The computational complexity for every iteration is $O(WHT)$, where W and H are the width and height of the probability map and T is the number of temporal data. Figure 3 presents the pseudocode of the algorithm.

Experimental Results

Data Description

The data set used in our experiment is a multitemporal data set in Port-au Prince, Haiti, through the 2010 earthquake, when a catastrophic earthquake with magnitude 7.0 M_w caused a large number of fatalities and extreme damages to the area, forcing Haitians to migrate into temporary (tents) and long-term lodging (i.e., shelters last for a longer time for accommodations). Therefore, our classification work particularly includes changes in buildings with different functionalities (i.e., long-term lodgings, temporary lodgings, and normal built-up areas). The satellite data set contains seven on-track stereo pairs (data collected on the same day with the satellite on the same track) from 2007 to 2014 and one incidental image pair in 2015 over Port-au-Prince, Haiti, with data-acquisition date and details shown in Table 2.

We selected three test regions with a size of 1×1 km² (i.e., 2001×2001 pixels for images resampled at 0.5 m GSD (Ground Sampling Distance) in various urban scenes (see Figure 4 for details). Test region 1 is an open area around the airport in which refugees and the government built up their temporary and long-term lodgings spontaneously. We consider seven classes in the classification: buildings, ground, trees, roads, grass, temporary lodging, and long-term lodging (see Figure 4). The three test regions vary in terms of their urban forms: Test

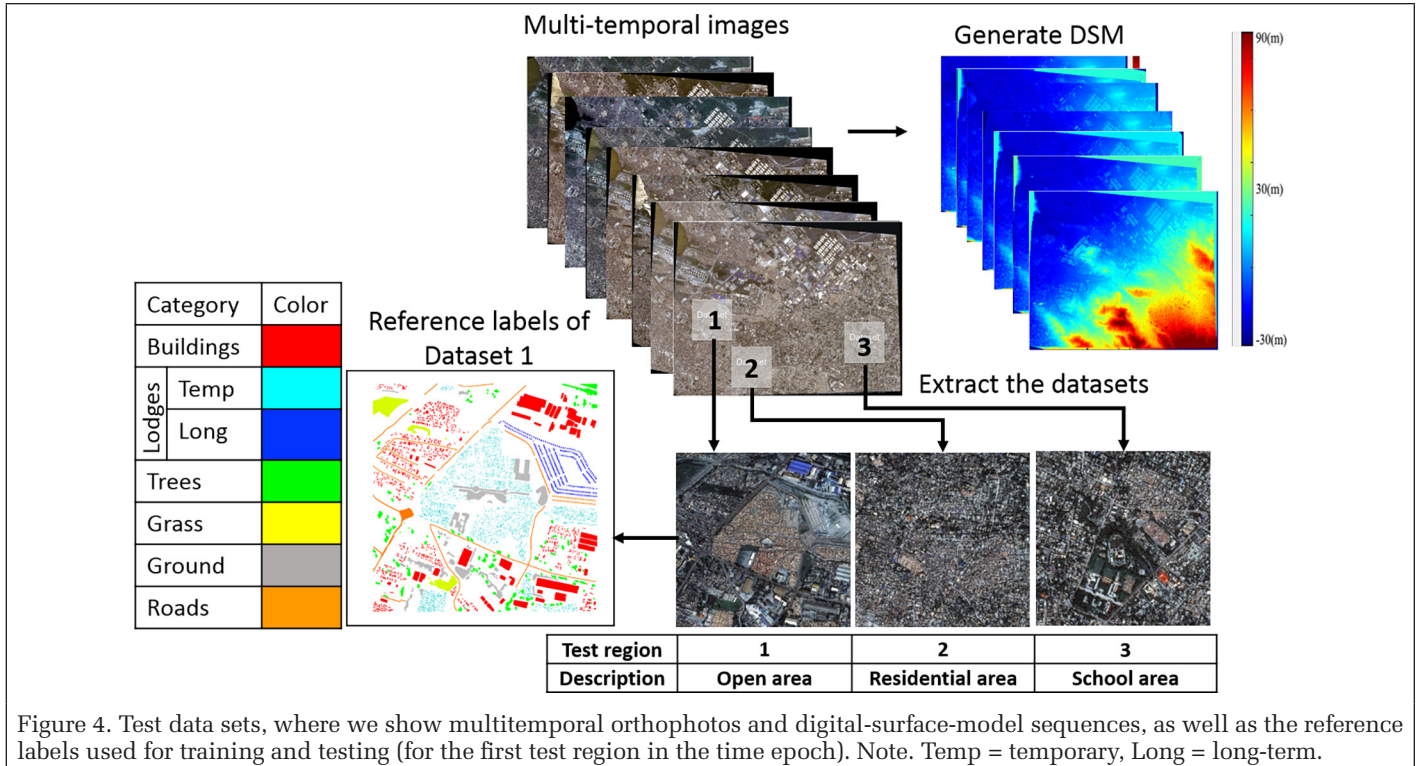


Figure 4. Test data sets, where we show multitemporal orthophotos and digital-surface-model sequences, as well as the reference labels used for training and testing (for the first test region in the time epoch). Note. Temp = temporary, Long = long-term.

region 1 indicates an open area surrounded by dense buildings, test region 2 is specifically dense residential areas with narrow streets, and test region 3 is a school zone with moderate and larger buildings among dense and small buildings. The selection of the three test regions is based on our visual inspection for representative regions across the data set, and apparent surface changes were observed in these regions as well, which will be quantified in detail in subsequent sections.

Data Preprocessing: DSM and Orthophoto Generation

In this preprocessing step, we generate the orthophoto and DSMs for the entire area of Port-au-Prince, Haiti, using the RPC Stereo Processor software and the stereo satellite imagery. The DSM generation is based on the semiglobal matching algorithm (Hirschmüller 2005). Then, the DSMs are geometrically aligned and nDSMs are generated, as described earlier. Figure 4 shows an overview of these data sets. During this step, all data sets with varying spatial resolutions are sampled to the highest cell size through the data sets (0.5 m).

Classification and Probability-Map Generation

The initial object-based classification is generated using the methods as described in previous sections. We keep the per-class probability map (already described) for further spatio-temporal inference. This initial classification yields a relatively satisfactory classification map to start with, with the overall accuracy shown in Table 3. In general, test region 2 (dense residential regions) yields the lowest overall accuracy (around 80%), primarily due to the complex rooftops and potentially higher uncertainties of the DSM.

Experimental Details of the Proposed 3D Iterative Spatiotemporal Filter

Parameters

As already described in section *The proposed 3D iterative spatiotemporal filter for probability inference*, the 3D iterative spatiotemporal filter has spatial, spectral, and temporal components (height difference through the temporal data set). Based on the described rationale of determining these bandwidth parameters, we apply the following parameters based on our data set.

Table 3. Overall initial classification accuracy for the three test regions.

Date	Accuracy (%)		
	Test region 1	Test region 2	Test region 3
3/Mar 2007	91.04	83.47	91.12
1/Jan 2010	93.21	81.50	93.06
6/Jun 2010	91.93	83.52	88.82
12/Dec 2010	89.08	80.81	88.58
3/Mar 2012	92.19	81.43	91.44
9/Sep 2013	90.40	81.03	94.99
7/Jul 2014	95.11	82.19	90.39
7/Jul 2015	92.74	83.22	94.61

Bandwidth for the spectral and spatial domains: Because of the size of each test image (over 2000×2000 pixels), the window size is set to 5×5 pixels to balance the efficiency and accuracy of the results. The bandwidth σ_s for each dimension of the spatial domain in the filter window is set to 3. In addition, for 8-bit images (ranging from 0 to 255) the bandwidth of the spectral domain σ_r is set empirically to 5, and this is shown in the original bilateral filter (Tomasi and Manduchi 1998) to have good leverage on smoothing and edge preserving.

Bandwidth for temporal (height) range domain σ_h : The elevation bandwidth is determined separately for each class as specified in Equation 6. Table 4 shows the bandwidth σ_h for each class, calculated using statistics in the test regions; this is to be done for each test region, as they have their own training labels. We can see that σ_h for buildings and trees is much higher than for the ground and grass classes. This is reasonable because the building and tree classes, in general, have larger height variations, and for the same amount of height difference the ground class should have smaller bandwidth to be sensitive to large changes, while the trees should have moderate tolerance to height differences when considering summing weighted probability maps.

Visual and Statistical Analysis of the Proposed Iterative Spatiotemporal Filter

Visual analysis: Our method enhances classification by utilizing the per-class probabilities of time-series data via

Table 4. Temporal (height) domain bandwidth σ_h for each class on test region 1.

Item	Height (m)
Buildings	5.98
Temporary lodging	0.64
Long-term lodging	1.50
Ground	0.53
Trees	4.45
Grass	0.56
Roads	1.08

spatiotemporal inference. This is reasonable, as unchanged objects can be used to mutually enhance the fidelity of the classification probability maps. We compare the initial and enhanced classification results for all the data sets in Figure 5. For instance, the mislabeled objects in the initial classification map of the dense areas in test regions 2 and 3 are corrected after being processed by the proposed spatiotemporal inference method. As shown in regions within the black circle, open grounds primarily dominated by temporary lodgings are misclassified to the ground or grass classes in the initial classification map, and the proposed spatiotemporal inference method shows that these misclassifications can be effectively corrected and demonstrates that classification maps are visually consistent with the images (quantifiable accuracy improvement shown under Statistical analysis).

To demonstrate how the iterative process improves the classification results, we select a small patch from the date of 2014/07 in test region 1 (Figure 6) to analyze their classification map in each iteration of the process. The patch shows two buildings with close adjacency, and its initial classification map (Figure 6b) shows the enlarged view where the buildings are partly misclassified to long-term lodgings. As can be seen from the figures, the iterative process gradually recovers the classification map where, in the 11th iteration (convergence), the final result (Figure 6g) shows a much more complete building segment.

Statistical analysis: Table 5 shows the classification accuracies of each image in each test region before and after their probability maps are processed by the proposed method, where “Before” refers to the overall accuracy of initial classification results, “After” indicates the enhanced accuracy through our proposed method, and “ Δ ” represents the accuracy change in the enhanced results over the initial ones. The average increase in the accuracy of the three test regions is 4.2363%, 5.285%, and 4.723%, respectively.

In Table 6 we took a small patch of pixels in test region 2 to show probability changes with the number of iterations. The first patch is a part of a building area, and the second patch shows trees. In both patches, we notice that the probability of the correct class increases with iterations (see the arrows) and those of the remaining classes decrease.

Figure 7 presents the overall accuracy for the entire set of iterations and three experiments. We can see in Figure 7 that the first iteration plays a major role in the accuracy enhancement. In all three experiments, the first iteration increased about 4%–6% of the overall accuracy and the rest of the iterations (until convergence) contribute approximately 1%–2%. On average, we note that all experiments converge around the fifth iteration.

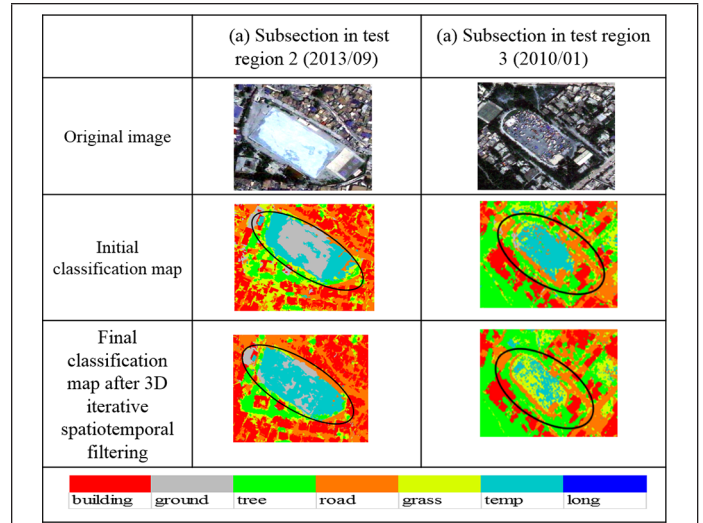


Figure 5. Two sample patches in test regions 2 and 3 illustrating the enhancement of classification after the proposed filter.

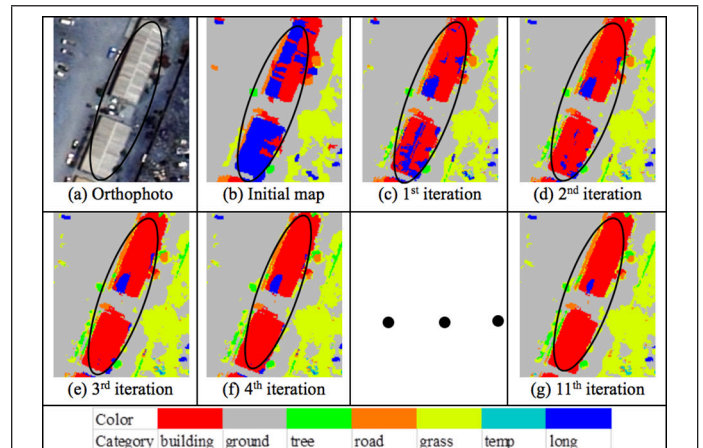


Figure 6. Detailed classification result for each iteration of enhancement for a patch in test region 1.

Table 5. The overall accuracy (%) before and after probability enhancement for each test region. (Note: the bold numbers indicate the maximum increase in the accuracy.)

Date	Test region 1			Test region 2			Test region 3		
	Before	After	Δ	Before	After	Δ	Before	After	Δ
2007	91.04	95.21	+4.17	83.47	88.14	+4.67	91.12	95.85	+4.73
1/Jan 2010	93.21	96.45	+3.24	81.50	85.67	+4.17	93.06	96.82	+3.76
6/Jun 2010	91.93	96.26	+4.33	83.52	89.79	+6.27	88.82	94.87	+6.05
12/Dec 2010	89.08	95.57	+6.49	80.81	87.59	+6.78	88.58	94.86	+6.28
3/Mar 2012	92.19	95.92	+3.73	81.43	86.92	+5.49	91.44	97.08	+5.64
9/Sep 2013	90.40	96.56	+6.16	81.03	87.29	+6.26	94.99	97.54	+2.55
7/Jul 2014	95.11	97.27	+2.16	82.19	88.90	+6.17	90.39	96.58	+6.19
2015	92.74	96.35	+3.61	83.22	85.69	+2.47	94.61	97.19	+2.58
Average	92.09	96.20	+4.24	82.15	87.50	+5.29	91.63	96.35	+4.72

Conclusion and Future Work

We have proposed a spatiotemporal inference method that improves the classification accuracy of multiview and multitemporal VHR satellite images. Knowing that temporal classification maps often suffer from inconsistencies in their results due to highly variable features that change over time, we propose using 3D geometric features (i.e., DSMs generated

Table 6. Mean probabilities (%) for each class changed through iterations using a sample patch of buildings and trees in test region 2.

Iteration	Class					
	Buildings	Grass	Ground	Road	Temp	Tree
Buildings						
1	73.16	1.68	17.69	11.53	0.92	0.24
2	74.95↑	1.85	16.36	10.65	1.09	0.25
3	75.45↑	1.96	15.87	10.28	1.19	0.25
4	75.53↑	2.05	15.70	10.11	1.25	0.26
5	75.53	2.14	15.70	10.11	1.30	0.27
6	75.53	2.14	15.70	10.11	1.35	0.27
7	75.53	2.14	15.70	10.11	1.35	0.28
Trees						
1	0.12	24.66	0.23	0.01	0.01	80.69
2	0.10	23.76	0.22	0.01	0.01	82.97↑
3	0.09	23.18	0.22	0.01	0.01	84.03↑
4	0.08	22.75	0.22	0.01	0.01	84.58↑
5	0.08	22.41	0.22	0.01	0.01	84.86↑
6	0.08	22.41	0.22	0.01	0.01	84.95↑
7	0.08	22.41	0.22	0.01	0.01	84.91

from multiview images) for better stability. We applied our proposed spatiotemporal inference method to process VHR imagery and DSMs to enhance the classification accuracy of each individual temporal data set. Our proposed method approximates the global inference model through iterative processing of 3D bilateral filters utilizing the spatial, spectral, and geometric information. Our method achieved a 2% to 6% increase in overall accuracy for all experiments with varying scene complexities. Notable improvements were observed in certain scenarios. For example, for the open (sparse) areas in the first and third data sets, the accuracy increased from $\approx 89\%$ to $\approx 97\%$, whereas for dense regions in test region 2, the accuracy increased from $\approx 80\%$ to $\approx 90\%$. Since the proposed method is a postprocessing method operating on probability maps, it is able to work on probability maps generated by different types of classifiers as long as the probability maps can be derived. In addition, the proposed method can be further generalized to less-restrictive data sets by considering the temporal component to be the image themselves. For instance, it can be applied on moderate- and low-resolution satellite imagery and can be used to process video sequences or different types of time-series raster data to enhance the image data qualities.

Acknowledgments

This work is supported by the Sustainable Institute at The Ohio State University. The authors would like to thank the anonymous reviewers for their comments and suggestions that led to the final version of the manuscript.

References

Albanwan, H. and R. Qin. 2018. A novel spectrum enhancement technique for multi-temporal, multi-spectral data using spatial-temporal filtering. *ISPRS Journal of Photogrammetry and Remote Sensing* 142:51–63.

Chaabouni-Chouayakh, H., T. Krauss, P. d'Angelo and P. Reinartz. 2010. 3D change detection inside urban areas using different digital surface models. *The International Archives of the Photogrammetry, Remote Sensing and Spatial Information Sciences* 38 (3B):86–91.

Chen, G., G. J. Hay, L.M.T. Carvalho and M. A. Wulder. 2012. Object-based change detection. *International Journal of Remote Sensing* 33 (14):4434–4457.

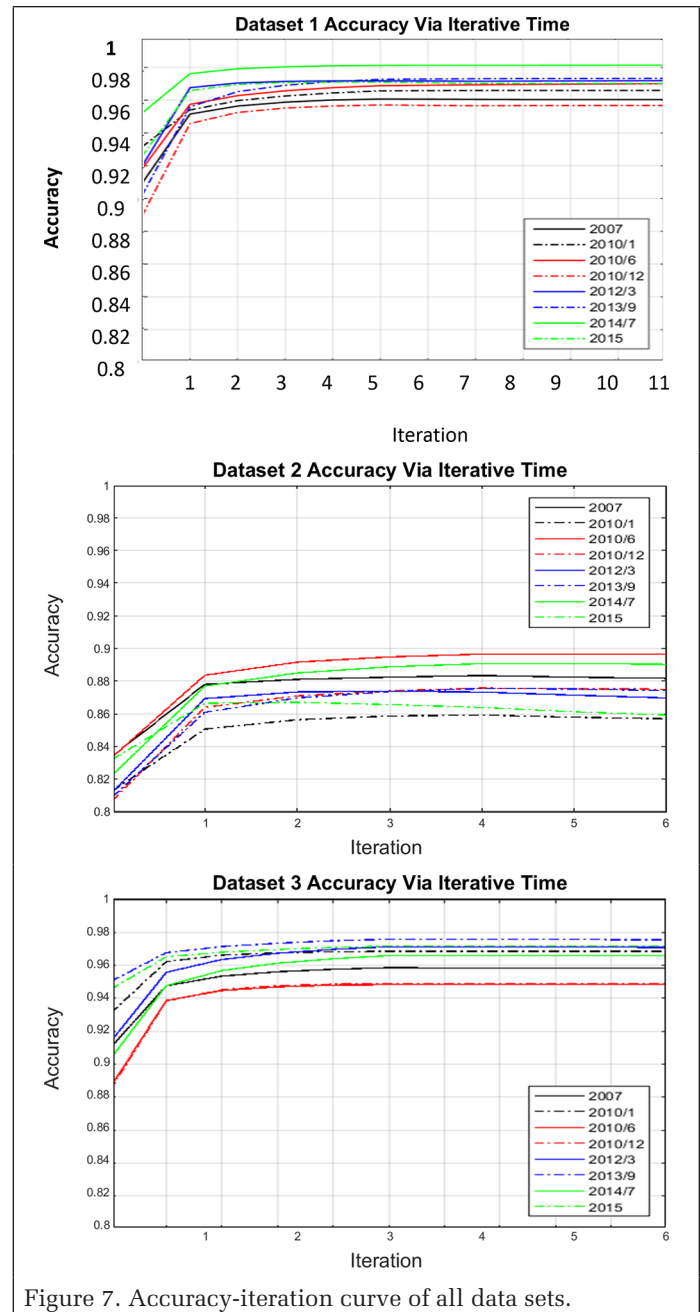


Figure 7. Accuracy-iteration curve of all data sets.

Cheng, Q., H. Liu, H. Shen, P. Wu and L. Zhang. 2017. Spatial and temporal nonlocal filter-based data fusion method. *IEEE Transactions on Geoscience and Remote Sensing* 55:4476–4488.

Fauvel, M., Y. Tarabalka, J. A. Benediktsson, J. Chanussot and J. C. Tilton. (2013). Advances in spectral-spatial classification of hyperspectral images. *Proceedings of the IEEE* 101 (3):652–675.

Floberg, J. M. and J. E. Holden. 2013. Nonlinear spatio-temporal filtering of dynamic PET data using a four-dimensional Gaussian filter and expectation-maximization deconvolution. *Physics in Medicine and Biology* 58 (4):1151–1168.

Fu, T.-C. 2011. A review on time series data mining. *Engineering Applications of Artificial Intelligence* 24 (1):164–181.

Ghamisi, P., M. Dalla Mura and J. A. Benediktsson. 2015. A survey on spectral-spatial classification techniques based on attribute profiles. *IEEE Transactions on Geoscience and Remote Sensing* 53 (5):2335–2353.

Gruen, A. and D. Akca. 2005. Least squares 3D surface and curve matching. *ISPRS Journal of Photogrammetry and Remote Sensing* 59 (3):151–174.

- Gu, W., Z. Lv and M. Hao. 2017. Change detection method for remote sensing images based on an improved Markov random field. *Multimedia Tools and Applications* 76 (17):17719–17734.
- Hirschmüller, H. 2005. Accurate and efficient stereo processing by semi-global matching and mutual information. Pages 807–814 in *Proceedings, 2005 IEEE Computer Society Conference on Computer Vision and Pattern Recognition*, Vol. 2, held in San Diego, California, 20–25 June 2005. Edited by C. Schmid, S. Soatto and C. Tomasi. Los Alamitos, California: IEEE Computer Society.
- Huang, X., L. Zhang and W. Gong. 2011. Information fusion of aerial images and LIDAR data in urban areas: Vector-stacking, re-classification and post-processing approaches. *International Journal of Remote Sensing* 32 (1):69–84.
- Joblove, G. H. and D. Greenberg. 1978. Color spaces for computer graphics. *ACM SIGGRAPH Computer Graphics* 12 (3):20–25.
- Jolliffe, I. 2005. Principal component analysis. In *Encyclopedia of Statistics in Behavioral Science*, Wiley Online Library.
- Kasetkasem, T. and P. K. Varshney. 2002. An image change detection algorithm based on Markov random field models. *IEEE Transactions on Geoscience and Remote Sensing* 40 (8):1815–1823.
- Keypour, R. N., T. Oommen, T. R. Martha, K. S. Sajinkumar and J. S. Gierke. 2018. A comparative analysis of pixel- and object-based detection of landslides from very high-resolution images. *International Journal of Applied Earth Observation and Geoinformation* 64:1–11.
- Kim, Y. 2016. Generation of land cover maps through the fusion of aerial images and airborne LiDAR data in urban areas. *Remote Sensing* 8 (6):521.
- Kotthaus, S., T.E.L. Smith, M. J. Wooster and C.S.B. Grimmond. 2014. Derivation of an urban materials spectral library through emittance and reflectance spectroscopy. *ISPRS Journal of Photogrammetry and Remote Sensing* 94:194–212.
- Krähenbühl, P. and V. Koltun. 2011. Efficient inference in fully connected CRFs with Gaussian edge potentials. Pages 109–117 in *Proceedings of the 24th International Conference on Neural Information Processing Systems*, held in Granada, Spain, 12–15 December 2011. Edited by J. Shawe-Taylor, R. S. Zemel, P. L. Bartlett, F. Pereira and K. Q. Weinberger.
- Liu, D. and S. Cai. 2012. A spatial-temporal modeling approach to reconstructing land-cover change trajectories from multi-temporal satellite imagery. *Annals of the Association of American Geographers* 102 (6):1329–1347.
- Lu, D., S. Hetrick and E. Moran. 2010. Land cover classification in a complex urban-rural landscape with QuickBird imagery. *Photogrammetric Engineering and Remote Sensing* 76 (10):1159–1168.
- MacFaden, S. W., J.P.M. O’Neil-Dunne, A. R. Royar, J.W.T. Lu and A. G. Rundle. 2012. High-resolution tree canopy mapping for New York City using LIDAR and object-based image analysis. *Journal of Applied Remote Sensing* 6 (1):63567.
- Minh, N. Q. and L. P. Hien. 2011. Land cover classification using LiDAR intensity data and neural network. *Journal of the Korean Society of Surveying, Geodesy, Photogrammetry and Cartography* 29 (4):429–438.
- Moser, G., S. B. Serpico and J. A. Benediktsson. 2013. Land-cover mapping by Markov modeling of spatial-contextual information in very-high-resolution remote sensing images. *Proceedings of the IEEE* 101 (3):631–651.
- Qin, R. 2015. A mean shift vector-based shape feature for classification of high spatial resolution remotely sensed imagery. *IEEE Journal of Selected Topics in Applied Earth Observations and Remote Sensing* 8 (5):1974–1985.
- Qin, R. 2016. RPC Stereo Processor (RSP)—A software package for digital surface model and orthophoto generation from satellite stereo imagery. *ISPRS Annals of the Photogrammetry, Remote Sensing and Spatial Information Sciences* III-1:77–82.
- Qin, R. and W. Fang. 2014. A hierarchical building detection method for very high resolution remotely sensed images combined with DSM using graph cut optimization. *Photogrammetric Engineering and Remote Sensing* 80 (9):873–883.
- Qin, R., X. Huang, A. Gruen and G. Schmitt. 2015. Object-based 3-D building change detection on multitemporal stereo images. *IEEE Journal of Selected Topics in Applied Earth Observations and Remote Sensing* 8 (5):2125–2137.
- Qin, R., J. Tian and P. Reinartz. 2016. Spatiotemporal inferences for use in building detection using series of very-high-resolution space-borne stereo images. *International Journal of Remote Sensing* 37 (15):3455–3476.
- Salehi, B., Y. Zhang and M. Zhong, M. 2011. Object-based land cover classification of urban areas using VHR imagery and photogrammetrically-derived DSM. Pages 461–467 in *American Society for Photogrammetry and Remote Sensing Annual Conference 2011*, held in Milwaukee, Wisconsin, 1–5 May 2011. Edited by J. Editor. Bethesda, Maryland: American Society for Photogrammetry and Remote Sensing.
- Tomasi, C. and R. Manduchi. 1998. Bilateral filtering for gray and color images. Pages 839–846 in *Sixth International Conference on Computer Vision*, held in Bombay, India, 4–7 January 1998. Edited by J. Editor. New Delhi, India: Narosa Publishing House.
- Waser, L. T., E. Baltsavias, K. Ecker, H. Eisenbeiss, E. Feldmeyer-Christe, C. Ginzler, M. Küchler and L. Zhang. 2008. Assessing changes of forest area and shrub encroachment in a mire ecosystem using digital surface models and CIR aerial images. *Remote Sensing of Environment* 112 (5):1956–1968.
- Weih Jr, R. C. and Riggan Jr, N. D. 2010. Object-based classification vs. pixel-based classification: Comparative importance of multi-resolution imagery. *The International Archives of the Photogrammetry, Remote Sensing and Spatial Information Sciences* XXXVIII-4/C7:PPP–PPP.
- Yan, W. Y., A. Shaker and N. El-Ashmawy. 2015. Urban land cover classification using airborne LiDAR data: A review. *Remote Sensing of Environment* 158:295–310.
- Zhang, J. 2010. Multi-source remote sensing data fusion: Status and trends. *International Journal of Image and Data Fusion* 1 (1):5–24.
- Zhang, Q. [Qian], R. Qin, X. Huang, Y. Fang and L. Liu. 2015. Classification of ultra-high resolution orthophotos combined with DSM using a dual morphological top hat profile. *Remote Sensing* 7 (12):16422–16440.
- Zhang, Q. [Qing]. 2006. An empirical evaluation of the random forests classifier models for variable selection in a large-scale lung cancer case-control study (Doctoral dissertation). Retrieved from ProQuest Dissertations and Theses database. (3259518)

Advertise in the #1 publication in the imaging and geospatial information industry!



Impact Factor (2018): 3.15

PE&RS (Photogrammetric Engineering & Remote Sensing) is the official journal of the American Society for Photogrammetry and Remote Sensing—the Imaging and Geospatial Information Society (ASPRS). This highly respected publication is the #1 publication in the industry by a wide margin. Advertisers with a desire to reach this market can do no better than PE&RS. It delivers the right audience of professionals who are loyal and engaged readers, and who have the purchasing power to do business with you.

PE&RS Readership Highlights

Circulation: 3,000
Total audience: 6,400*

Founded in 1934, the American Society for Photogrammetry and Remote Sensing (ASPRS) is a scientific association serving professional members throughout the world. Our mission is to advance knowledge and improve understanding of mapping sciences to promote the responsible applications of photogrammetry, remote sensing, geographic information systems (GIS), and supporting technologies.

Our members are analysts/specialists, educators, engineers, managers/administrators, manufacturers/ product developers, operators, technicians, trainees, marketers, and scientists/researchers. Employed in the disciplines of the mapping sciences, they work in the fields of Agriculture/Soils, Archeology, Biology, Cartography, Ecology, Environment, Forestry/Range, Geodesy, Geography, Geology, Hydrology/Water Resources, Land Appraisal/ Real Estate, Medicine, Transportation, and Urban Planning/Development.

RESERVE YOUR SPACE TODAY!

Bill Spilman, ASPRS Advertising, Exhibit Sales & Sponsorships
 (877) 878-3260 toll-free
 (309) 483-6467 direct
 (309) 483-2371 fax
 bill@innovativemediasolutions.com

Corporate Member Exhibiting at a 2019 ASPRS Conference	Corporate Member	Exhibitor	Non Member
---	------------------	-----------	------------

All rates below are for four-color advertisements

Cover 1	\$1,850	\$2,000	\$2,350	\$2,500
<i>In addition to the cover image, the cover sponsor receives a half-page area to include a description of the cover (maximum 500 words). The cover sponsor also has the opportunity to write a highlight article for the journal. Highlight articles are scientific articles designed to appeal to a broad audience and are subject to editorial review before publishing. The cover sponsor fee includes 50 copies of the journal for distribution to their clients. More copies can be ordered at cost.</i>				
Cover 2	\$1,500	\$1,850	\$2,000	\$2,350
Cover 3	\$1,500	\$1,850	\$2,000	\$2,350
Cover 4	\$1,850	\$2,000	\$2,350	\$2,500
Advertorial	1 Complimentary Per Year	1 Complimentary Per Year	\$2,150	\$2,500
Full Page	\$1,000	\$1,175	\$2,000	\$2,350
2 page spread	\$1,500	\$1,800	\$3,200	\$3,600
2/3 Page	\$1,100	\$1,160	\$1,450	\$1,450
1/2 Page	\$900	\$960	\$1,200	\$1,200
1/3 Page	\$800	\$800	\$1,000	\$1,000
1/4 Page	\$600	\$600	\$750	\$750
1/6 Page	\$400	\$400	\$500	\$500
1/8 Page	\$200	\$200	\$250	\$250
Other Advertising Opportunities				
Wednesday Member Newsletter Email Blast	1 Complimentary Per Year	1 Complimentary Per Year	\$600	\$600

A 15% commission is allowed to recognized advertising agencies

THE MORE YOU ADVERTISE THE MORE YOU SAVE! PE&RS offers frequency discounts. Invest in a three-times per year advertising package and receive a 5% discount, six-times per year and receive a 10% discount, 12-times per year and receive a 15% discount off the cost of the package.

*Based on 2 readers per copy as well as online views | Source: PE&RS Readership Survey, Fall 2012

Robust Pose Estimation and Calibration of Catadioptric Cameras With Spherical Mirrors

Sagi Filin, Grigory Ilizirov, and Bashar Elnashef

Abstract

Catadioptric cameras broaden the field of view and reveal otherwise occluded object parts. They differ geometrically from central-perspective cameras because of light reflection from the mirror surface. To handle these effects, we present new pose-estimation and reconstruction models for imaging through spherical mirrors. We derive a closed-form equivalent to the collinearity principle via which three methods are established to estimate the system parameters: a resection-based one, a trilateration-based one that introduces novel constraints that enhance accuracy, and a direct and linear transform-based one. The estimated system parameters exhibit improved accuracy compared to the state of the art, and analysis shows intrinsic robustness to the presence of a high fraction of outliers. We then show that 3D point reconstruction can be performed at accurate levels. Thus, we provide an in-depth look into the geometrical modeling of spherical catadioptric systems and practical enhancements of accuracies and requirements to reach them.

Introduction

In land cover/land use change mapping, obtaining consistent data and classification results is critical for remote sensing applications and time-series analysis. Varying acquisition conditions—such as meteorological conditions, viewing angles, sun illumination, and sensor characteristics—largely affect the radiometric consistency through different temporal data sets. State-of-the-art satellite imaging platforms, including the Ikonos (1999, decommissioned), GeoEye-1 (2008), and WorldView satellite constellations, are able to collect very-high-resolution (VHR) multispectral images, with a spatial resolution that reaches as high

Affordable digital cameras are making photogrammetric practices relevant for a wide variety of applications. Beneficial as they are, they are hindered by the limited field of view that necessitates acquisition of a large number of images.

In this context, incorporation of mirrors into the imaging systems (aka catadioptric cameras) can expand the field of view and facilitate mapping of otherwise unseen or occluded objects or object parts. As a consequence, such systems find use in a variety of applications including object tracking (Barreto, Martin and Horaud 2003; Cinaroglu and Bastanlar 2016), navigation and path following (Khurana and Armenakis 2018; Marie *et al.* 2019), depth recovery (Barone *et al.* 2018a), and human detection (Cinaroglu and Bastanlar 2014).

While broadening the field of view and revealing otherwise occluded scene parts, imaging by such systems is governed by light reflection from the mirror surface. The collinearity relation no longer holds, and imaged entities are acquired with severe nonlinear distortions. The challenge is to establish the relation of object space to image space in a manner that leads to estimation of the camera pose parameters and to the performance of mapping. Our focus in this article is on an imaging

system which incorporates a camera and a spherical mirror, an inexpensive apparatus which is simple to manufacture (Ohte *et al.* 2005). Its symmetric form also makes it advantageous from a modeling perspective. In reference to its actual system modeling, Ohte *et al.* (2005) model the reflection and projection of an object-point through such a system. The focus lies on the image formation rather than on pose estimation. Mi^{ccaron}usik and Pajdla (2004) propose an approximation to the central-perspective model with a single calibration parameter. However, the approximation error does not allow estimation of the mapping error as a function of the image noise. Lanman *et al.* (2006) describe a system composed of an array of spherical mirrors which provides multiple views from a single image. A bundle adjustment-like solution is proposed, but accuracy matters are not discussed. Agrawal (2013) uses a coplanarity constraint between an object-point and the sphere and camera centers, estimating the latter two using eight points or more. In this model the sphere boundary may not be seen. Geometrical properties within the plane are not considered. Xiang, Dai, and Gong (2013) address the calibration of a spherical imaging system and extend the generalized unified model (Geyer and Daniilidis 2000) to account for a misalignment between the camera optical axis and the axis connecting the perspective center and the spherical-mirror center. The authors propose adding compensating parameters that account for the offset of the projection center and rotation of the image plane. In a follow up work, Xiang, Zhou, and Gong (2015) consider a setting consisting of a single camera and an array of spherical mirrors. They estimate both the intrinsic camera parameters and the relative pose of a set of virtual cameras (one for each sphere) with no prior knowledge on the system parameters. Jaramillo, Valenti, and Xiao (2016) extend the generalized unified model for a stereo-catadioptric system. Here again, they focus on misalignment as in Xiang *et al.* (2013). A virtual system for each camera is defined that is connected by a joint coordinate reference frame. The relative orientation between the two systems is estimated in the form of a bundle adjustment. Finally, Barone *et al.* (2018a, 2018b) present a spherical-mirror-based stereo-view configuration that also includes a pattern projector as a means to perform 3D modeling and object reconstruction. The stereo-pair parameters are solved independently, and a four-degree polynomial is solved for the catadioptric system parameters, yielding four solutions from which two are feasible and one is optimal.

In this article we study pose estimation and reconstruction models for spherical-mirror-based catadioptric systems. We first develop new expressions that relate object- and image-space coordinates and then model the imaging system as a whole. Our derivations yield three alternative estimation models—the first offers a closed-form equivalence to

Sagi Filin, Grigory Ilizirov, and Bashar Elnashef are with Mapping and Geo-Information Engineering, Technion City, Haifa 32000, Israel (filin@technion.ac.il).

Photogrammetric Engineering & Remote Sensing
Vol. 86, No. 1, January 2020, pp. 33–44.
0099-1112/20/33–44

© 2020 American Society for Photogrammetry
and Remote Sensing
doi: 10.14358/PERS.86.1.33

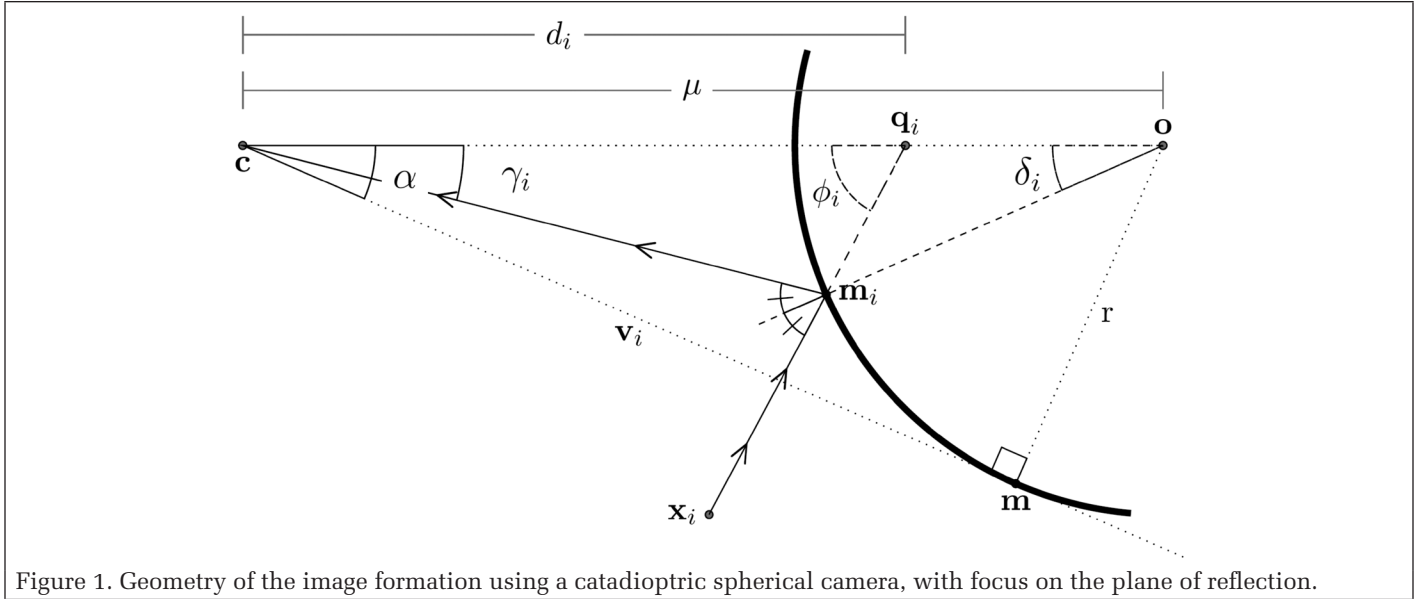


Figure 1. Geometry of the image formation using a catadioptric spherical camera, with focus on the plane of reflection.

the collinearity principle, the second proposes a geometric constraint that improves the accuracy and robustness of the estimated parameters, and the third provides an equivalent to a direct linear transform (DLT). The proposed models show improved accuracy of the system parameters compared to the state of the art. The requirements for estimating the system parameters are minimal, and only three control points are needed for the first two models, while the third requires only six, similar to the DLT. Performance analysis shows robustness to a high fraction of outliers and needs no application of the random-sample consensus algorithm. We then extend the model into a calibration mode and study 3D reconstruction using a stereo configuration and the derived accuracy. In sum, it not only offers a thorough study on the system geometry and its implications on modeling and accuracy but also provides a viable framework for pose estimation and modeling. Notably, the ability to model scene parts from outside the camera's direct field of view offers an appealing means for 3D reconstruction.

Geometrical Quantities Within Spherical Catadioptric Systems

Images acquired by catadioptric cameras are formed by reflection of light from the mirror surface and onto the image plane. By the law of reflection we have that the incident ray $\overline{x_i m_i}$, the reflected ray $\overline{m_i c}$, and the normal to the mirror surface are coplanar and that the angles between the incident and emitted rays and the normal to the surface are equal (Figure 1). As the radius is the normal to the sphere surface, its center \mathbf{o} also lies within that plane. The system is classified as *axial* (Ramalingam, Sturm and Lodha 2006), as all the extended rays (as if they were not reflected) intersect along an axis.¹ This axis is the vector $\overline{\mathbf{o}c}$, which links the perspective and camera centers; μ is the distance between these two points (Figure 1).

The system parameters consist of the projection center \mathbf{c} , the spherical-mirror center \mathbf{o} , and the radius r , a parameter that is often ignored. The objective is to estimate the parameters using a set of reference-points \mathbf{x}_i , which are projected onto the image plane from the sphere surface.

Geometric Quantities of Planes of Reflection

In order to express the relation between the control points, their projection onto the image plane, and the direction of the

extended ray, we first derive expressions for four elements within the *plane of reflection*: the angle γ_i between $\overline{\mathbf{o}c}$ and $\overline{\mathbf{m}_i c}$; the distance d_i between \mathbf{c} and \mathbf{q}_i , the intersection of the extended ray $\overline{x_i m_i}$ and $\overline{\mathbf{o}c}$; the angle δ_i between $\overline{\mathbf{o}c}$ and $\overline{\mathbf{o}m_i}$; and the angle ϕ_i between $\overline{x_i q_i}$ and $\overline{\mathbf{o}c}$ (Figure 1). To keep the model applicable to any type of central camera (e.g., one equipped with a fish-eye lens), we use angular quantities which are measurable in the image reference frame. Therefore, the inner orientation has no effect on the computation, while the radial lens distortions do. In the case that neither the principal distance nor the distortion parameters are given, the camera should be calibrated in advance using any standard method.

Computing γ_i requires defining the image-space direction of $\overline{\mathbf{o}c}$. This direction must be estimated, as the mirror's center \mathbf{o} does not show on the image. We first make a reference to methods that are based on either placement of actual markers on the lens or projection of the sphere's boundary onto the image following the camera orientation (Kanbara *et al.* 2006; Francken, Hermans and Bekaert 2007). However, we propose an alternative method that requires neither, and is valid for any central camera as long as part of the sphere boundary is imaged.

We begin by observing that the projection of the mirror boundary on the image relates to the tangent ray to the sphere's surface, $\overline{\mathbf{m}_i c}$ (Figure 1), and that the angle α between these two vectors is the same for any point on the boundary (Taguchi *et al.* 2010). Thus,

$$\mathbf{v}_i^T \overline{\mathbf{o}c} = \|\mathbf{v}_i\| \|\overline{\mathbf{o}c}\| \cos(\alpha), \quad (1)$$

with \mathbf{v}_i the image-space direction toward the sphere boundary. As our interest is only in the direction of $\overline{\mathbf{o}c}$, we set

$$\|\overline{\mathbf{o}c}\| = \cos(\alpha)^{-1} \quad (2)$$

and so can write:

$$\mathbf{v}_i^T \overline{\mathbf{o}c} = \|\mathbf{v}_i\|, \quad (3)$$

which can then be extended to multiple observations allowing us to estimate $\overline{\mathbf{o}c}$ linearly and thereby compute the angle α by Equation (2). Here \mathbf{v}_i is the measured parameters, and the system axis $\overline{\mathbf{o}c}$ is the unknown. The angle γ_i can then be computed by the scalar product between $\overline{\mathbf{o}c}$ and $\overline{\mathbf{c}m_i}$. As the radius is perpendicular to the tangent ray (Figure 1), we also have

1. For standard pinhole cameras, all rays intersect at a single point, and accordingly the camera is classified as *central*.

$$\sin(\alpha) = \frac{r}{\mu}. \quad (4)$$

$$\sin\left(\frac{\xi_{ij}}{2}\right) = \frac{m_{ij}}{2r} \quad (9)$$

Hence, if r is known, μ can be derived.

To express d_i , our second element of interest within the plane of reflection, we use the law of sines for $\Delta(\mathbf{c}, \mathbf{q}_i, \mathbf{m}_i)$ and $\Delta(\mathbf{c}, \mathbf{m}_i, \mathbf{o})$ to obtain (Figure 2)

$$d_i = \frac{\sin(\pi - (\gamma_i + \phi_i))}{\sin(\phi_i)} \cdot m_i, \quad (5)$$

where

$$m_i = \frac{\sin(\delta_i)}{\sin(\gamma_i)} \cdot r. \quad (6)$$

To express the third quantity, δ_i , which also appears in Equation 6, we use again the law of sines for $\Delta(\mathbf{c}, \mathbf{m}_i, \mathbf{o})$ to obtain

$$\delta_i = \sin^{-1}\left(\frac{\mu}{r} \sin(\gamma_i)\right) - \gamma_i \quad (7)$$

for $0 < \gamma_i < \alpha$. Finally, the fourth quantity, ϕ_i , can be derived by observing that $\phi_i = 2\gamma_i + \delta_i$ (Figure 2). The four geometric quantities allow computation, for any plane of reflection, of the projection of a point onto image space and the direction of the extended ray $\overline{\mathbf{x}, \mathbf{m}_i}$.

Relation Between Planes of Reflection

Two planes of reflection are related by a rotation ψ_{ij} about the camera axis $\overline{\mathbf{o}, \mathbf{c}}$ (Figure 3). To compute ψ_{ij} , we first compute the distances m_i and m_j using Equation 6 and then compute m_{ij} (Figure 3) by the law of cosines for $\Delta(\mathbf{c}, \mathbf{m}_i, \mathbf{m}_j)$:

$$m_{ij}^2 = m_i^2 + m_j^2 - 2m_i m_j \cos(\beta_{ij}), \quad (8)$$

where β_{ij} is the outcome of the scalar product of $\overline{\mathbf{m}_i, \mathbf{c}}$ and $\overline{\mathbf{m}_j, \mathbf{c}}$. As \mathbf{m}_i and \mathbf{m}_j lie on the sphere, the spherical angle ξ_{ij} (Figure 3) can be computed by

and according to the spherical law of cosines (Figure 3c),

$$\cos(\psi_{ij}) = \frac{\cos(\xi_{ij}) - \cos(\delta_j) \cos(\delta_i)}{\sin(\delta_j) \sin(\delta_i)}, \quad (10)$$

yielding the angle ψ_{ij} between the two planes of reflection.

Parameter Estimation

The establishment of the geometrical relations within and between the planes of reflection allows us to estimate the system parameters, including the camera and mirror positions and the radius. Three alternatives are derived, beginning with an equivalent to the collinearity relation and ending in a direct linear model.

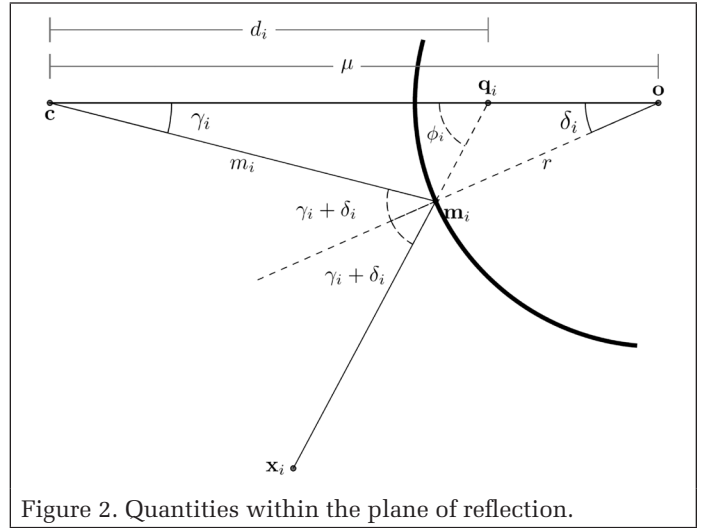


Figure 2. Quantities within the plane of reflection.

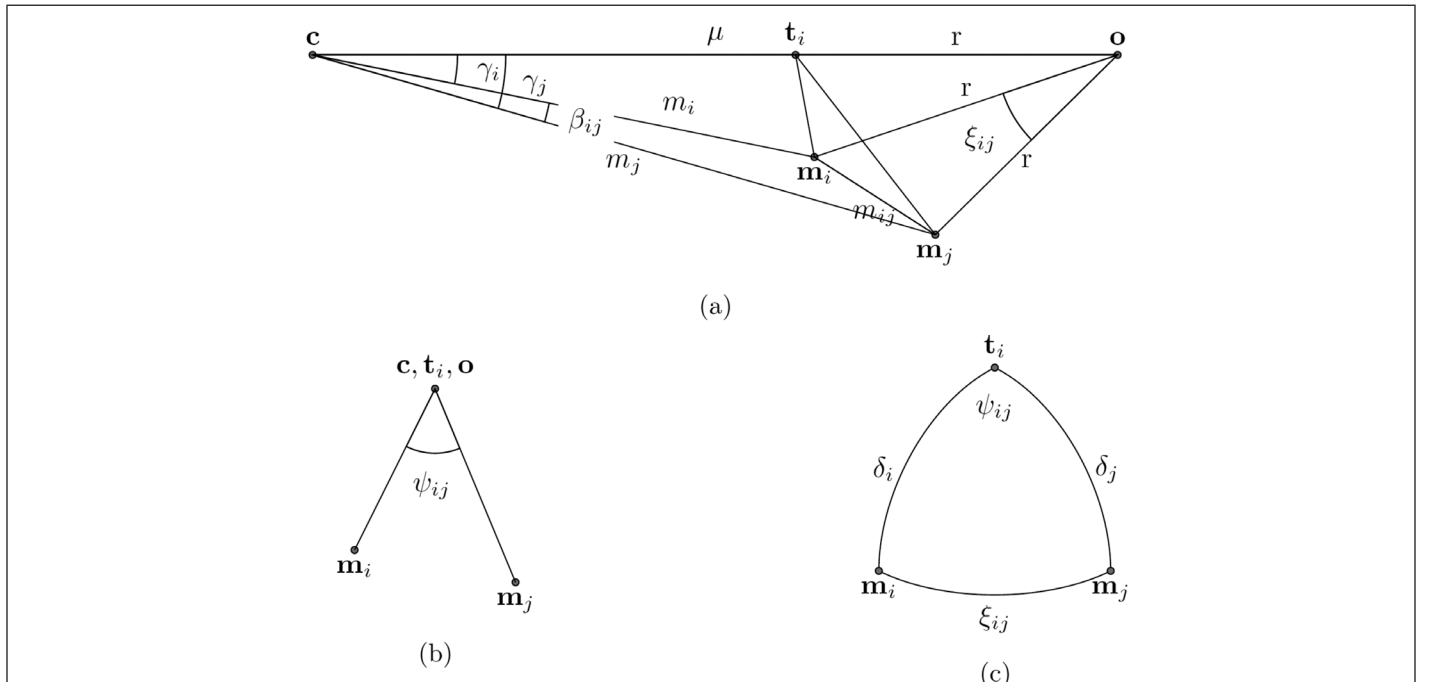


Figure 3. Geometry of two reflection planes: (a) Quantities between two planes of reflection, (b) definition of the angle ψ_{ij} between planes of reflection, (c) the spherical triangle formed by two incidence points and the intersection of camera axis and the sphere.

Transformation Between Planes of Reflection and Object-Space and Collinearity Equivalence

We derive first the transformation between the plane of reflection and object-space. To establish this relation we introduce an intermediate coordinate system M , whose center lies at \mathbf{c} , x-axis is $\overline{\mathbf{oc}}$, y-axis is orthogonal to the x-axis on an arbitrary plane of reflection (e.g., on that containing \mathbf{x}_1), and z-axis completes a right-hand-side reference frame. A control point in M is expressed by its position along $\overline{\mathbf{q}_i\mathbf{x}_i}$ (Figure 2), namely:

$$[\mathbf{x}_i]_M = u[\mathbf{p}_i]_M + [\mathbf{q}_i]_M, \quad (11)$$

where $[\]_M$ is a vector in the M system and u is a scale factor. The vector $[\mathbf{q}_i]_M = (d_i, 0, 0)$, and $[\mathbf{p}_i]_M$ is the direction of $\overline{\mathbf{q}_i\mathbf{x}_i}$, for which we use the conical parametrization

$$[\mathbf{p}_i]_M = u_i (1, w_i \cdot \cos(v_i), w_i \cdot \sin(v_i))^T, \quad (12)$$

where v_i represents the rotation around $\overline{\mathbf{oc}}$ and is derived from ψ_{ij} , and $w_i = \tan(\phi_i) = \tan(\gamma_i + 2\gamma_i)$ is the slope of the line (Figure 2).

The transformation from M to object-space is of Euclidean nature.² Therefore,

$$[\mathbf{x}]_M = \mathbf{R}^T (\mathbf{x} - \mathbf{c}), \quad (13)$$

where \mathbf{c} is the camera perspective center and $\mathbf{R} = [\mathbf{r}_1 \ \mathbf{r}_2 \ \mathbf{r}_3]$ is the rotation matrix whose \mathbf{r}_1 column is the normalized $\overline{\mathbf{oc}}$ direction, \mathbf{r}_2 is the orthogonal direction to \mathbf{r}_1 in reference to the set control point when defining the axes (e.g., \mathbf{x}_1), and \mathbf{r}_3 completes a right-hand-side frame. We use Equations 11 and 13 to write

$$\mathbf{R}^T (\mathbf{x}_i - \mathbf{c}) - [\mathbf{q}_i]_M = u_i [\mathbf{p}_i]_M, \quad (14)$$

which provides an equivalent to the *collinearity relation*, where an object-space point \mathbf{x}_i is linked to derivable image-space quantities (here, ϕ_i , d_i , and v_i). Similar to central-perspective cameras, collineation is of the control-point-to-projection-center vector in both image- and object-space. Estimation of the rotation angles in \mathbf{R} and the camera position \mathbf{c} is directly obtained using a nonlinear least-squares adjustment. To derive the mirror's center \mathbf{o} we use

$$\mathbf{o} = \mathbf{c} + \mu \mathbf{r}_1 = \mathbf{c} + r \left(\frac{\mu}{r} \right) \mathbf{r}_1 = \mathbf{c} + \left(\frac{r}{\sin(\alpha)} \right) \mathbf{r}_1. \quad (15)$$

Trilateration-Based Estimation

Equations 14 and 15 allow us to estimate the system parameters, yet we derive it further into another approach that yields more accurate estimates and exhibits robustness to the existence of outliers. To do so, we first estimate the object-space parameters of $\overline{\mathbf{oc}}$ and only then determine both \mathbf{o} and \mathbf{c} positions along it. The estimation is performed in two separate steps: First, the direction of $\overline{\mathbf{oc}}$ is derived and its position estimated; then the model parameters are recovered (Algorithm 1 summarizes our scheme).

We note that $\overline{\mathbf{oc}}$'s direction in object-space coincides with \mathbf{r}_1 in Equation 13. For its estimation we construct a triangular

prism-like structure using a pair of control points, \mathbf{x}_i and \mathbf{x}_j , where the prism bases are orthogonal to $\overline{\mathbf{oc}}$ and pass through both points (Figure 12d). We derive in the Appendix the geometric relations between the distances $\|\overline{\mathbf{q}_i\mathbf{x}_i}\|$, r_1 , and the measurable image-space quantities, and show that they yield two constraints:

$$\mathbf{r}_1^T (\mathbf{x}_i - \mathbf{x}_j) + b_0 + b_1 l_j + b_2 l_i = 0 \quad (16)$$

$$-l_i^2 - l_j^2 + a_0 l_i l_j + a_1 l_i + a_2 l_j + a_3 = 0, \quad (17)$$

Algorithm 1. The trilateration-based parameter estimation scheme.

Input: image- and object-space correspondences

Output: mirror and camera centers \mathbf{o} and \mathbf{c}

1. Estimate $\overline{\mathbf{oc}}$ and the distances $l_i = \|\overline{\mathbf{q}_i\mathbf{x}_i}\|$ using least-squares adjustment on Equations 16 and 17.
2. Estimate \mathbf{e} , an arbitrary point on $\overline{\mathbf{oc}}$, using 2D trilateration on a plane orthogonal to $\overline{\mathbf{oc}}$.
3. For each control point \mathbf{x}_i , estimate the camera center \mathbf{c}_i .
4. Compute the average camera center \mathbf{c} , using \mathbf{c}_i and their variance.
5. Compute the mirror center \mathbf{o} using Equation 15.

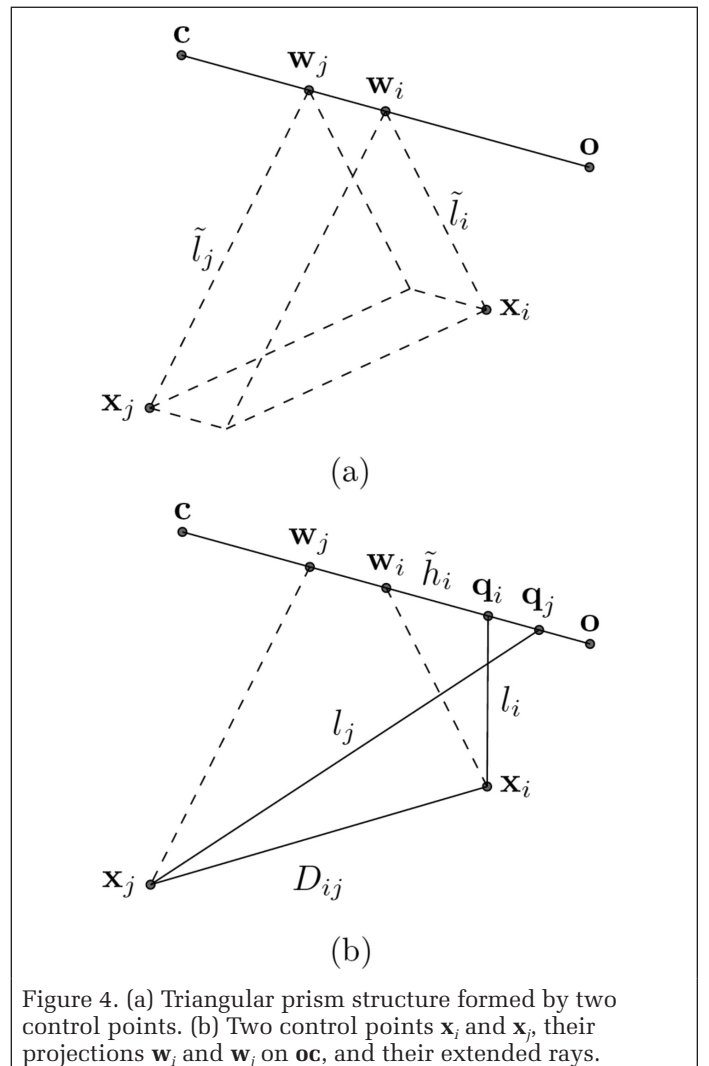


Figure 4. (a) Triangular prism structure formed by two control points. (b) Two control points \mathbf{x}_i and \mathbf{x}_j , their projections \mathbf{w}_i and \mathbf{w}_j on $\overline{\mathbf{oc}}$, and their extended rays.

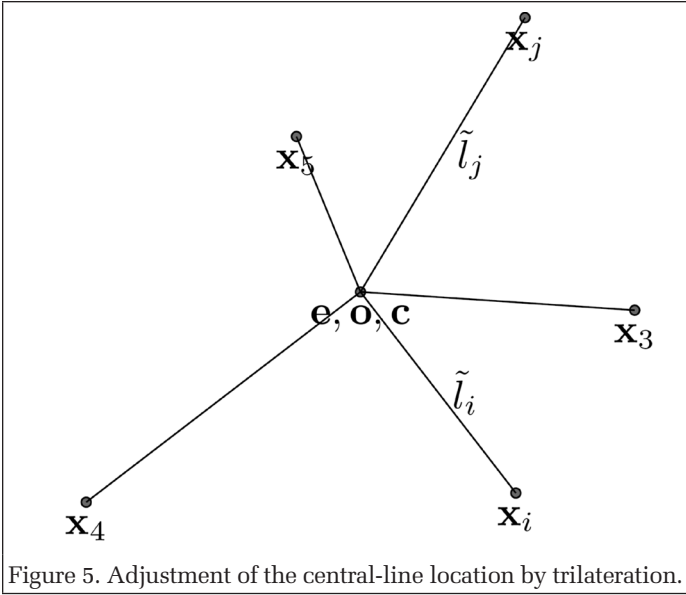


Figure 5. Adjustment of the central-line location by trilateration.

where the variables a_i and b_i are spelled out in the Appendix and $l_i = \|\mathbf{q}_i - \mathbf{x}_i\|$. Such a pair of constraints can then be written for each pair of points, altogether yielding a set of equations from which \mathbf{r}_1 and the l_i s can be estimated simultaneously.

To estimate the position of \mathbf{oc} , we take advantage of its known direction and project the reference points onto a plane orthogonal to it. Using the norm of the cross product between l_i and \mathbf{oc} , we have \tilde{l}_i , the projection of l_i on that plane (Figure 5); and then, using a 2D trilateration, we estimate \mathbf{y} , the position of \mathbf{oc} on that orthogonal plane.

The 2D coordinate of \mathbf{y} can be expressed as a projection of its actual 3D point \mathbf{e} onto that plane, namely $\mathbf{y} = \mathbf{P}_{2 \times 3} \mathbf{e}$, where the two row vectors $\mathbf{p}_{1,2}$ should be orthogonal to one another and orthogonal to \mathbf{r}_1 . To reconstruct \mathbf{e} , we reproject \mathbf{y} into 3D space: $\mathbf{e} = \mathbf{P}_{3 \times 2}^T \mathbf{y}$.

To compute \mathbf{c} , we first project the reference points on \mathbf{oc} (Figure 12d):

$$\mathbf{w}_i = \mathbf{e} + (\mathbf{r}_1^T \mathbf{x}_i) \mathbf{r}_1, \quad (18)$$

with \mathbf{w}_i the projected point. By using the distances $d_i = \|\mathbf{c} - \mathbf{q}_i\|$ (Equation 5), we have

$$\mathbf{c}_i = d_i \mathbf{r}_1 + \mathbf{q}_i = d_i \mathbf{r}_1 + \mathbf{q}_i - \mathbf{w}_i + \mathbf{w}_i = (d_i + \tilde{h}_i) \mathbf{r}_1 + \mathbf{w}_i, \quad (19)$$

where $\tilde{h}_i = l_i \cos(\phi_i)$. Notice that \tilde{h}_i , the difference between \mathbf{w}_i and \mathbf{q}_i along \mathbf{oc} , is essentially the difference in their x ordinates in the M system (Figure 12d). Using Equation 19, \mathbf{c} can be computed for each control point \mathbf{x}_i . However, a better result can be reached by computing \mathbf{c} as a weighted average of \mathbf{c}_i , and using the error propagation for l_i and \mathbf{r}_1 , which yields the weight $\lambda_i = \text{var}(\mathbf{c}_i)^{-1} / \sum \text{var}(\mathbf{c}_i)^{-1}$. Then the camera-perspective center is given by

$$\mathbf{c} = \sum_{i=1}^n \lambda_i \mathbf{c}_i, \quad (20)$$

and from Equation 15, \mathbf{o} can be computed.

Estimation of the Radius

The radius r of the sphere was implicitly considered as known thus far. If r is unknown, an additional parameter in the estimation of \mathbf{oc} 's direction is introduced and the constraints in Equations 16 and 17 become

$$\mathbf{r}_1^T (\mathbf{x}_i - \mathbf{x}_j) + g_0 r + g_1 l_j + g_2 l_i = 0 \quad (21)$$

$$-l_i^2 - l_j^2 + e_0 l_i l_j + e_1 r l_i + e_2 r l_j + e_3 r^2 + e_4 = 0, \quad (22)$$

allowing us to estimate r as well, where the variables e_i and g_i are spelled out in the Appendix. Later, under Estimation of the Radius and System Calibration, we describe an extension that allows us to incorporate multiple images.

Parameter Estimation Using DLT

The appeal of linear methods lies in direct estimation without the need for first approximations or iterations. Our representation (Equation 14) facilitates such derivations, where by dividing the last two rows by the first, the parameter u can be eliminated, leading to

$$\frac{r_{12}(x - c_x) + r_{22}(y - c_y) + r_{32}(z - c_z)}{r_{11}(x - c_x) + r_{21}(y - c_y) + r_{31}(z - c_z) + d_i} = w \cos(v)$$

$$\frac{r_{13}(x - c_x) + r_{23}(y - c_y) + r_{33}(z - c_z)}{r_{11}(x - c_x) + r_{21}(y - c_y) + r_{31}(z - c_z) + d_i} = w \sin(v) \quad (23)$$

where r_{ij} are elements of \mathbf{R} and c_x, c_y, c_z are the projection-center coordinates. Equation 23 can be rewritten as

$$\frac{L_5 x + L_6 y + L_7 z + L_8}{L_1 x + L_2 y + L_3 z + L_4 + d_i} = w \cos(v)$$

$$\frac{L_9 x + L_{10} y + L_{11} z + L_{12}}{L_1 x + L_2 y + L_3 z + L_4 + d_i} = w \sin(v) \quad (24)$$

where

$$\begin{bmatrix} L_1 & L_2 & L_3 \\ L_1 & L_2 & L_3 \\ L_9 & L_{10} & L_{11} \end{bmatrix} = \bar{\mathbf{R}} \quad \begin{bmatrix} L_4 \\ L_8 \\ L_{12} \end{bmatrix} = -\bar{\mathbf{R}} \mathbf{c}. \quad (25)$$

In linear form, it can be written as $\mathbf{A} \xi = \mathbf{b}$. From Equation 5 one sees that d_i is scaled by r , and as each row in \mathbf{b} contains d_i , r scales the entire model. Setting $r = 1$ leads to a scaled solution $\mathbf{A} \bar{\xi} = \mathbf{b}$, from which the system parameters can also be recovered. Note that there are 12 unknowns in this model, so at least six control points are needed.

To recover the model parameters from $\bar{\xi}$, we begin from Equation 25, which yields a scaled rotation matrix $\bar{\mathbf{R}}$. Using the singular-value decomposition $\bar{\mathbf{R}} = \mathbf{U} \mathbf{S} \mathbf{V}^T$, both $\bar{\mathbf{R}}$ and r can be recovered, with $\mathbf{R} = \mathbf{U} \mathbf{V}^T$ and r given by the reciprocal of singular values average:

$$r = 3 / \text{trace}(\mathbf{S}). \quad (26)$$

Using Equation 25, the projection center \mathbf{c} can be recovered by

$$\mathbf{c} = \bar{\mathbf{R}}^{-1} (L_4, L_8, L_{12})^T. \quad (27)$$

Recalling that $\mathbf{r}_1 = \bar{\mathbf{oc}} / \|\bar{\mathbf{oc}}\|$ and using the estimated values of α and r (Equations 4 and 26, respectively), \mathbf{o} can be computed from Equation 15.

Reconstruction of 3-Space Points

Finally, two or more images can be used to estimate the position of a point in object-space. Using Equation 11, we express the rays toward \mathbf{x} in the M -systems of two images (M_1 and M_2 , respectively) by

$$[\mathbf{x}]_{M_1} = u_1[\mathbf{p}_1]_{M_1} + [\mathbf{q}_1]_{M_1} \quad (28)$$

$$[\mathbf{x}]_{M_2} = u_2[\mathbf{p}_2]_{M_2} + [\mathbf{q}_2]_{M_2}, \quad (29)$$

where u_1 and u_2 are unknown scalars. Using the estimated model parameters, each of the rays can be transformed into object-space:

$$\mathbf{e}_i = \mathbf{R}_i[\mathbf{q}_i]_{M_i} + \mathbf{c}_i \quad (30)$$

$$\mathbf{s}_i = \mathbf{R}_i[\mathbf{p}_i]_{M_i}, \quad (31)$$

yielding

$$\mathbf{x} = u_1\mathbf{s}_1 + \mathbf{e}_1 \quad (32)$$

$$\mathbf{x} = u_2\mathbf{s}_2 + \mathbf{e}_2, \quad (33)$$

which form two lines in object-space that intersect in \mathbf{x} . We have six equations and five unknowns, (\mathbf{x} , u_1 , and u_2) and the point position in object-space can be estimated.

Results and Analysis

The performance of the parameter-estimation models is carried out over different control configurations, at different levels of noise and in the presence of outliers. First the models are analyzed, and then a more detailed study is performed for the case where both the radius and the positional parameters should be estimated.

The model is tested using both simulated experiments, under realistic imaging configurations, and real-world data. The imaging system consists of a standard pinhole camera and a spherical mirror, where the camera's intrinsic parameters are assumed to be calibrated in advance. Parameters similar to the real-world experiments were used for the synthetic tests, with $\mu = 500$ mm and $r = 74$ mm.

Influence of Control-Point Configurations on the Parameter Estimation

To test the quality of the estimation and the influence of the control-point distribution, we observe that the distribution of points in image-space has the greater influence on the solution (see earlier, under Transformation Between Planes of Reflection and Object-Space and Collinearity Equivalence). Thus, we describe the points by their angular image-related quantities: v and γ . Three different configurations are evaluated: a random distribution of points; an X-shaped arrangement, which represents an even distribution of the angle γ ;

and a circular arrangement of points, which represents an even distribution of the angle v (Figure 6).

The necessary number of control points is computed as follows: The resection model (Equation 14) yields three equations which include an unknown scale factor; therefore, only three control points are needed to estimate the six positional parameters (Table 1).

Three control points are also needed for the trilateration-based model, as they generate six independent equations. Avoiding degeneracy, these points should lie on two or more planes of reflection. Six control points are needed for the DLT method. Here we use 20 control points to ensure sufficient redundancy and distribution in image-space. We test with noise levels ranging from $\sigma = \pm 0.1$ to ± 1.5 pixels. Accuracy estimates of the model parameters are the standard deviation of 100 trials for each noise level.

Applying the resection model for the random point distribution (Figure 6a) yields submillimeter accuracy estimates for $\sigma = \pm 0.5$ pixels and estimates lower than 2 mm for ± 1 pixels (Table 2). The condition number of the *Gramian* matrix (Schwerdtfeger 1950) is 830. Notably, throughout the analysis,

Table 1. Number of minimum control points required for each model type.

Model type	Minimum points	Model type
Resection	3	Nonlinear
Trilateration	3	Nonlinear
Direct linear transform	6	Linear

Table 2. Parameter accuracy measures as a function of the noise level, using random point distribution (Figure 6a).

Method	Image noise	Camera position			Mirror position	
	$\sim N(0, \sigma)$ (pixels)	σ_x (mm)	σ_y (mm)	σ_z (mm)	σ_γ (mm)	σ_ν (mm)
Resection	0.1	0.03	0.16	0.14	0.06	0.06
	0.2	0.07	0.36	0.29	0.12	0.11
	0.5	0.17	0.86	0.74	0.31	0.33
	1.0	0.38	1.63	1.39	0.53	0.59
	1.5	0.54	2.86	2.26	0.88	1.05
Trilateration	0.1	0.02	0.08	0.08	0.03	0.03
	0.2	0.05	0.15	0.14	0.06	0.06
	0.5	0.10	0.34	0.37	0.14	0.17
	1.0	0.22	0.68	0.68	0.27	0.31
	1.5	0.33	1.03	1.13	0.43	0.50

Table 3. Accuracy measures for the position and orientation estimation of the central line.

$\sim N(0, \sigma)$ (pixels)	σ_θ (°)	σ_d (mm)
0.1	0.01	0.01
0.2	0.01	0.02
0.5	0.04	0.05
1.0	0.07	0.11
1.5	0.11	0.15

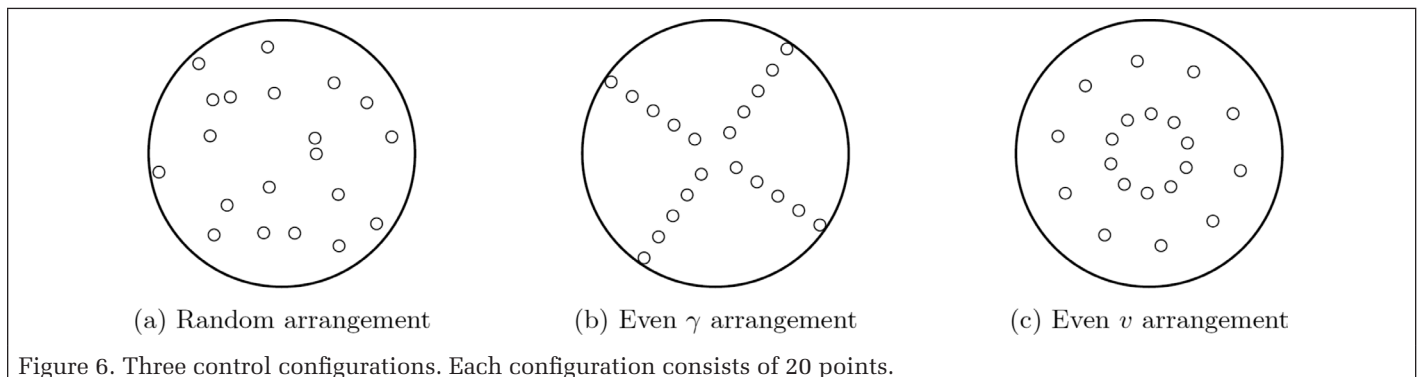


Figure 6. Three control configurations. Each configuration consists of 20 points.

σ_x of the mirror is omitted as the camera-mirror position along the central line is related by the distance μ , which is computed in advance as a function of α (Equation 4). The angle α is the outcome of a separate adjustment process, and being accurately estimated, its influence on the accuracy of μ is negligible. As an example, for $\sigma = \pm 1$ pixel, $\sigma_\alpha = \pm 1 \times 10^{-4}$ rad, which translates to $\sigma_\mu = \pm 0.01$ mm for $\mu = 500$ mm.

The trilateration model is performed in two adjustment steps—one to estimate \overline{oc} 's orientation and the other for its position in object-space. The condition number is 5.3 for the first step and 1 for the second, an improvement of two orders of magnitude compared to the resection-based solution. As the first phase concerns the determination of \overline{oc} , we analyze its accuracy under different noise levels, with σ_d being the estimated variance for the distance and σ_θ for the angle between the actual and estimated lines (Table 3). The results show that even for $\sigma = \pm 1.5$ pixels, the accuracies are on tenth-of-a-millimeter and tenth-of-a-degree levels in position and orientation, respectively. Returning to the trilateration-based solution, accuracy estimates for the camera and sphere's pose-parameters are listed in Table 2 and show two- to threefold improvement in the positional parameters compared to those reached by the resection model. They are on a submillimeter level even for a noise level of $\sigma = \pm 1$ pixel (Table 2). Note also that the accuracy measures are proportional and linearly linked with the increase of noise.

The X-shaped point arrangement offers an even distribution in γ along two planes of reflection (Figure 6b).³ Estimates for the resection model (Table 4) show some improvement in accuracy but not on a significant level, with a nearly similar condition number of 832. The trilateration method yields condition numbers of 5.3 and 1.1 for the first and second steps, respectively, similar to those of the random distribution. The accuracy levels (Table 4) are similar to the ones obtained when the distribution was random, and again, better by a factor than those obtained using the resection approach.

The circular point arrangement offers fixed γ values and an even distribution in v (Figure 6c). Accuracy measures for the resection model are somewhat higher than the previous two, but not on a significant level (Table 5), while the condition number drops to 103. The condition numbers for the trilateration model are 6.7 and 1 for the first and second phases, respectively. The effect of measurement noise on the results is listed in Table 5.

The correlations among the estimated parameters are low in general. Relatively high correlations can be observed between the Y and Z values, reaching 88% for the resection-based solution (Table 6), but dropping to 55% when the trilateration-based model is applied (Table 7). The rate of convergence shares similar patterns to those of the conventional central-projection model for the resection-based solution, requiring first approximations which are close to the actual values. In contrast, the trilateration model is unaffected by first approximations, as long as the initial direction of \overline{oc} is not reversed. The choice of distances hardly has any effect. Convergence was reached by no more than five or six iterations for the first step and no more than two or three for the second.

Application of the DLT-based approach differs from the resection and trilateration approaches for its linearity (requiring no first approximations and iterations) and the inherent estimation of the radius. The minimal number of points here is six for the DLT, as it has 12 unknowns. When the model parameters were estimated using this model, the condition number was 2.7×10^{13} , far higher than that reached by the non-linear models. Also, the accuracy estimates of the system's

3. As a solution cannot be obtained using a single plane of reflection, this configuration is the minimal distribution of v .

Table 4. Parameter accuracy measures as a function of the noise level, using X-shaped arrangement (Figure 6b).

Method	Image noise	Camera position			Mirror position	
	$\sim \mathcal{N}(0, \sigma)$ (pixels)	σ_x (mm)	σ_y (mm)	σ_z (mm)	σ_Y (mm)	σ_Z (mm)
Resection	0.1	0.04	0.13	0.13	0.06	0.06
	0.2	0.08	0.28	0.27	0.12	0.12
	0.5	0.21	0.76	0.71	0.34	0.32
	1.0	0.47	1.43	1.40	0.62	0.58
	1.5	0.69	1.90	2.20	0.72	0.94
Trilateration	0.1	0.03	0.07	0.08	0.03	0.03
	0.2	0.05	0.16	0.16	0.07	0.06
	0.5	0.12	0.39	0.40	0.17	0.17
	1.0	0.25	0.81	0.70	0.35	0.32
	1.5	0.36	1.21	1.11	0.54	0.53

Table 5. Parameter accuracy measures as a function of the noise level, using the two-circles arrangement (Figure 6c).

Method	Image noise	Camera position			Mirror position	
	$\sim \mathcal{N}(0, \sigma)$ (pixels)	σ_x (mm)	σ_y (mm)	σ_z (mm)	σ_Y (mm)	σ_Z (mm)
Resection	0.1	0.02	0.08	0.07	0.04	0.04
	0.2	0.05	0.17	0.16	0.08	0.08
	0.5	0.12	0.42	0.48	0.22	0.25
	1.0	0.27	0.82	0.97	0.47	0.52
	1.5	0.37	1.29	1.45	0.77	0.78
Trilateration	0.1	0.02	0.07	0.08	0.04	0.04
	0.2	0.04	0.15	0.15	0.07	0.07
	0.5	0.10	0.35	0.35	0.17	0.17
	1.0	0.23	0.65	0.67	0.38	0.35
	1.5	0.30	1.22	1.13	0.57	0.56

Table 6. Correlation matrix of model parameters, for resection with a given radius.

	Camera position			Mirror position		
	X (mm)	Y (mm)	Z (mm)	X (mm)	Y (mm)	Z (mm)
X (mm)	1.00	-0.10	0.11	1.00	0.06	-0.14
Y (mm)	-0.10	1.00	-0.08	-0.10	-0.88	0.16
Z (mm)	0.11	-0.08	1.00	0.11	0.13	-0.88
X (mm)	1.00	-0.10	0.11	1.00	0.06	-0.14
Y (mm)	0.06	-0.88	0.13	0.06	1.00	-0.19
Z (mm)	-0.14	0.16	-0.88	-0.14	-0.19	1.00

Table 7. Correlation matrix of model parameters, for trilateration with a given radius.

	Camera position			Mirror position		
	X (mm)	Y (mm)	Z (mm)	X (mm)	Y (mm)	Z (mm)
X (mm)	1.00	-0.03	-0.22	1.00	0.07	0.01
Y (mm)	-0.03	1.00	0.21	-0.03	-0.57	-0.08
Z (mm)	-0.22	0.21	1.00	-0.22	-0.23	-0.54
X (mm)	1.00	-0.03	-0.22	1.00	0.07	0.01
Y (mm)	0.07	-0.57	-0.23	0.07	1.00	-0.08
Z (mm)	0.01	-0.08	-0.54	0.01	-0.08	1.00

Table 8. Accuracy estimates using direct linear transform as a function of the noise level for a random point distribution (Figure 6a).

Control points	Image noise (pixels)	Camera position			Mirror position		Radius σ_r (mm)	μ σ_μ (mm)
		σ_x (mm)	σ_y (mm)	σ_z (mm)	σ_Y (mm)	σ_Z (mm)		
Random	0.1	3.84	0.32	0.36	0.56	0.12	0.11	0.55
	0.2	7.41	0.63	0.67	1.07	0.24	0.21	1.05
	0.5	19.50	1.74	1.64	2.84	0.66	0.48	2.75
	1.0	42.99	3.70	4.25	6.08	1.14	1.14	5.89
	1.5	73.92	6.80	5.89	10.49	2.11	1.55	9.47

parameters dropped (Table 8). Application of the DLT model for an X-shaped point arrangement improved the condition number to 3.1×10^{10} , but the results show a drop in the accuracy estimates for high image noise. For $\sigma = \pm 1$, accuracy estimates were $[\pm 65.90, \pm 1.32, \pm 1.54]$ mm for the camera position, $[\pm 9.11, \pm 0.45, \pm 0.01]$ mm for the sphere center position, and ± 9.93 mm for the radius. For brevity we note only that use of the circular point arrangement yielded lower accuracies than the previous two configurations. This drop and the high condition number relate to the fact that the solution involves 12 parameters which relate to only seven model parameters and the added radius, thereby leading to higher correlations and weakened model stability. Yet, because it is linear, parameters are obtained without iterations, making it an appealing way to derive approximated values for the trilateration model.

Impact of Outliers on the Estimated Parameters

We test the performance of the proposed models by introducing gross errors into up to 25% of the points and analyzing their impact on the estimation. Performance analysis shows that the resection model distributes the errors almost

uniformly, thus making them undetectable. In contrast, the trilateration model exhibits remarkable robustness to the presence of outliers even at such a rate. There is no need to resort to a strategy based on the random-sample consensus algorithm in order to filter them out (Figure 7). This robustness can be attributed in large part to both partitioning the problem into two smaller ones and using the trilateration-based strategy, which proves to be more immune to the influence of outliers. Consequently, the trilateration model provides not only better estimates and lower correlations but also robustness to potential outliers in the reference data. Clearly, in the more common case where an increase in the number of inlying control points is expected, the results will improve further as the outlier's effect on the estimation is reduced.

Comparison to the State of the Art

To test the model against the state of the art, we used the random configuration (Figure 6a) with 20 points and the same scene parameters, and compared it to the one proposed by Agrawal (2013), who also studied pose estimation of a camera and spherical-mirror system. The linear and nonlinear

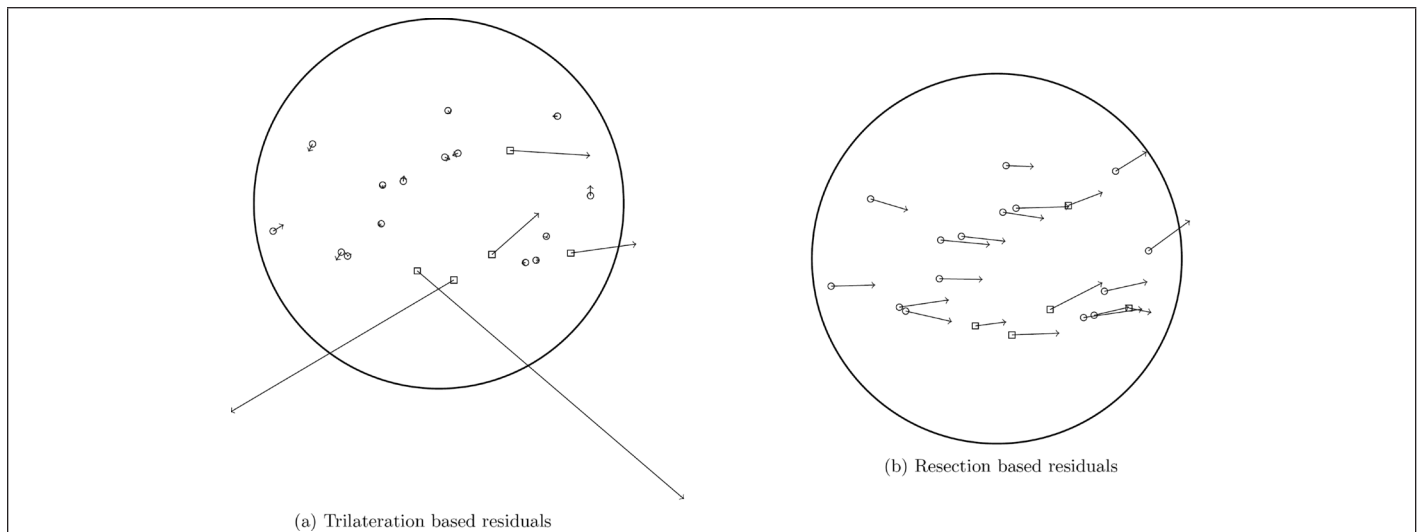


Figure 7. Residuals diagram in the image-space. Using the estimated camera and mirror location, the control points are projected to the image-space, and together with the original image-space samples form the residuals arrows.

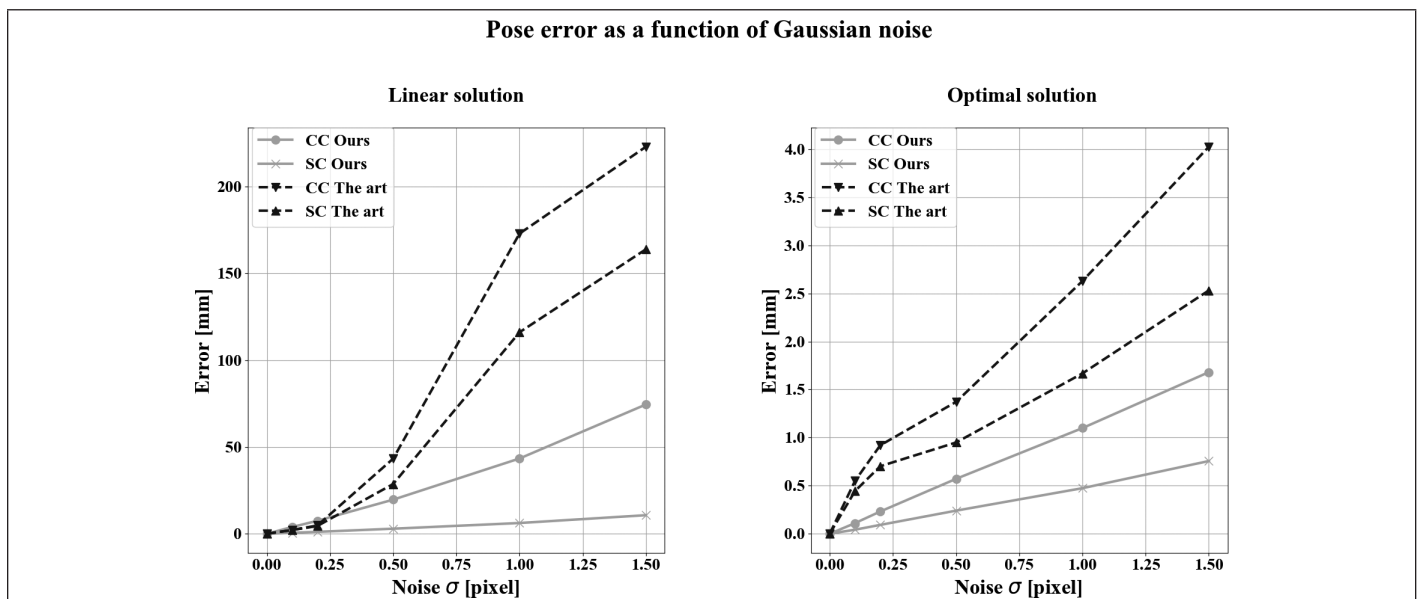


Figure 8. Accuracy-estimate comparison of our model to the state of the art as a function of the noise level for a random point distribution, Errors are measured by the norm of the distance between actual and estimated camera center (CC) and sphere center (SC). (a) The linear versions of both models; (b) the optimal, nonlinear models.

forms there are compared to our DLT and trilateration models, respectively (Figure 8). The errors in the plots are defined by the distance of the norm between the actual and estimated camera and sphere centers.

Application of the linear model shows that for an image noise greater than $\sigma = \pm 0.5$ pixel, a significant drop in accuracy is observed, probably due to the rotation-matrix extraction (Figure 8). These results are less accurate than those of our DLT-related model. They are comparable to a certain extent, as in both cases the solution involves estimation of the rotation matrix under the normality constraint, which we may assume become less stable when the noise level exceeds ± 0.5 pixel. The accuracy of the nonlinear solution (Figure 8) is lower by a factor compared to that of the trilateration-based model, and we may assume that the accuracy drop here is due to the fact that the camera-mirror distance is estimated explicitly. As indicated, the trilateration-based approach captures a more robust constraint of the catadioptric system, thereby yielding more accurate estimations of the parameters (Table 3). Moreover, and as shown in the previous subsection, it also produces robust results in the presence of outliers.

Estimation of the Radius and System Calibration

If the radius is unknown, both positional parameters and the radius r should be estimated simultaneously. Application of the DLT-based approach was evaluated earlier; here we extend this to the trilateration-based approach. The minimal number of points here is four (compared to six for the DLT). For the random distribution, the trilateration model yielded condition numbers of 23.6 and 1 for the first and second phases, respectively. The positional accuracy σ_x along the central line is 40 times higher than that reached when r was given (Table 9 compared to Table 2), while σ_y and σ_z are approximately the same. This rise relates to the system's geometry—as the control points are distributed around the camera axis, its position and orientation can be accurately determined (Table 3). However, as the position of the mirror and camera along that axis depends on γ , measurement noise can translate to an increase in r or to an offset in the camera position (Figure 9). An X-shaped arrangement did not much affect the condition number, which was 25.6 for the first phase. However, the accuracy estimates improved (Table 9), most likely because of the symmetric distribution of control points around the camera central line (angle ν). The accuracy estimates of the radius here are better than a millimeter for $\sigma = \pm 1$ and lower. Hence, we may conclude that while the point distribution had little effect on the pose parameter estimation, the X-shaped arrangement has value in calibrating the system.

Improved Estimation by Incorporation of Multiple Images

Because of the drop in positional accuracy along the camera axis, we consider the merit of incorporating multiple views. With

such a setup, each image has its own perspective center \mathbf{c}_i , angle α_i , and camera axis $\overline{\mathbf{oc}}_i$. These vectors point toward the same sphere center; thus, the following constraint can be introduced:

$$\mathbf{o} = \mathbf{c}_i + \frac{r}{\sin(\alpha_i)} \mathbf{r}_{1,i}, \quad (34)$$

where $\mathbf{r}_{1,i}$ is the normalized direction of $\overline{\mathbf{oc}}_i$. This constraint on its own has little effect on limiting the error along the camera axis, but it becomes effective when the baseline is constrained, $\|\mathbf{c}_1 - \mathbf{c}_2\| = b$, which also adds the equation

$$r \left\| \frac{\mathbf{r}_{1,1}}{\sin(\alpha_1)} - \frac{\mathbf{r}_{1,2}}{\sin(\alpha_2)} \right\| = b. \quad (35)$$

Both constraints (Equations 34 and 35) together with Equations 21 and 22 can be used to estimate $\mathbf{r}_{1,1}$, $\mathbf{r}_{1,2}$, the distances l_i , and r . This constraint improved the accuracy of the pose parameter estimation to that obtained when r was assumed known. The accuracy of r improved to ± 0.9 mm.

If the relative orientation between the two cameras is given in advance, the axes $\mathbf{r}_{1,i}$ will be known relative to one another and so will the perspective centers \mathbf{c}_1 and \mathbf{c}_2 . Then Equation 34 suffices to solve for \mathbf{o} and r . The radius value depends mostly on the accuracy of b , and for $\sigma_b = \pm 1$ mm we have $\sigma_r = \pm 0.8$ mm. Notably, improved accuracy of the relative orientation between the cameras will further improve the estimated calibration parameters.

Real-World Experiment

Testing the model on real-world data, we used a Nikon D70s camera with a fixed 24-mm Nikkor lens and an aluminum

Table 9. Accuracy estimates using trilateration as a function of the noise level for a random point distribution (Figure 6a) and X-shaped arrangement (Figure 6b).

Control points	Image noise (pixels)	Camera position			Mirror position		Radius	μ
		σ_x (mm)	σ_y (mm)	σ_z (mm)	σ_r (mm)	σ_μ (mm)		
Random	0.1	0.83	0.07	0.07	0.03	0.03	0.15	0.00
	0.2	1.58	0.16	0.13	0.05	0.05	0.28	0.00
	0.5	3.97	0.38	0.36	0.15	0.14	0.71	0.00
	1.0	8.30	0.77	0.72	0.28	0.32	1.50	0.01
	1.5	11.97	1.17	1.18	0.39	0.43	2.15	0.01
X-shaped	0.1	0.54	0.08	0.07	0.03	0.03	0.10	0.00
	0.2	1.11	0.15	0.16	0.07	0.06	0.20	0.01
	0.5	2.58	0.39	0.36	0.18	0.17	0.47	0.01
	1.0	4.40	0.68	0.77	0.27	0.34	0.97	0.03
	1.5	8.37	1.12	1.16	0.42	0.49	1.51	0.04

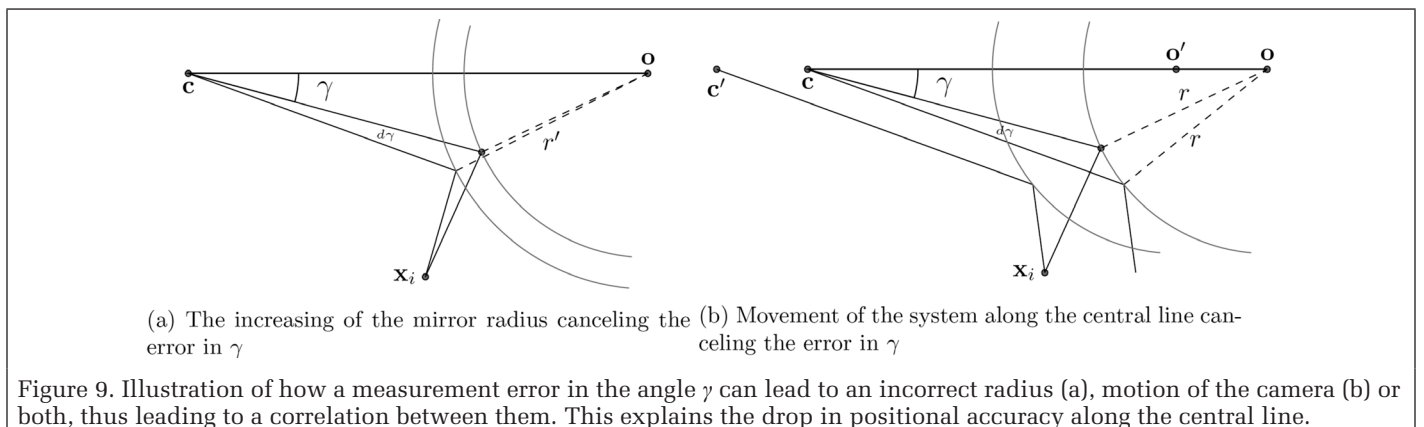
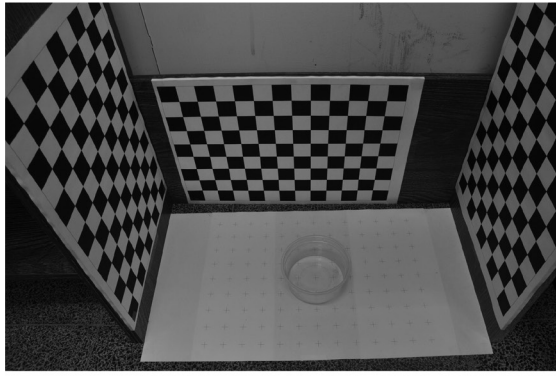
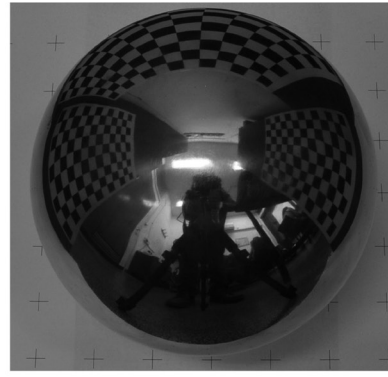


Figure 9. Illustration of how a measurement error in the angle γ can lead to an incorrect radius (a), motion of the camera (b) or both, thus leading to a correlation between them. This explains the drop in positional accuracy along the central line.

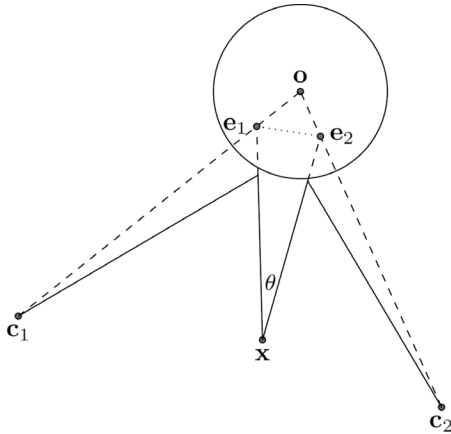


(a) Three vertical checkboard pattern planes.

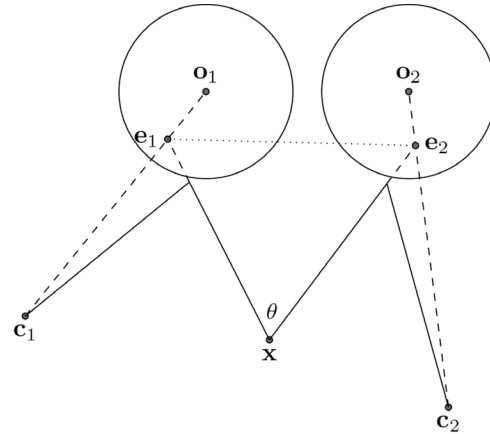


(b) A reflection of the vertical planes in the spherical mirror.

Figure 10. Experimental setup for the real-world experiment.



(a) Stationary mirror



(b) Two mirrors

Figure 11. Reconstruction using reflection from spherical surfaces.

spherical mirror with $r = 73.9$ mm for the experiments (Figure 10b). The spherical mirror was placed inside a box with three surrounding vertical planes covered by a checkerboard pattern (Figure 10a). In order to test the estimation of the camera and mirror pose parameters, their positions were first computed by a separate process. The camera pose parameters were estimated directly using checkerboard points for control (Figure 10a). The sphere position was measured in reference to the stand, allowing determination of the mirror horizontal position when placed on it. The center of the stand, which was circular, was measured from images, with accuracy which is submillimeter, and the height by geometric properties, all related to measures which were better than a millimeter.

The camera and mirror positions were then estimated using the trilateration model, by using the reflected control points. The difference between estimations for the camera position was $\Delta \mathbf{c} = (-0.2, -0.4, 1.2)$ mm, and the difference between the mirror positions was $\Delta \mathbf{o} = (-0.2, -0.9, 0.4)$ mm. The positional error along the central line is the same for the mirror and the camera, approximately 1 mm, similar to the synthetic results for a sampling error of $\sigma = \pm 1.5$ pixels. This is about the measurement accuracy which was obtained manually. A similar experiment was carried out when the radius was unknown. In that experiment the camera position error was $\Delta \mathbf{c} = (-1.2, -1.7, 0.4)$ mm, the mirror positional error was $\Delta \mathbf{o} = (-1.2, -0.9, 0.3)$ mm, and the radius error was $\Delta r = 0.3$ mm. Both results are in general agreement with those reached by the simulated tests (even outperforming the synthetic one when r was calibrated as well), indicating

that the model reflects actual imaging scenarios as well as the expected accuracy measures.

Measurement of 3-Space Points

Finally, we evaluate the application of the models to measurement of 3D object-space points. We have already demonstrated that once the camera and mirror position are estimated, reconstruction can be performed by intersection of the extended rays $\overline{\mathbf{q}_1 \mathbf{x}}$ and $\overline{\mathbf{q}_2 \mathbf{x}}$ (Equations 32 and 33). In that respect, the intersection of the extended rays with the camera axes at \mathbf{e}_1 and \mathbf{e}_2 is equivalent to the central-perspective baseline, which here becomes $\|\mathbf{e}_1 \mathbf{e}_2\|$ (Figure 11).

With this observation in mind, and with the understanding that higher accuracy can be reached with wider baselines ($\|\mathbf{e}_1 \mathbf{e}_2\|$), we study two scenarios: The first is the conventional one, in which two images are acquired through a stationary mirror, and the second is designed so that the baseline is extended. For this, we move not only the camera but also the spherical mirror between acquisitions (Figure 11b). To test the expected accuracy of both settings, we study a setup in which two images are acquired with a distance of $\|\mathbf{c}_1 \mathbf{c}_2\| = 770$ mm between them but the mirror is also shifted by $\|\mathbf{o}_1 \mathbf{o}_2\| = 280$ mm in the second setup. Comparing the baseline under both setups show that in the first one $\|\mathbf{e}_1 \mathbf{e}_2\|$ is equivalent to 114 mm, while in the second one it reaches 366 mm, three times wider. The accuracy estimate for a reconstructed point follows from here on a standard pinhole-camera model. We study the reconstruction accuracy of a fixed point \mathbf{x} for both scenarios. For the stationary case (Figure 11a) a narrow parallax angle is obtained compared to the second one,

with $\Delta\theta = 45^\circ$ ($\sim 15^\circ$ vs 60°), leading to a less accurate reconstruction. This is expressed in Table 10 for varying noise levels. The accuracy of the stationary scenario is twofold lower than that obtained by the second scenario.

Table 10. Estimated position accuracy measures as a function of the noise level.

Image noise $\sim N(0, \sigma)$ (pixels)	Position accuracy σ (mm)	
	Nonstationary	Stationary
0.1	0.05	0.14
0.2	0.11	0.34
0.5	0.28	0.73
1.0	0.55	1.56
1.5	0.83	2.34

Conclusions

This article studied pose estimation and 3D point reconstruction from a catadioptric system that consists of a camera and a spherical mirror. As demonstrated, this system forms an axial camera and remains so irrespective of the relative position or orientation between the camera and sphere. Derivation of measures within and between planes of reflection led to a closed form similar to the collinearity principle that was then extended into a direct linear-transformation model. The latter requires no first approximations or iterations. Further analysis of the system's geometry led to a novel trilateration-based model that proved robust to outliers, yielded improved estimates, and demonstrated stability, which was echoed in the single-digit condition numbers. Results and analysis show that accuracy estimates are better than the state of the art. Furthermore, the system radius can be calibrated, even at a submillimeter level of accuracy. The analysis shows that control configuration has little effect on accuracy, that a minimal number of control points is needed, and that degenerate configurations are limited. We also demonstrated the ability to apply our model in a calibration mode. In the case that the sphere boundary is completely unseen, an indirect means to estimate the angle between the tangent ray to the sphere and the camera axis should be applied. Evaluation of the reconstruction with this system managed to draw a resemblance to central-perspective cameras, thereby applying known principles in assessing the reconstruction accuracy. Finally, we note that use of spherical mirrors leads to an alternative modeling approach that helps broaden the imaging baseline, thereby contributing to high levels of accuracy. Future work would see application of this approach to outdoor scenes, evaluating accuracies and imaging settings.

Appendix

Having established the relation between measurable image-space quantities and object-space

coordinates \mathbf{x}_i (Equation 14), we wish to estimate the position and orientation of $\overline{\mathbf{oc}}$. To do so we first estimate the direction of $\overline{\mathbf{oc}}$ in object-space and the distances $l_i = \|\overline{\mathbf{q}_i\mathbf{x}_i}\|$.

In order to estimate l_i , we first decompose the vector $\overline{\mathbf{q}_i\mathbf{x}_i}$ into its parallel and perpendicular directions— \tilde{l}_i and \tilde{h}_i , respectively—in reference to $\overline{\mathbf{oc}}$ (Figure 12a):

$$\tilde{l}_i = \|\mathbf{w}_i - \mathbf{x}_i\| = l_i \sin(\phi_i) \quad (36)$$

$$\tilde{h}_i = w_{i,x} - q_{i,x} = l_i \cos(\phi_i), \quad (37)$$

where \mathbf{w}_i is the projection of \mathbf{x}_i on $\overline{\mathbf{oc}}$ and $w_{i,x}$ is the x ordinate of that vector. Note also that $q_{i,x} = d_i$ and can be computed by Equation 5. Similarly, given another control point \mathbf{x}_j , the values $l_j, \tilde{l}_j, \tilde{h}_j$ can be computed. We also define the distance $D_{ij} = \|\mathbf{x}_i - \mathbf{x}_j\|$ between two control points. Next we define $\tilde{\mathbf{x}}_i$, a point that lies on a line parallel to $\overline{\mathbf{oc}}$ that passes through \mathbf{x}_j , positioned at a distance $\|\mathbf{w}_i - \mathbf{w}_j\|$ from \mathbf{x}_j (Figure 12d).

We define $\tilde{D}_{ij} = \|\tilde{\mathbf{x}}_i - \mathbf{x}_j\|$ and $\tilde{d}_{ij} = d_i - d_j = q_{i,x} - q_{j,x}$ (Figure 12c). From measures along the camera axis and from Equation 37, we have

$$\tilde{d}_{ij} = w_{i,x} - w_{j,x} = (q_{i,x} - q_{j,x}) - (w_{j,x} - q_{j,x}) + (w_{i,x} - q_{i,x}) = d_{ij} - \tilde{h}_j + \tilde{h}_i. \quad (38)$$

From the law of cosines for $\Delta(\mathbf{w}_i, \mathbf{x}_j, \tilde{\mathbf{x}}_i)$ we have (Figure 12b)

$$\tilde{D}_{ij}^2 = \tilde{l}_i^2 + \tilde{l}_j^2 + 2\tilde{l}_i\tilde{l}_j \cos(\psi_{ij}). \quad (39)$$

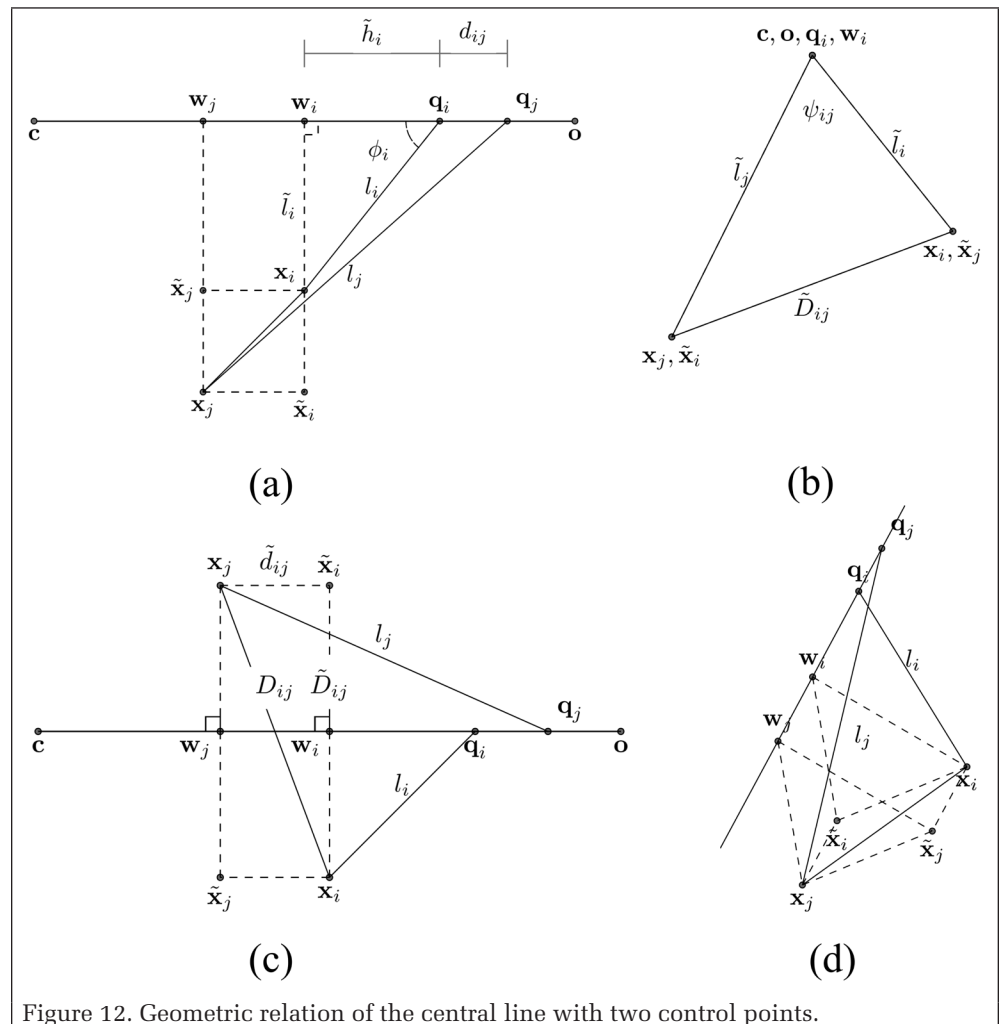


Figure 12. Geometric relation of the central line with two control points.

And from the Pythagorean theorem for $\Delta(\mathbf{x}_j, \mathbf{x}_i, \tilde{\mathbf{x}}_i)$ we know that (Figure 12c)

$$D_{ij}^2 = \tilde{D}_{ij}^2 + \tilde{d}_{ij}^2. \quad (40)$$

Rewriting Equation 40 in terms of l_i and l_j , we have

$$f(l_i, l_j) = -l_i^2 - l_j^2 + a_0 l_i l_j + a_1 l_i + a_2 l_j + a_3 = 0, \quad (41)$$

where $a_0 = 2 \sin(\phi_i) \sin(\phi_j) \cos(\psi_{ij}) + 2 \cos(\phi_i) \cos(\phi_j)$, $a_1 = -2d_{ij} \cos(\phi_i)$, $a_2 = 2d_{ij} \cos(\phi_j)$, and $a_3 = D_{ij}^2 - d_{ij}^2$.

Equation 41 defines a constraint for the pair l_i, l_j . We add another constraint D_{ij} such that its projection onto $\overline{\mathbf{oc}}$ is equal to d_{ij} . Since \mathbf{w}_i is the projection of \mathbf{x}_i on $\overline{\mathbf{oc}}$ (whose direction is \mathbf{r}_1), we have

$$\mathbf{r}_1^T \mathbf{x}_i = w_{i,x}. \quad (42)$$

Using Equations 37 and 38 we then have

$$\begin{aligned} \mathbf{r}_1^T (\mathbf{x}_i - \mathbf{x}_j) &= w_{i,x} - w_{j,x} = \tilde{d}_{ij} = d_{ij} - l_j \cos(\phi_j) \\ &+ l_i \cos(\phi_i) \Rightarrow \mathbf{r}_1^T (\mathbf{x}_i - \mathbf{x}_j) + b_0 + b_1 l_j + b_2 l_i = 0 \end{aligned} \quad (43)$$

where $b_0 = -d_{ij}$, $b_1 = \cos(\phi_j)$, and $b_2 = \cos(\phi_i)$. Using the constraints in Equations 41 and 43 for each pair of control points, a set of equations is formed, and l_i -s and \mathbf{r}_1 can be estimated.

Estimation of the Radius

When r is considered as an additional parameter, the constraint in Equation 41 becomes

$$-l_i^2 - l_j^2 + e_0 l_i l_j + e_1 r l_i + e_2 r l_j + e_3 r^2 + e_4 = 0, \quad (44)$$

where by defining $\bar{d}_{ij} = d_{ij}/r$ we have

$e_0 = 2 \sin(\phi_i) \sin(\phi_j) \cos(\psi_{ij}) + 2 \cos(\phi_i) \cos(\phi_j)$, $e_1 = -2\bar{d}_{ij} \cos(\phi_i)$, $e_2 = 2\bar{d}_{ij} \cos(\phi_j)$, $e_3 = -\bar{d}_{ij}^2$, and $e_4 = D_{ij}^2$ (note that \bar{d}_{ij} is independent of r); and the constraint in Equation 43 becomes

$$\mathbf{r}_1^T (\mathbf{x}_i - \mathbf{x}_j) = g_0 r + g_1 l_j + g_2 l_i, \quad (45)$$

where $g_0 = -\bar{d}_{ij}$, $g_1 = \cos(\phi_j)$, and $g_2 = -\cos(\phi_i)$. In this way r and $\overline{\mathbf{oc}}$'s direction are estimated.

References

Agrawal, A. 2013. Extrinsic camera calibration without a direct view using spherical mirror. Pages 2368–2375 in *Proceedings of the 2013 IEEE International Conference on Computer Vision*, held in Sydney, Australia, 1–8 December 2013. Edited by J. Editor. Washington, D.C.: IEEE Computer Society.

Barone, S., P. Neri, A. Paoli and A. V. Rationale. 2018a. Catadioptric stereo-vision system using a spherical mirror. *Procedia Structural Integrity* 8:83–91.

Barone, S., P. Neri, A. Paoli and A. V. Rationale. 2018b. Structured light stereo catadioptric scanner based on a spherical mirror. *Optics and Lasers in Engineering* 107:1–12.

Barreto, J. P., F. Martin and R. Horaud. 2003. Visual servoing/tracking using central catadioptric images. In *Experimental Robotics VIII*, edited by B. Siciliano and P. Dario, 245–254. Berlin: Springer.

Cinaroglu, I. and Y. Bastanlar. 2014. A direct approach for human detection with catadioptric omnidirectional cameras. Pages 2275–2279 in *2014 22nd Signal Processing and Communications Applications Conference*, held in Trabzon, Turkey, 23–25 April 2014. Edited by J. Editor. City, State/Country: Publisher.

Cinaroglu, I. and Y. Bastanlar. 2016. A direct approach for object detection with catadioptric omnidirectional cameras. *Signal, Image and Video Processing* 10 (2):413–420.

Francken, Y., C. Hermans and P. Bekaert. 2007. Screen-camera calibration using a spherical mirror. Pages 11–20 in *Fourth Canadian Conference on Computer and Robot Vision*, held in Montreal, Canada, 28–30 May 2007. Edited by J. Editor. Los Alamitos, Calif.: IEEE Computer Society.

Geyer, C. and K. Daniilidis. 2000. A unifying theory for central panoramic systems and practical implications. Pages 445–461 in *Computer Vision—ECCV 2000*, held in Dublin, Ireland, 26 June–1 July 2000. Edited by D. Vernon. Berlin: Springer.

Jaramillo, C., R. G. Valenti and J. Xiao. 2016. GUMS: A generalized unified model for stereo omnidirectional vision (demonstrated via a folded catadioptric system). Pages 2528–2533 in *2016 IEEE/RSJ International Conference on Intelligent Robots and Systems*, held in Daejeon, South Korea, 9–14 October 2016. Edited by J. Editor. City, Country: Publisher.

Kanbara, M., N. Ukita, M. Kidode and N. Yokoya. 2006. 3D scene reconstruction from reflection images in a spherical mirror. Pages 874–879 in *Proceedings of the 18th International Conference on Pattern Recognition, Vol. 4*, held in Hong Kong, China, 20–24 August 2006. Edited by Y. Y. Tang, S. P. Wang, G. Lorette, D. S. Yeung and H. Yan. Los Alamitos, Calif.: IEEE Computer Society.

Khurana, M. and C. Armenakis. 2018. Localization and mapping using a non-central catadioptric camera system. *ISPRS Annals of Photogrammetry, Remote Sensing & Spatial Information Sciences* 4 (2):145–152.

Lanman, D., D. Crispell, M. Wachs and G. Taubin. 2006. Spherical catadioptric arrays: Construction, multi-view geometry, and calibration. Pages 81–88 in *Proceedings of the Third International Symposium on 3D Data Processing, Visualization, and Transmission*, held in Chapel Hill, N.C., 14–16 June 2006. Edited by M. Pollefeys and K. Daniilidis. Los Alamitos, Calif.: IEEE Computer Society.

Marie, R., H. Ben Said, J. Stéphant and O. Labbani-Igbida. 2019. Visual servoing on the generalized Voronoi diagram using an omnidirectional camera. *Journal of Intelligent & Robotic Systems* 4 (3–4):793–804.

Mičusik, B. and T. Pajdla. 2004. Autocalibration & 3D reconstruction with non-central catadioptric cameras. Pages 1-58–1-65 in *Proceedings of the 2004 IEEE Computer Society Conference on Computer Vision and Pattern Recognition, Vol. 1*, held in Washington, D.C., 27 June–2 July 2004. Edited by J. Editor. Los Alamitos, Calif.: IEEE Computer Society.

Ohte, A., O. Tsuzuki and K. Mori. 2005. A practical spherical mirror omnidirectional camera. Pages 8–13 in *Proceedings of the 2005 IEEE International Workshop on Robotic Sensors: Robotic and Sensor Environments*, held in Ottawa, Canada, 30 September–1 October 2005. Edited by J. Editor. City, Country: Publisher.

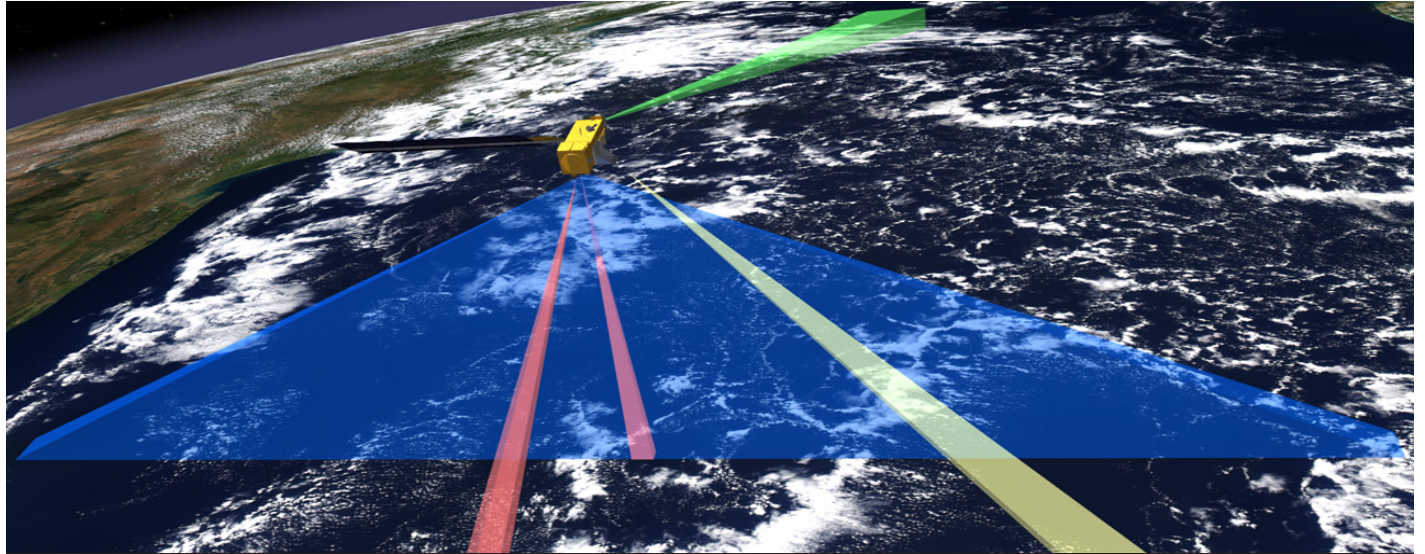
Ramalingam, S., P. Sturm and S. K. Lodha. 2006. Theory and calibration for axial cameras. Pages 704–713 in *Computer Vision—ACCV 2006*, held in Hyderabad, India, 13–16 January 2006. Edited by P. J. Narayanan, S. K. Nayar and H.-Y. Shum. Berlin: Springer.

Schwerdtfeger, H. 1950. *Introduction to linear algebra and the theory of matrices*. Groningen, the Netherlands: Noordhoff.

Taguchi, Y., A. Agrawal, A. Veeraraghavan, S. Ramalingam and R. Raskar. 2010. Axial-cones: Modeling spherical catadioptric cameras for wide-angle light field rendering. *ACM Transactions on Graphics* 29 (6):172.

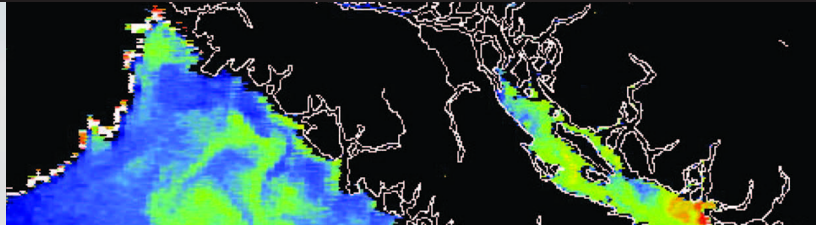
Xiang, Z., X. Dai and X. Gong. 2013. Noncentral catadioptric camera calibration using a generalized unified model. *Optics Letters* 38 (9):1367–1369.

Xiang, Z., Y. Zhou and X. Gong. 2015. A novel sub-camera array model for calibrating multi-mirror catadioptric systems. *Measurement Science and Technology* 26 (8):085402.



MANUAL OF REMOTE SENSING

Fourth Edition



Announcing the 4th Edition of the Manual of Remote Sensing

The fourth edition of the ASPRS *Manual of Remote Sensing, 4th Ed.* is an “enhanced” electronic publication available online from ASPRS. This edition expands its scope from previous editions, focusing on new and updated material since the turn of the 21st Century. Stanley Morain (Editor-in-Chief), and co-editors Michael Renslow and Amelia Budge have compiled material provided by numerous contributors who are experts in various aspects of remote sensing technologies, data preservation practices, data access mechanisms, data processing and modeling techniques, societal benefits, and legal aspects such as space policies and space law. These topics are organized into nine chapters. MRS4 is unique from previous editions in that it is a “living” document that can be updated easily in years to come as new technologies and practices evolve. It also is designed to include animated illustrations and videos to further enhance the reader’s experience.

The *Manual of Remote Sensing, 4th Ed.* will be available the beginning of 2020. All ASPRS members will have complimentary unlimited access to MRS as part of their ASPRS member benefits. Non-ASPRS members will be able to purchase access to MRS. More information will be announced in *PE&RS* and in the ASPRS eNewsletter. In the meantime, enjoy this preview of Chapter 1.

edited by: Stanley A. Morain,
Michael S. Renslow and Amelia M. Budge



Preface

The first *Manual of Remote Sensing* (MRS-1) was a 2-volume compendium exceeding 3100 pages published by the American Society of Photogrammetry (ASP) in 1975. It was meant to be a bridging device between ASP's *Manual of Photographic Interpretation* (published in 1944) and as a consequence was weighted heavily toward airborne and space-borne imaging. However, it included material on rapidly evolving technologies across both the visible and longer wavelengths of the electromagnetic (EM) spectrum. In fact, the term *remote sensing* has a longer and somewhat more shadowy history. Sometime in the 1950s, the term, as first used in the United States, is credited to Evelyn Pruitt, then at the U.S. Office of Naval Research (ONR), to describe the process for identifying, observing, and measuring radiation from objects on the Earth's surface. That such activities were in use in the '50s is confirmed by top secret Corona imagery obtained from high altitude U-2 over-flights of the Soviet Union and the downing of one flight piloted by Francis Gary Powers on May 1, 1960. Advances in these technologies, and their transformations over the past 60+ years, are the basis for the *Manual of Remote Sensing*.

MRS-1 (Vol. 1) was divided into 21 Chapters, reprising the unclassified histories of airborne cameras, camera systems, and the analytical techniques used to conduct qualitative and quantitative analyses across a wide range of Earth systems and environments. Several of the chapters included early results from the Earth Resources Technology Satellite (ERTS-1). Volume 2 was divided into 26 chapters introducing the electro-magnetic spectrum, energy/matter interactions, platform and sensor designs, sensor physics, data transmission, and data processing techniques required to convert electronic and photographic data into useful information about Earth environments. MRS-1 was a game-changer for ASP, which soon changed its name to the American Society for Photogrammetry and Remote Sensing (ASPRS). As transformative as it was, MRS-1 was encyclopedic. It can be found, if at all, in university and industry libraries.

MRS-2 was published in 1983. Like MRS-1, it was a two-volume set. Volume 1 addressed theory, instruments and techniques in 25 Chapters (1232 pages.); and Volume 2 addressed interpretation and applications in 10 Chapters (1207 pages.). Volume 2 also contained a lengthy color quire of aerial, satellite (mainly Landsat-1), and extraterrestrial images illustrating the range of image types and spatial resolutions then available. MRS-2 established the unclassified mathematical basis for acquiring and applying remotely sensed data to Earth's terrestrial, aquatic, and atmospheric environments, thus establishing the field as much broader than traditional photogrammetry. Its impact was to establish the technical basis for more than three decades of explosive growth in academic programs, remote sensing research centers, and global networking (1983-2009). It is now out-of-print but as of March 2015, was still available in limited quantities from online book sellers.

MRS-3 focused on the rapidly expanding range of platforms, sensors and applications in a series of hardcopy, thematic volumes. Between 1997 and 2009 six volumes were published before the program was terminated due to mounting publication costs and production delays (Table 1). In all, MRS-3 was just shy of 4000 pages, not including the color quires. Volume 1 (version 1) *Platforms and Sensors* was released as a searchable CD-ROM in 1997. It described both airborne and space-borne platforms and sensor designs, and a brief description of their data collection and transmission parameters. It was modernized and released in hardcopy as MRS-3 volume 1.1 in 2009. Between 1997 and 2006, Volumes 2 through 6 were released and

are available through ASPRS. Initially, the idea was to publish these as a series of thematic monographs on specific technologies and/or applications, each of which would be available at manageable cost to attract broader classroom use and avoid repeating earlier MRS content. The strategy of MRS-3 was to refresh MRS-2 sensor and application technologies in a series of thematic monographs. As it happened author/editors found that technologies were advancing on an upward curve and could be monitored on the World Wide Web while hard-copy publications were experiencing a downward spiral...close, but not close enough to the cutting edge. The unintended consequence was a long-delayed set of volumes that were increasingly too expensive for most of the intended market. Three volumes were published by Wiley Press, and three by ASPRS. Clearly, a different approach was needed. One interim approach was to retail books, or chapters of books, as downloadable PDFs (e.g., ASPRS’s LiDAR Manual (Renslow, 2013)). Hardcopy text books are still a common denominator for classroom instruction; but updating text books to keep pace with technological advances is ever harder.

Table 1. MRS-3 Production Data.

Title	Copyright	Number of Pages	Principal Author/Editors
Vol. 1 Earth Observing Platforms & Sensors	ASPRS, 1997	CD/ROM	S.A. Morain & A.M. Budge
Vol. 2 Principles & Applications of Imaging Radar	Wiley, 1998	866 + color quire	F.M. Henderson & T.J. Lewis
Vol. 3 Remote Sensing for Earth Resources	Wiley, 1999	707 + color quire	A.N. Rencz
Vol. 4 Remote Sensing for Natural Resources and Environmental Monitoring	Wiley, 2004	736 + CD/ROM no color	S.L. Ustin
Vol. 5 Remote Sensing of Human Settlements	ASPRS, 2006	752 + color quire	M.K. Ridd & J.D. Hipple
Vol. 6 Remote Sensing of the Marine Environment	ASPRS, 2006	338 (including color)	J.F.R. Gower
Vol. 1.1 Platforms & Sensors	ASPRS, 2009	520 + color quire	M.W. Jackson

MRS-4 was initiated in 2013. Headquarters’ staff recruited an editorial team to create a more effective, affordable, and durable Manual, and to broaden its scope to include economic and societal benefits. *Effective* in the sense that MRS-4’s content could be found online as an *enhanced e-book*; *affordable* in the sense that content could be retrieved by everyone on an annual subscription basis; and *durable* in the sense that it could be easily updated as a “living” manual through fresh, contributor-driven and vetted material as technologies advance. It does not reprise the extensive mathematical basis for remote sensing given in MRS-2, but instead focuses on system designs; data processing, storage, and retrieval; and on societal applications. A key feature of this concept is to facilitate timely updates of cutting edge or new developments from a wide spectrum of sophisticated contributors facile collectively with the technological, mathematical, and utilitarian aspects of Earth and space sciences. An example of these advances stemming from ever-finer spatial resolution is shown in Figure 1. Corresponding improvements in temporal and radiometric resolution also have contributed to the rapid expansion of Earth and Space applications.

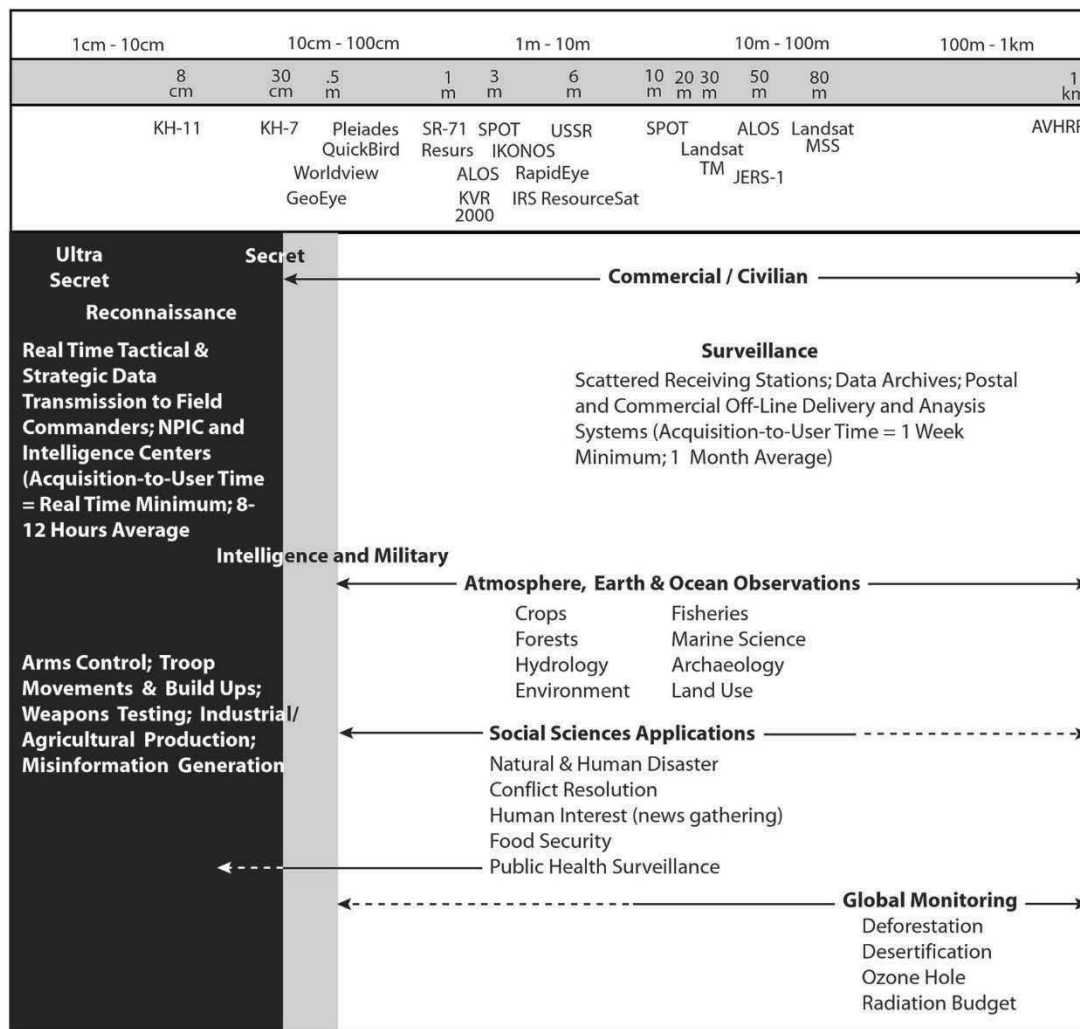


Figure 1. The range of social science applications expanded dramatically in the last decades of the 20th Century as system resolutions improved and were declassified. Compiled from data provided by Phillip Burrows, 1986, *Deep Black: Space espionage and national security*. New York: Random House.

MRS-4 is an enhanced *e-manual* available to the global community. The content is organized and compiled by chapter author/editors (A/Es) who are experts in their technical fields; and by contributors invited to develop topic-specific chapter elements. The overarching concept is that as an *e-manual*, MRS-4 should be updated as new subject matter and technological advances warrant. This implies that: (1) ASPRS maintains a mechanism for reviewing and vetting new and updated material submitted by contributors; and, (2) that this ongoing editorial process is flexible to accommodate new topics as well as revisions.

In future updates to MRS-4 a broader range of new and emerging remote sensing applications and results could be included such as data from *in-situ* sensors on the Moon, Mars, and perhaps including analysis of lunar samples and remote Martian samplers. These aims are ambitious in that most organizations like ASPRS, ISPRS and their international members (e.g., GEO, ICSU, UNESCO, and others) represent remote sensing communities-of-practice that rightly focus on Earth applications. But, there are other bodies like CEOS, a growing number of international space agencies, AIAA, and others that are dedicated also to solar system and astronomical research. These audiences also need sources of information that are produced by

their peers and that are up-to-date and vetted. Consequently, the potential of MRS-4 will be realized when these other audiences become regular users of a self-perpetuating and self-refreshing information sources that are not tied to expensive re-publications every few years.

Acknowledgement

ASPRS, the MRS-4 Editors-in-Chief, and Chapter Editors and their contributors acknowledge the generous support of the *University of New Mexico, Earth Data Analysis Center, and Geography Department* for providing office space, scanning devices, high speed printers, and communications equipment to generate the first version of MRS-4 as a “living electronic document.”

Stanley A. Morain

Earth Data Analysis Center, University of New Mexico, Albuquerque, NM, USA

Michael S. Renslow

Renslow Mapping Services, Eugene, OR, USA

Amelia M. Budge

Earth Data Analysis Center, University of New Mexico, Albuquerque, NM, USA

Chapter 1: Fundamentals of Electromagnetic Radiation

Stanley A. Morain

University of New Mexico, Albuquerque, NM, USA

Amelia M. Budge

University of New Mexico, Albuquerque, NM, USA

1 SCIENTIFIC BASIS FOR 21ST CENTURY REMOTE SENSING

Remote Sensing, its component sciences, technologies, and applications are all governed by the universal physics of energy interacting with matter at scales from subatomic to galactic. MRS-1, -2, and -3 describe hardware, software, and data processing developments for an exploding suite of airborne and space-borne platforms and sensors; and the resulting array of Earth and planetary science applications. These editions are overwhelmingly Earth-oriented to monitor Earth’s environments across spatial and temporal time-scales; and to develop methodologies for measuring and monitoring local-to-global phenomena. To maximize these capabilities, it has proven necessary for communities-of-practice to work within a broad framework that includes engineering designs that integrate environmental engineering, scientific, economic, human, and social considerations that, together, define the suite of remote sensing technologies. MRS-4 concentrates on state-of-the-art platforms, sensors, processing technologies and applications since the turn of the 2nd Millennium. Chapter 1 addresses basic matter and energy relationships as mathematical expressions; and where possible, as illustrated in animated and interactive graphics from the World Wide Web. However, much of the graphical material from the Web is limited to screen resolution (72dpi).

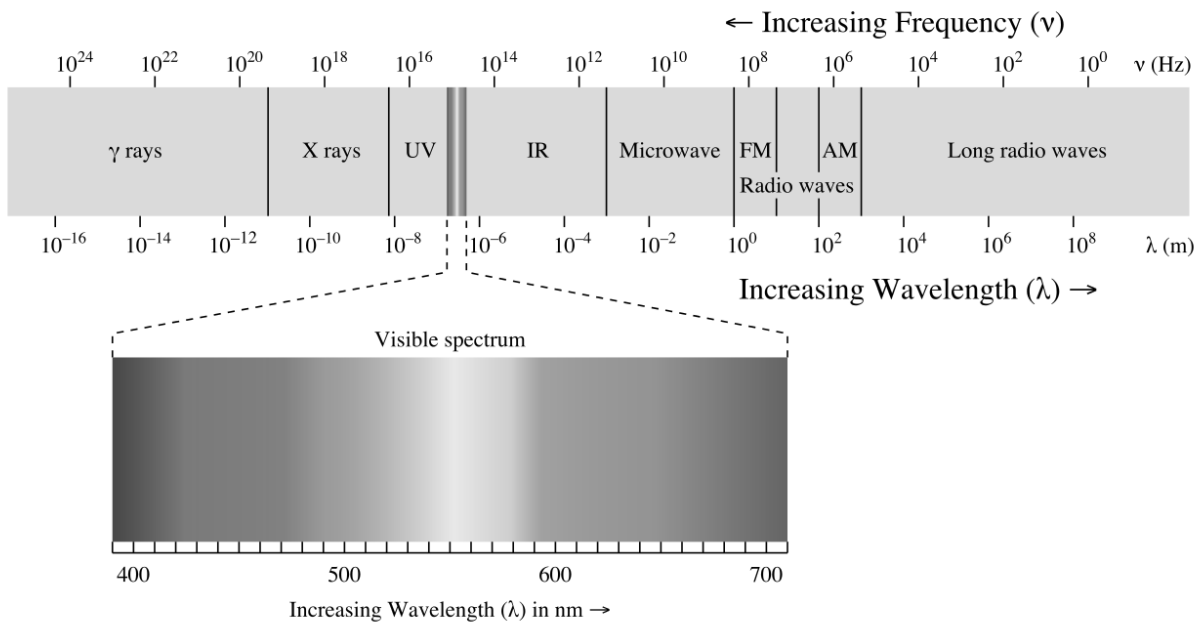


Figure 1-1. The EM-spectrum from gamma (γ) rays, where frequency exceeds 1024 Hertz (top left) and wavelengths (λ) are extremely short (10-16) meters, to radio wavelengths (top right) (Commons/Wikimedia). The human eyes' visible spectrum ranges from deep purple to ultra-red in the 400 to 700 nanometer (nm) spectral region.

For a short video visit http://chandra.harvard.edu/resources/flash/telescopes_light.html.

The term *remote sensing* was coined in the United States by Evelyn Pruitt at the U.S. Office of Naval Research (ONR) to describe processes for identifying, observing, and measuring radiation from objects on the Earth's surface (Graham, 1999; see <http://earthobservatory.nasa.gov/Features/RemoteSensing/>). Secret activities were in use in the 1950s in the form of Corona imagery obtained from high altitude U-2 flights over the Soviet Union and the downing of one flight piloted by Francis Gary Powers on May 1, 1960. For a concise pictorial history of early high altitude and space-based imaging programs see Baumann (2009) (<http://www.oneonta.edu/faculty/baumanpr/geosat2/RS%20History%20II/RS-History-Part-2.html>). Advances in these technologies over the subsequent five-to-six decades are the basis for the first three editions of the *Manual of Remote Sensing*.

1.1 Image Resolution

Resolution is a key parameter in remote sensing of any scene properties. It is a complex measure of image content arising from the various ways for describing the characteristics of a given system or image. Moreover, measuring spatial resolution differs between photographic systems and electronic systems. In the simplest case, spatial resolution has been defined as the minimum distance between two objects that a sensor can record distinctly. However, it is the format of the sensor system that determines how spatial resolution is measured. Measurements from one system may not be convertible to those obtained from another; and a single measure of spatial resolution cannot be applied satisfactorily to all sensor systems.

Forshaw *et al.* (1980) suggested that definitions of spatial resolution be placed into one of four categories: 1) the geometric properties of the imaging system, 2) the ability to distinguish between point targets, 3) the ability to measure the periodicity of repetitive targets, and 4) the ability to measure spectral properties of small, finite objects. Townshend (1980) provided a review of spatial resolution, including the measures listed above, and much of the following material comes from that paper.

Table 1-1 summarizes the different estimates of resolving power for the Landsat-1 Multispectral Scanner (MSS) calculated by different measures. In terms of the *geometric properties of the imaging system*, spatial resolution is usually described as *the instantaneous field of view (IFOV)*, which is a function of satellite orbital altitude, detector size, and the focal length of the optical system. For the visible and near infrared bands of Landsat-1, the IFOV is most commonly quoted as being $79m$. However, if the effects of cladding (using walls and adhesives) around the fiber optics are taken into consideration, the IFOV is reduced to $73.4m$ (Colvocoresses, 1979) or to $76.2m$ according to calculations by Slater (1979). Changes in the orbital altitude also cause the IFOV to change. Since Landsat altitude has varied from $880km$ to $940km$, the IFOV has varied from $76m$ to $81m$ (Gordon, 1980; see Table 1-1).

Table 1-1. Estimates of the Resolving Power of Landsat-1 MSS (Townshend, 1980).

Resolution Measure	Source	Resolution (meters)
IFOV-geometric	NASA, 1972	79
IFOV-geometric	Slater, 1979	76.2
IFOV-geometric	Colvocoresses, 1979	73.4
IFOV-geometric (min. altitude)	Gordon, 1980	76
IFOV-geometric (max. altitude)	Gordon, 1980	81
Pixel size	General Electric (undated)	79 x 56
Pixel size (resampled)	Holkenbrink, 1978	57 x 57
IFOV (point spread)	Landgrebe, <i>et al.</i> , 1977	90
EIFOV (half cycle)	Welch, 1977	66
IDFOV (full cycle)	Welch, 1977	135
ERE	Colvocoresses, 1979b	87
Modified ERE est. for band 4	Norwood, 1974	125
Minimum classifiable area	Shay, <i>et al.</i> , 1975	500 x 350
	General Electric, 1975	320 x 220

An IFOV value is not a true indication of the size of the smallest object that can be detected. An object of sufficient contrast with respect to its background, either brighter or darker, can change the overall radiance of a given pixel so that the object becomes detectable. Colvocoresses (1980) demonstrated this phenomenon using 61 *cm* mirrors arranged in the pattern of an “eye” and oriented to Landsat's view angle, one mirror per pixel. The ninety mirrors formed a pattern 2.52 *km* across and were detected because the reflection was sufficient to saturate the associated pixels. Conversely, on early vintage Landsat imagery, objects of medium to low contrast were only detectable if they occupied an area of 250 *m* or larger.

Perrin (1966) used the Rayleigh criterion for distinguishing between two point targets. A point source, even if viewed with a perfect or aberration-free lens, would not appear as a point source but as a central disk surrounded by faint dark and light rings. These features known as “Airy rings, are the result of diffraction. The Rayleigh criterion for distinguishing between two equal-intensity point-source targets with a perfect lens says that the two will just be resolvable if the central peak of the image of one source lies on the dark ring of the second. Once the angular separation is calculated and the height of the sensor above the ground is known, a measure of ground resolution may be derived. See <https://www.google.com/search?q=airy+rings&cad=h> for numerous examples and their relation to ground resolution in the visible spectrum. Since aberration-free lenses do not exist, actual lens resolutions must be less than the Rayleigh criterion.

Otterman (1969) derived a measure for extended circular targets because most remote sensing targets are neither points nor circular objects. For these reasons, making resolution estimates for square and rectangular objects also are required. Otterman showed that the diffraction-limited resolution for such sources is nearly six times coarser than for point sources.

Measures of resolution using the *periodicity of repetitive targets*, or “resolution targets” arose primarily from work using photographic images. On one commonly used form of resolution target, a pattern of parallel black lines on a white background provides a 100-to-1 contrast in the amount of light reflected. For each pattern, three black lines are used. The width of the space between adjacent lines is equal to the width of the lines in the pattern, and the length of each line is five times the width. Successive patterns on a target are composed of black lines and spacing of progressively narrower width. As the spacing between the parallel lines and the white background decreases, the contrast between them

will appear to be less until a point is reached when the contrast is so small that the parallel lines are indistinguishable from each other. Values of resolution derived in this way are consequently expressed by spatial frequency measures such as line pairs/*mm* which is sometimes abbreviated to lines/*mm*. Resolution may be expressed also in cycles/*mm* since the linear targets used often have a sinusoidally-varying tone (see <http://onlinetonegenerator.com/theory.html>) for a one page tutorial. The spatial frequencies of a linear target can be further characterized by the modulation transfer function (MTF). Modulation, a measure of contrast, is unity or near unity at low spatial frequencies and declines with higher spatial frequencies. The spatial frequency at which the modulation drops to zero is referred to as the cut-off frequency. The MTF of an image-forming system can be calculated from its design or measured in a laboratory. There are a number of MTFs which must be considered when examining the spatial resolution characteristics of a given remote sensor system (Slater, 1980). The two principal ones are related to the size of the detector or to the image displacement caused by linear image motion.

By using MTF curves, different measures of resolution can be derived at various frequencies. For example, a spatial frequency can be calculated where the modulation falls to a set proportion of its maximum value. The *effective instantaneous* field of view (EIFOV) is half the value of the spatial frequency for which the modulation of an object with a sinusoidal distribution of radiance has dropped to 50 percent of its original value as a result of the MTF of the system (Townshend, 1980; NASA, 1973). In Table 1-1, the EIFOV for the Landsat-1 multispectral scanner (MSS) as calculated by Welch (1977) is 66*m*. If the full cycle definition is used, a value of 132*m* is obtained.

A resolution employing *spectral properties of the target* is the effective resolution element (ERE). This measure is of interest because of the increasing importance of automated classification procedures, which are highly dependent on the fidelity of the spectral measurements recorded by the sensor system (Swain and Davis, 1978). Colvocoresses (1979) defined an ERE as the *size of an area for which a single radiance value can be assigned with reasonable assurance that the response is within five percent of the value representing the actual relative radiance*. By using this value, the calculated spatial resolution for the Landsat MSS is 80*m* (Table 1-1) (Colvocoresses, 1979). A refinement of this idea defines a modified ERE as the minimum area for which the spectral properties of the center can be assigned with at least 95 percent confidence that the values differ from the actual parameter values by no more than five percent of the full scale of the measuring instrument. Work done earlier by Norwood (1974) using Landsat MSS-1 data for agricultural scenes reflects a somewhat modified ERE concept. Norwood's results show that a five percent error in radiance values for Landsat bands 4 and 6 can be expected when the field size is approximately 125*m* and 200*m*, respectively. From the preceding, it is clear that no single definition suffices. Table 1-1 indicates that very different estimates of spatial resolution can be obtained for the same sensor. Which of the entries in the table represents the "actual" or "true" resolution? The answer depends on which image properties are of interest to the user as determined not only by the application, but also by the method of analysis.

Spatial resolution of a system must allow analysts to discern and analyze their phenomena of interest. These phenomena may be natural or cultural features, and they often coexist within the environment at macro-, meso-, and/or micro-scales. Each drop in scale requires progressively finer resolution to identify and analyze scene phenomena.

The spatial resolution that is germane to a given task is determined, in part, by the specific needs of the application: 1) the detection of objects, 2) their identification, or 3) their analysis. *Detection* determines whether something is present or absent. For example, within an image of large open rangeland areas objects are detected that are not consistent with rangeland vegetation. *Identification* results when enough information is available from the image data, or from other sources, to identify the objects (e.g., there may be trees along drainage lines in a broader expanse of rangeland). At the *analysis* level of resolution, information about the object is obtained beyond its initial identification (e.g., the trees in the rangeland are identifiable as cottonwoods lining streams; or more specifically, *Populus deltoides* ssp. *Wislizeni*, commonly known as the, *Rio Grande Cottonwood*, that is common to the western high plains of New Mexico and Colorado. To move from detection to identification, the spatial resolution must improve by about three times. To pass from identification to analysis, a further improvement in spatial resolution of ten times or more may be needed.

Since image information-content is resolution-dependent, a trade-off exists between the levels of resolution of most remote sensing applications. High spatial resolutions provide small area observations, but regional patterns may be difficult to characterize because generalizations may be required to obtain the high frequency information inherent in such images. Low or coarse spatial resolution allows regional patterns to be readily observed, interpreted and analyzed. However, detail may be averaged within picture elements (pixels), which can lead to a loss of information: Every system is sub-optimal for some or all of the objects in a scene.

Much of our knowledge about spatial resolution evolved between the 1950s and the end of the 20th Century, during which time technology transitioned from aerial and satellite photography; and subsequently to satellite-based photographic and electronic imaging systems.

1.2 *Landsat Program and Legacy*

The Landsat series of low Earth orbit (LEO) platforms began in 1973. Subsequent platforms carried more sophisticated sensors that, in turn, led to an ever widening array of applications.

1.2.1 *Program History*

In the mid-1960s, the U.S. National Aeronautics and Space Administration (NASA) began to develop and launch an Earth monitoring satellite to meet the needs of resource managers and Earth scientists. The U.S. Geological Survey (USGS) partnered with NASA in the early 1970s to assume responsibility for archiving data and distributing image and data products. On July 23, 1972, NASA launched the first in a series of satellites designed to provide repetitive global coverage of Earth's land masses. Designated initially as the *Earth Resources Technology Satellite-A*, it used a Nimbus-type platform modified to carry sensor systems and data relay equipment.

When operational orbit was achieved, it was renamed *ERTS-1*. The satellite continued to function well beyond its designed life-expectancy of one year; and finally ceased to operate on January 6, 1978. The second in the series was designated *ERTS-B*). It was launched on January 22, 1975; and was later renamed *Landsat-2* by NASA, which also renamed *ERTS-1* as *Landsat 1*. Three additional platforms were launched in 1978, 1982, and 1984 (*Landsat 3, 4, and 5*). In January 1983, operation of the Landsat system was

transferred to the National Oceanic and Atmospheric Administration (NOAA). In October 1985, the system was commercialized and the Earth Observation Satellite Company (EOSAT), assumed responsibility for its operation under contract to NOAA. Throughout these changes, the USGS EROS Data Center (EDC) retained primary responsibility as the Government archivist for Landsat data. The Land Remote Sensing Policy Act of 1992 (Public Law 102-5555) officially authorized the National Satellite Land Remote Sensing Data Archive and assigned responsibility to the Department of the Interior. In addition to its Landsat data management responsibility, the EDC investigates new methods of characterizing and studying changes on the land surface with Landsat data. This history is soon to be published jointly by USGS and ASPRS under the title *Landsat Legacy*.

1.2.2 Chronology and Characteristics of Landsat Systems

Landsat-1 through -3 operated in a near polar orbit at an altitude of 920 km with an 18-day repeat coverage cycle. These satellites circled the Earth every 103 minutes, completing fourteen orbits a day. Eighteen days and 251 overlapping orbits were required to provide nearly complete coverage of the Earth's surface with 185km wide image swaths. The amount of swath overlap or side-lap varied from 14 percent at the Equator to a maximum of approximately 85 percent at 81° north and south latitude. These satellites carried two sensors: a Return-Beam-Vidicon (RBV) and a multispectral scanner (MSS). The MSS sensor scanned the Earth's surface from west to east as the satellite moved in its descending (north-to-south) orbit over the sunlit side of the Earth. Six detectors for each spectral band provided six scan lines on each active mirror scan. The combination of scanning geometry, satellite orbit, and Earth rotation produced the global coverage necessary for studying land surface changes. The resolution of the MSS sensor was approximately 80m with radiometric coverage in four spectral bands from the visible green to the near-infrared (IR) wavelengths. Only the MSS sensor on Landsat 3 had a fifth band in the thermal-IR spectrum. The RBV sensor was essentially a television camera and did not achieve the popularity of the MSS sensor.

Landsat-4 and -5 carried both the MSS and the thematic mapper (TM) sensors; however, routine collection of MSS data was terminated in late 1992. These platforms orbited at an altitude of 705km and provided a 16-day, 233-orbit cycle with a swath overlap that varied from seven percent at the Equator to nearly 84 percent at 81° north and south latitude. These satellites were also designed to collect data over a 185km swath. The MSS sensors onboard Landsat-4 and -5 were identical to the ones that were carried on Landsat-1, -2 and -3. The MSS and TM sensors detected reflected radiation primarily from the Earth in the visible and IR wavelengths, but the TM sensor had seven spectral bands providing more radiometric information than the MSS sensor (see Table 1-2). The wavelength range for the TM sensor is from the visible (blue), through the mid-IR, into the thermal-IR part of the electromagnetic spectrum. Sixteen detectors for the visible and mid-IR wavelength bands in the TM sensor provide 16 scan lines on each active scan. Four detectors for the thermal-IR band provide four scan lines on each active scan. The TM sensor has a spatial resolution of 120m for the thermal-IR band and 30m for the other six radiometric bands. All of the Landsats have been in sun-synchronous orbits with equatorial crossing times ranging from 8:30am (local time) for Landsat-1, to 9:00am for Landsat-2, to the current time of approximately 9:45am for Landsat-5. Detailed system and sensor characteristics and operations are given in NASA (1979) and USGS/NOAA (1984).

1.2.3 Applications of Landsat Data

Landsat data have been used by government, commercial, industrial, civilian, military, and educational communities worldwide. They are being used to support applications that monitor global land-cover changes; agricultural patterns; deforestation and forest fires; geological phenomena (e.g. mining, volcanic eruptions, tracking lava flows and ash distributions); resource management; geography (e.g., land-use change, urban expansion); mapping; water quality; oceanography (e.g., El Niño, La Niña, typhoons, tsunamis and hurricanes); and human health (e.g., predicting malaria outbreaks, forecasting heat waves).

1.2.4 Spectral, Radiometric and Temporal Resolution

Spectral resolution is determined by the bandwidths of the channels used. Thus, high spectral resolution is achieved by having narrow bandwidths that, collectively, are able to provide a more refined spectral signature for discrete objects than are broad bandwidths. However, narrow-band instruments tend to acquire data with a low signal-to-noise (S/N) ratio, lowering the system's radiometric resolution. This situation can be alleviated if relatively long “look” or “dwell” times are employed; or, even better, if the sensor can “stare” at a particular scene of interest. In contrast, broad-band sensors usually have good spatial and radiometric resolution.

In the broader context of spectral resolution, there are tradeoffs between specific applications and spectral and radiometric resolution. Crop growth and development are probably better monitored using very narrow bandwidths in the visible and reflective infrared regions, as shown in Figure 1-2 for the Landsat multispectral scanner (MSS) bands and the Landsat-4 Thematic Mapper Bands. Monitoring sea state is probably best accomplished with multichannel active and passive microwave systems. Even within a discipline such as geology, specific applications are best studied using specific spectral ranges. Volcanism may be explored with broad thermal infrared bands of high radiometric resolution and surface geology may be mapped with Landsat images, aerial photographs or imagery acquired by means of active microwave systems, depending on the situation.

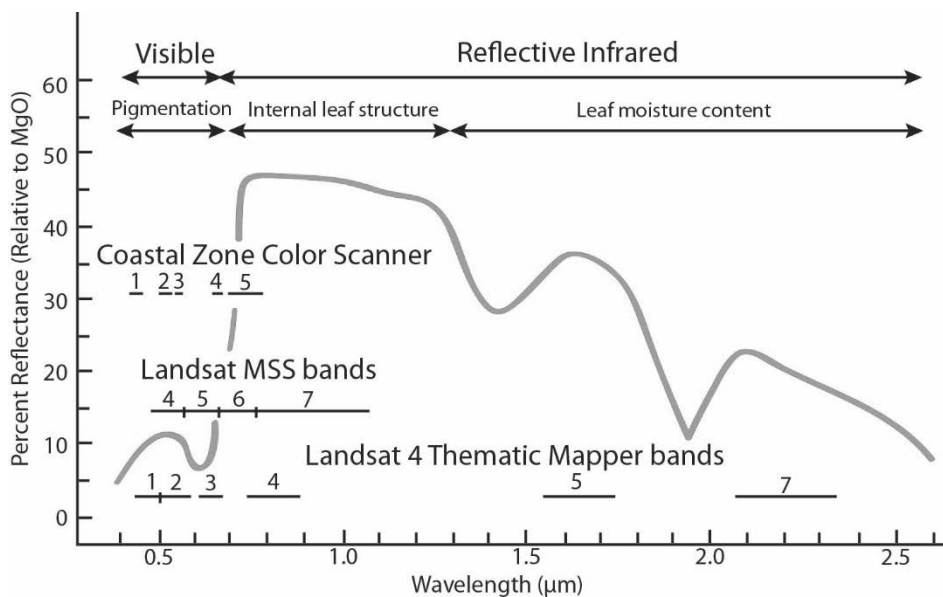


Figure 1-2. The blue line traces laboratory reflectances of green vegetation in the visible and reflective infrared spectral regions. The elements interacting with energy are primarily pigmentation, internal leaf structure and leaf moisture.

Radiometric resolution is determined by the number of discrete levels into which a signal may be divided. Considering the effects of varying illumination, the radiometric dynamic range of a sensor is determined by the maximum radiance value that the sensor system can experience for a given band. For example, the initial analog voltage signal of the Landsat MSS detectors is converted to digital count outputs ranging from 0 to 63 for a total of 64 quantizing levels. However, the maximum number of quantizing levels possible from a sensor system depends on the signal-to-noise ratio and the confidence level that can be assigned when discriminating between levels (Slater, 1980).

With a given spatial resolution, increasing the number of quantizing levels to improve radiometric resolution will improve discrimination between scene objects. Tucker (1979) found that the number of quantizing levels had a decided effect upon the ability to resolve spectral radiances that were related to plant-canopy status. Specifically, his analysis showed a per-channel improvement of two to three percent for 256 levels (Thematic Mapper bands 3 and 4) versus 64 levels (Landsat MSS). With such comparisons, it is essential to assess the cost/benefit ratio of improved, but more costly procedures; a two or three percent gain is modest for the extra processing costs involved.

Interdependencies between spatial, spectral, radiometric and temporal resolutions for each remote sensing instrument affect the various compromises and trade-offs. These trade-offs will be governed by the particular application or group of applications. To study housing quality within an urban area, high spatial resolution is needed. The information could be obtained by using panchromatic film (low spectral resolution). Forest inventories require fine spatial resolution to discriminate between species, but coarser resolutions, such as those available with some space sensors, may be adequate for discriminating between plant communities.

When trade-offs between spectral, radiometric, and spatial resolution occur, the fourth type of resolution, “time”, may achieve the needed discrimination. There are a few categories of objects and phenomena in nature that do not change with respect to one another or to themselves as a consequence of time; for example, geologic features, vast deserts, and oceans, but they do occur. Witness, for example, the onset of El Niño/La Niña episodes in the Pacific Ocean; and the subsequent outcomes of these *vis à vis* subsequent malaria outbreaks in Africa (Morain and Budge, 2013). For virtually all physical and cultural landscape features there are optimal times during which they may best be observed. These optimal “times” can vary between a few hours, days, weeks, or seasonally; and, they are interdependent if human activities and outcomes are being monitored. With many applications the time interval at which remotely sensed data are acquired becomes an important factor. To monitor crop growth, for example, images should be obtained at a predetermined time interval, perhaps every ten days. However, to monitor urban growth patterns, imagery acquired at time intervals of a year or more may be appropriate. Thus, in sensing a substantial number of dynamic events, such as crop growth, rangeland development, hydrologic processes, earthquake damage, urban change, and marine processes, time often may be used as the key discriminant.

Since one of the major premises of remote sensing is to monitor change through time, temporal resolution is an important consideration when determining the resolution characteristics of a sensor-system.

Perhaps of greater importance in the quest for the most economical remote sensing procedures is the trade-off between the time dimension and the other three dimensions of resolution. For an agricultural application, using time as a discriminant, together with local *a priori* data, such as can be obtained from an accurate crop calendar, often allow crops covering large areas to be identified with sensors possessing spatial and spectral resolutions that are too coarse to identify the same crops on the basis of spectral and morphological characteristics alone. Use of the temporal resolution may have the effect of reducing the cost of data acquisition and processing.

1.3 Landsat Data Continuity Mission (LDCM) Experience

The Landsat Data Continuity Mission (LDCM) was launched in February, 2013 as Landsat-8. Data returns are stored in archives for long-term preservation and distribution by the Department of Interior's U.S. Geological Survey (USGS). They constitute the longest continuous record of the global land surface as seen from space. Landsat data are critically important for understanding and managing forests, farms, changes in urban landscapes, responding to wild fires, measuring the extent of flood and storm damage, examining wildlife habitat, measuring glacial retreat, mapping the extent of the Antarctic ice sheet, and much more. Landsat data have become a part of America's infrastructure, and the data record constitutes a priceless archive that is open and freely available to everyone, everywhere.

NASA and the USGS collaborated to develop LDCM/Landsat-8. NASA was responsible for building and launching the satellite and its sensors and USGS led the development of the ground system. On May 30, 2013, USGS assumed responsibility for satellite operations and for collecting, archiving and distributing data and the spacecraft name was officially changed from the Landsat Data Continuity Mission (LDCM) to Landsat-8.

The scientific objective of Landsat-8 is to collect data sufficiently consistent with data from the earlier Landsat missions to permit studies of land cover and land use change over multi-decadal periods. Consistency in acquisition geometry, calibration, coverage characteristics, spectral and spatial characteristics, output product quality, and data availability have made it possible for people to compare Landsat data from month to month and year to year, and Landsat-8 will continue this tradition by collecting multispectral digital image data providing seasonal coverage of the global land mass.

The Landsat-8 satellite observatory consists of a spacecraft in low-Earth orbit, carrying two-sensors. One sensor, the Operational Land Imager (OLI), collects image data for nine shortwave spectral bands over a 185km swath with a 30m spatial resolution for all bands, except a 15m panchromatic band. The other sensor, the Thermal Infrared Sensor (TIRS), collects image data for two thermal bands with a 100m resolution over a 185km swath.

The Landsat-8 ground system sends daily commands to the observatory to schedule the coincident collection of OLI and TIRS data, and the transmission of the sensor data to a network of ground receiving stations. This network includes stations operated under the sponsorship of foreign governments. United States-operated stations forward the data on to the USGS Earth Resources Observation and Science (EROS) Center for processing, archiving, and distribution as part of the Landsat data archive. EROS distributes data products for all the OLI and TIRS spectral bands, both, corrected radiometrically and co-registered to the UTM cartographic projection, including correction for terrain effects. As with all of the Landsat data, EROS

distributes digital Landsat-8 data products over the internet to the general public on request and at no cost to requestors.

The Landsat-8 mission extends the more than 40-year Landsat data archive with images sufficiently consistent with data from the earlier missions to allow long-term studies of regional and global land cover change.

1.3.1 *LDCM Properties*

The Spacecraft has a terabit solid-state data recorder powered by a single $9 \times 0.4m$ solar array and a 125 Ampere-Hour (Ahr), Nickel-Hydrogen (NiH₂) battery. At launch, it weighed 2,071kg (4,566 lbs.) fully loaded with fuel (without instruments). Its length is 3m (9.8ft.), and its diameter is 2.4m (7.9ft). The communications package consists of a direct downlink with Solid State Recorders (SSR). Its data rate is 384 Megabits/s on X-band frequency; 260.92 Mbps on S-band frequency. Its orbital parameters include a: Worldwide Reference System-2 (WRS-2) path/row system; a Sun-synchronous orbit at an altitude of 705km; a 233 orbit cycle covering the entire globe every 16 days (except for the highest polar latitudes); an inclination of 98.2° (slightly retrograde) that circles the Earth every 98.9 minutes with an Equatorial crossing time: 10:00am +/- 15 minutes.

Sensors include the Operational Land Imager (OLI), which has nine spectral bands including a panchromatic band. Band 1 Visible (0.43-0.45 μm) 30m; Band 2 Visible (0.45-0.51 μm) 30m; Band 3 Visible (0.53-0.59 μm) 30m; Band 4 Red (0.64-0.67 μm) 30m; Band 5 Near-Infrared (0.85-0.88 μm) 30m; Band 6 SWIR 1 (1.57-1.65 μm) 30m; Band 7 SWIR 2 (2.11-2.29 μm) 30m; Band 8 Panchromatic (PAN) (0.50-0.68 μm) 15m; and Band 9 Cirrus (1.36-1.38 μm) 30m. The thermal infrared sensor (TIRS) has two spectral bands: band-1 (10.6-11.19 μm) and band-2 (11.5-12.51 μm) both having 100m resolution.

1.3.2 *Scale*

Scale is defined as the mathematical relationship between the size of objects as represented on maps or other imagery, and their actual size on the landscape. Scale should not be confused with spatial resolution. The spatial resolution of a Landsat Multi-spectral Scanner (MSS) image is approximately 79m, but the acquired data may be presented at different scales. The standard Landsat MSS product is a 9x9-inch print (0.2286km²) of an entire scene at a scale of approximately 1:1,000,000. However, because the data comprising the scene are digital, they can be presented at virtually any scale, such as 1:24,000; a scale compatible with the 7.5-minute topographic quadrangles produced by USGS. Selection of the appropriate scale is influenced by the resolution of the data, and both scale and resolution are application dependent.

1.3.3 *Information as a Scale-Dependent Phenomenon*

The scales at which data are collected and analyzed influence directly the level and kinds of information that may be obtained. It is appropriate to examine the relationships between data and information as a Venn diagram. Figure 1-3 shows the associations between remotely sensed data, ancillary data, and algorithm and theory development. The intersections of A and C, and B and C and (if it exists), A, B, and C, lead to scientific information; that is, a composite of quantitative observations and descriptions. Remotely sensed data alone are not scientific information. Figure 1-3 also shows that information is related fundamentally to algorithm and theory. It is only by connecting previously identified sets of

observations and data that remotely sensed data contain information; otherwise, the data gathered from the sensing instruments can be nothing more than possible building blocks for algorithms and theory (Morgenstern, 1950). Information derived from data collected at a particular scale is dependent on that scale. McCarthy *et al.* (1956) emphasize the scale-dependent nature of information as follows: "Conclusions derived from studies made at one scale should not be expected to apply to problems whose data are expressed at other scales. Every change in scale will bring about a statement of a new problem, and there is no basis for assuming that associations existing at one scale will exist at another."

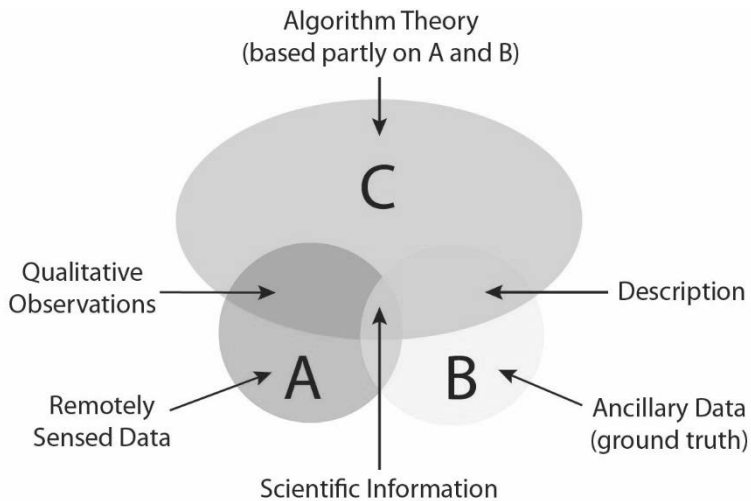


Figure 1-3. Associations between remotely sensed data, ancillary data, and algorithm and theory development (modified from Morgenstern, 1950).

What causes the dependency between scale and information? In the realm of remote sensing, the environment is ultimately the subject of most analyses. Within a scene, the size and surface characteristics of objects may vary considerably. Consequently, for that scene a single scale and resolution will not be appropriate for observing all scene components. For the analysis of large continuous geologic features in a region, the scale of a full-frame Landsat scene may be appropriate. However, difficulties will occur when one tries to identify individual bedding planes, discontinuous intrusive elements, and other features for which the combined scale and resolution are too coarse.

The appearance of objects will change with changing resolution and scale. Use of large-scale aerial photographs for a forested area can show individual crown shapes from which species, crown size, and closure may be determined. These data can then be used to extract measures of stand density and timber volumes. On Landsat imagery forest stands appear as broad classes of vegetation. Nevertheless, general physical parameters of the forest stand, such as tree height or stand density, may be determined from satellite data when these data are augmented by an acceptable sample design including ground or large-scale photographic observations (Strahler *et al.*, 1981).

1.3.4 Environmental Modulation Transfer Function (EMTF)

The variability of Earth's surface is one of the most pervasive problems encountered in remote sensing. Commenting on the spatial nature of the environment Townshend (1980) noted that there is a clear need for "... improved quantitative information about the spatial variability of terrain attributes if

their significance in affecting the usefulness of remote sensing data are to be fully appreciated." Not surprisingly, the environment and its fluctuating parameters remain the least known components of the remote sensing system. From the discussion above it is evident that the amount and quality of information that can be extracted from a remotely acquired image is a function of complex interactions between sensor parameters (e.g., resolution and scale) and scene dependent phenomena (e.g. socio-economic, biological, and geological spatial complexity).

The information obtainable from an analysis of remotely sensed data depends on variable characteristics of the given environment. Just as a sensor modulates the energy it receives, the environment modulates the information content of the scene. The concept of an environmental modulation transfer function (EMTF) was first proposed by Everett and Simonett (1976). They attempted to show how environmental complexity affects the amount of information extractable from remotely sensed data.

Fundamentally, Everett and Simonett contend that the environment is not passive to the electromagnetic energy that impinges upon it. Its variability in time, space, and number of functional categories affects information-extraction potential. This concept may be formalized by the equation

$$S = f(I, E) \quad (1-1)$$

where: S = system information (modulation) transfer function; I = instrument information (modulation) transfer function; and, E = environment information (modulation) transfer function.

The contributions to the environmental modulation transfer function may be expressed as

$$E = f(CR, SR, TR, AR, XR) \quad (1-2)$$

where: C_R = number of distinct land-use or mapping categories; S_R = size and spatial arrangement of the homogeneous categories of an area; T_R = a measure of the time-variable nature of the environment; A_R = a measure of the atmospheric constraints on sensing; and, X_R = other aspects of the environment.

The equations were developed to provide a formalized means of illustrating the interaction between sensor system resolution and the complexities of the environment which, together, modulate the data and ultimately the information. The EMTF emphasizes the previously stated concept that a single resolution used for multiple environments cannot and, indeed, will not produce uniform classes of information for all environments, or scene components.

The complexity and modulation of information from a given environment becomes more evident when the consequences arising from data aggregation are considered. The effects of environmental complexity are notably evident in Landsat data with their relatively coarse spatial resolution. Within a single resolution cell (pixel), two, three, or more land use or land cover categories may be present, each with its peculiarities of spatial size and location, class, spectral response and temporal nature. Therefore, depending on the environment (e.g. large agricultural fields versus urban patterns) many of the pixels may represent mixtures of functional information categories.

It is the presence of internal heterogeneities within individual functional categories that Wiersma and Landgrebe (1978) have called "scene noise." As an example, consider a residential area where imagery having high spatial resolution may reveal many separate land-cover components such as, roofs, road surfaces, grass, trees, and others. When imaged at a coarse spatial resolution,

such as that available from Landsat, these land-cover components become mixed within a pixel. This mixed pixel problem is compounded in small complex areas where multi-date registration is required. Misregistration, even by one pixel, could cause all land-cover components to be improperly mixed in time, and thereby confound accurate classification using machine-assisted analytical techniques.

1.3.5 Consistency

The EMTF illustrates in a more precise fashion how the dynamic nature of the environment affects the data recorded and the potential information. The potential for change within the domains of space, class, and time must be considered to ensure that the types of remotely sensed data and the respective ground truth remain mutually consistent. In other words, it is important to retain a level of internal consistency when interfacing data sets of various scales.

The level of consistency achievable in remotely sensed data is dependent upon two factors: the system resolution and the complexity of the environment being studied (Everett and Simonett, 1976). This idea is expressed as:

$$C = f[SR(s, \lambda, r, t), Env. Compl. (S, \lambda, Q, T) A] \quad (1-3)$$

where: C = level of consistency; SR = system resolution with respect to spatial (s), spectral (λ), radiometric (r) and temporal (t) components; and, $Env. Compl.$ = environmental complexity with respect to the frequency distribution of the spatial (S), categorical (λ), quantitative (Q) and temporal (T) domains of the environment for a given area (A).

Consistency is directly related to system resolution in the sense that by improving resolution will generally yield a higher consistency in the results. On the other hand, consistency is inversely related to the degree of environmental complexity in space and time, and in size of the study area. Suggested by these relationships is the notion that high levels of consistency may be obtainable for areas of continental size only if very general categories are specified. For example, Level I categories in the Anderson land-use classification (1972) is the level at which high consistency may be obtained with Landsat imagery over large areas. Level II categories are distinctly less consistent, and Level III categories are not at all consistent from locale to locale.

1.3.6 Scale and Aggregation

When dealing with information obtained at different scales, it is important to consider the degree of aggregation represented by each scale. Broadly stated, small-scale information requires an aggregation of data while large-scale information requires sub-division. Data aggregation occurs in both the temporal and categorical domains and in the spatial domain. The same consequences occur regardless of the domain in which the aggregation occurs. Two examples illustrate what happens when data are aggregated: 1) to the same level but according to different criteria; and, 2) to different levels for the same phenomenon. The first comes from economic statistics and the second from geographical analysis. Both have analogs in remote sensing.

An example of the accuracy of economic statistics by Morgenstern (1950) showed that figures reported for various national economic indices differed significantly between government agencies. These differences were a result of the way in which the data were aggregated. Aggregation was based on criteria

developed separately by each agency. It follows that data aggregation levels must be appropriate for the phenomenon being studied. It is unnecessary and costly to use data that are more specific than the level of analysis requires. Also, there may be relationships or classes contained within the data that might require them to be "smoothed" or aggregated to detect trends that could be lost in highly divided data.

1.4 *The "Multi" Concept*

From the preceding sections one can begin to recognize the various facets of remote sensing. The variety of data combinations provide analysts with more insight, and this has become a commonly accepted article-of-faith in the remote sensing community. In Chapter 1 of the first edition of the *Manual of Remote Sensing*, Colwell stressed the possibilities of the "multi" concept in remote sensing which he enumerated as: multi-date, multi-spectral, multi-station, multi-stage, multi-polarization, multi-directional, multi-enhancement, multi-disciplinary, and multi-thematic. In time, both the efficacy and weaknesses of these multiple techniques have been demonstrated. The capability for conducting "multi" remote sensing has improved. The elements of the concept are described below.

1.4.1 *Multi-stage*

Remote sensing is multi-stage in the sense that "progressively more information is obtained for progressively smaller subsamples of the areas being studied" (Colwell, 1975). Space-borne instruments commonly produce small scale, relatively coarse, resolution imagery and photography. When mosaicked to cover large areas, these products reveal surface features over large areas. The identification and subsequent study of small scale features and their relationships with the surrounding environment can be carried out with one, or a composite of a few, contiguous images. One of the principal uses of the small scale (1:500,000) imagery is to locate potential sites to be scrutinized in greater detail by progressively larger scale remotely sensed data and/or by other means. Small scale data may often be interpreted meaningfully by using information obtained from progressively larger scale remotely sensed data, or from ground or shipboard surveys of the area. Using smaller-scale to progressively larger-scale data was the basis for extensive test site programs undertaken in the 1960s (Lee, 1975).

1.4.2 *Multi-date*

Comparing images of the same area acquired at different instants in time can be used to create time lapse photography. Except for natural disasters, events recorded over longer periods of time (days, weeks, years, or even decades) reveal changes in landscapes associated with their spectral responses. By analyzing an area through time it is possible to develop analytical procedures based on these variations, and to differentiate classes of information accordingly. The principal advantage of multi-date analysis lies in the increased amount of information.

The seasonal changes for an area in the northern mid-west were documented on a month by month basis using Landsat images obtained from 1973 to 1976 (Lucas and Taranik, 1977). This sequence of images documented seasonal changes that took place on an annual cycle as different landscape components slip into and out of prominence on the images. It is thus possible to use time as a discriminant function, and take advantage of the way in which time modulates elements of the natural spatial system to

enhance them selectively. In an agricultural context, multi-date imagery records the phenology or developmental stages of crops. For identification, crops within an area can be partitioned according to their respective life-cycles, resulting in an increase in the probability of correct identification.

Multi-date imagery has long been recognized as a valuable tool for image analysis. Yet, the true power of incorporating multi-date imagery into landscape analysis lies in the speed of computer-assisted techniques. Computerized systems allow images to be viewed sequentially or simultaneously on a display screen, some at very rapid speeds. As technologies for computer systems have evolved, techniques for reviewing large image data bases has expanded into a wide range of data and information retrieval systems including natural landscapes, criminology, and gene sequencing, to name a few.

1.4.3 *Multi-band and Multi-spectral*

The electromagnetic energy emanating from Earth's land and water surfaces are recorded by instruments sensitive to various parts of the EM-spectrum. Although the radiation measured by a sensor is limited to the spectral sensitivities of its detectors, objects being sensed reflect and emit energy at many wavelengths. The characteristics of the energy emanating from a given feature depend largely on its atomic, molecular and macro-molecular composition. From the earliest days of remote sensing, the community-of-practice has borrowed the notion of spectral analysis in physics and chemistry to suggest that each feature tends to exhibit a unique "spectral signature." However, this multi-spectral analogy must be used with some caution. Its relative degree of accuracy varies geographically and environmentally. While it is correct that data from many spectral channels is an asset for researching problems, the selection of spectral channels for analysis is of equal, or possibly even greater, importance. The farther apart channels are located in the spectrum, the higher the independence of information obtained; the closer they are, the greater the redundancy. There is some merit, therefore, to obtaining multi-spectral data from bands that are far apart.

1.4.4 *Multi-polarization*

Conceptually, when treated collectively, the various waves comprising solar energy can be considered to be vibrating in all planes that are parallel to that beam as they travel through the atmosphere and impinge upon Earth's surface. However, the energy that is reflected back into the atmosphere from one kind of surface feature (e.g., a water body) may be strongly polarized (i.e., vibrating primarily in one plane), while energy reflected back from other surfaces such as vegetation or fractured rock, may be polarized only slightly.

With radar systems the polarization of the transmitted energy is an important consideration. It is less costly to have two receiving antennas than to have two transmitters. One system configuration might have a single transmitter that transmits in one plane of polarization and two receivers that receive both the parallel and orthogonal components. Provision needs to be made so that the antennae and receivers are sufficiently separated to avoid "cross-talk". Such a configuration provides a useful and cost effective system since, in some circumstances, the quality of information available from both the "like" and "cross" polarizations (HH and HV) of microwave radiation might augment information derived from just the HH and VV polarizations.

1.4.5 *Multi-directional*

Although most modern-day remote sensing is done with the sensor pointed vertically downward, there are instances in which more information can be obtained if images of the same area from one or more oblique orientations of the sensor are available. Sensors having multidirectional, or multiple look angles, enhances their prospects for obtaining data from an otherwise narrow field-of-view. Multi-directional images for radar analyses are particularly useful in that they allow a greater variety of features within a scene to be differentially enhanced. They also eliminate the bias due to enhancement of features aligned parallel to the flight path. Differential and biased enhancements of structured features in geology have been observed with low sun-angle illumination in Landsat images.

1.4.6 *Multi-enhancement*

There is a frequent need to glean critical information contained either in a set of multi-band images of an area taken at one date, or from a set of multi-date images of an area using one spectral channel. There are two ways in which imagery may be enhanced optically and digitally. In the digital domain, images can be enhanced by a number of techniques to aid visual analysis. Some of the different enhancements commonly used include contrast stretching, edge enhancements, and principal component analysis. These types of enhancements, especially when used interactively, may facilitate identification of features where further attention should be directed.

2 THE NATURE OF ELECTROMAGNETIC RADIATION

Editor's note: Topics and sub-topics in sections 2 through 5 of this Chapter are described in more detail on the World Wide Web. Many include animated and interactive graphics. Readers are encouraged to use the Web to better understand these physical/mathematical processes and phenomena in context of sensing Earth's environmental realms (physical, biological, cultural, economic). These are universal processes as humankind explores other planets in our solar system; and searches for other Earth-like planets in our near galaxy.

2.1 *Fundamental Properties of Electromagnetic Radiation (EMR)*

Energy is propagated as electromagnetic radiation (EMR) with a velocity of $3 \times 10^8 \text{ms}^{-1}$ from its source (the Sun), directly through free space, or indirectly by reflection and re-radiation to a sensor. EMR is also one of the most useful force fields for remote sensing, forming a high-speed communications link between sensors and receiving stations. Changes in the amount and properties of the EMR become a valuable source of data for interpreting important properties of the media with which it interacts. An understanding of the fundamental properties of this EMR communications link forms the foundation for its use in more sophisticated ways than normal human vision permits.

2.1.1 *Wave Properties*

Many remote sensing techniques utilize wave motion for detecting and identifying distant objects. Seismographs utilize seismic waves or stress waves in the crust of the Earth; microphones and human

hearing utilize sound waves in air; sonar sensors utilize sound waves in water; and electromagnetic (EM) sensors utilize EM waves. Some properties of wave motion are independent of the type of wave considered, while others are specific. Although this discussion will cover only the EM wave, a number of similarities may be recognized between the properties of these waves and of other waves, for example, sonic, and seismic.

2.1.1.1 Maxwell's Formulation

EMR is a dynamic form of energy manifested by its interaction with matter. In the early 1860s, James Maxwell unified the extant theories by Gauss (for electricity and magnetism); Faraday (for induction); and Ampere (for flow rate of one coulomb or charge per second, i.e., amp). In addition, he provided a logical basis for predicting the possible existence of the dynamic form of electric and magnetic phenomena in the form of wave motion; that is, electromagnetic radiation, or EMR. Maxwell considered EMR on a macroscopic scale, the interaction with matter depending upon electric and magnetic properties of matter. His formulation imposed no limitations on the possible frequencies, wavelengths, or amplitudes with which such radiation could occur. Gauss's laws for electricity and magnetism are given below in integral form together with those for Faraday's law of induction, and Ampere's law, respectively (equations 1-4 to 1-7). These equations are also expressed in differential form as Equations 1-8 through 1-11. The differential equations expressed are those in the absence of magnetic or polarizable media.

$$\text{Gauss' law for electricity: } \oint \vec{E} \cdot d\vec{A} = \frac{q}{\epsilon_0} \quad (1-4)$$

$$\text{Gauss' law for magnetism: } \oint \vec{B} \cdot d\vec{A} = 0 \quad (1-5)$$

$$\text{Faraday's law of induction: } \oint \vec{E} \cdot d\vec{s} = \frac{d\Phi_B}{dt} \quad (1-6)$$

$$\text{Ampere's law: } \oint \vec{B} \cdot d\vec{s} = \mu_0 i + \frac{1}{c^2} \frac{\partial}{\partial t} \int \vec{E} \cdot d\vec{A} \quad (1-7)$$

$$\text{Gauss' law for electricity: } \nabla \cdot E = \frac{\rho}{\epsilon_0} = 4\pi k\rho \quad (1-8)$$

$$\text{Gauss' law for magnetism: } \nabla \cdot B = 0 \quad (1-9)$$

$$\text{Faraday's law of induction: } \nabla \times E = -\frac{\partial B}{\partial t} \quad (1-10)$$

$$\text{Ampere's law: } \nabla \times B = \frac{4\pi k}{c^2} J + \frac{1}{c^2} \frac{\partial E}{\partial t} = \frac{J}{\epsilon_0 c^2} + \frac{1}{c^2} \frac{\partial E}{\partial t} \quad (1-11)$$

where: E = Electric field; ρ = charge density; i = electric current; B = Magnetic field; ϵ_0 = permittivity; J = current density; D = Electric displacement; μ_0 = permeability; c = speed of light; H = magnetic field strength; M = magnetization; and P = Polarization.

Maxwell's formulation and our modern theory of EMR are both based on the concept of a force field. When a compass needle is held near a magnetized piece of iron for example, the compass needle becomes oriented in a particular direction depending upon the location of the needle relative to the magnetized iron. Based upon the mechanical activity of the needle, one infers that a force is being applied to the two ends of the needle and that the force is caused by the magnetized iron. Yet nothing material connects the iron with the compass needle. When two compass needles are tied together with like poles in the same place, the effect of the iron on the pair is doubled. One can imagine that the iron produces something real

but nonmaterial in the surrounding space affecting everything that is placed there. Even if the compass needle is removed, the effect of the iron will still exist at that point; and is ready to cause a force on each compass needle with magnitude and direction depending upon the location of that point relative to the piece of iron. This non-material cause is a force field. A similar cause of force on electric charges is observed to surround electrified materials.

Maxwell's concept of EMR was that a mathematically smooth wave motion existed in the magnetic and electric force fields; a concept he formulated as a set of differential equations expressing the inter-relationship of electric and magnetic fields. Thus, in any region where there is a time rate of change of electric field, a magnetic field appears automatically in that same region as a conjugal partner. Similarly in a region where there is a time rate of change in magnetic field, an electric field appears. Therefore, the dynamic fields always occur together as inseparable partners so that neither purely electric nor purely magnetic radiated waves will occur separately from the other. When EM waves are intercepted by matter, the result will depend upon both the magnetic and electric properties of the matter.

Radiant flux density; that is, the time-rate at which radiation passes a spatial position, is proportional to the squares of wave amplitudes. These waves propagate through empty space at a fixed velocity, c approximating $3 \times 10^8 \text{ m/s}$. When the waves propagate through material, the velocity of propagation depends on the material's properties and the frequency of the wave. In all cases, the relation between the velocity of propagation (v), the wavelength λ , and the wave frequency ν is, $v = \lambda\nu$.

As the frequency does not change when the waves penetrate matter, the wavelength must change as the velocity of propagation changes. For instance, visible light propagates through glass with a velocity, v approximately $c/1.5$, so that the wavelength of the wave in the glass is shorter than in free space by a factor of 1.5. This factor is called the *index-of-refraction* and is usually designated by the Greek letter η .

2.1.1.2 The Superposition Principle and Wave Analysis

The *principle of superposition of wave motion* states that the wave motion produced in a region where two separate waves cross, produces a wave whose amplitude is the sum of the two separate waves. For waves in force fields, the amplitude is a sum, or a vector sum (Figure 1-4a). It is not self-evident that all wave motion should obey the superposition principle. Indeed, shock waves in air caused by supersonic objects do not. However, experimental observation indicates that EM waves in free space do move in accordance with this principle. Moreover, EM waves propagate through most common materials in conformance with the superposition principle, provided that the amplitudes of the force fields are not great enough to alter the material properties of the matter. One can expect that the superposition principle will apply to all EM waves likely to be encountered in remote sensing.

It is not self-evident that all wave motion should obey the superposition principle. Indeed, shock waves in air caused by supersonic objects do not. However, experimental observation indicates that EM waves in free space *do* move in accordance with this principle. Moreover, EM waves propagate through most common materials in conformance with the superposition principle, provided that the amplitudes of the force fields are not great enough to alter the material properties of the matter. One can expect that the superposition principle will apply to all EM waves likely to be encountered in remote sensing. This principle forms the foundation for analyzing very complicated wave motions by the superposition of many simple

and more easily understood waves. Those most frequently used for analysis are sinusoidal or simple harmonic waves. The French mathematician, Jean Baptiste Fourier, showed mathematically that any complicated wave form could be constructed by the superposition of an infinite number of these sinusoidal waves as components if the sinusoidal waves had the proper amplitudes, frequencies, and phases (or starting times).

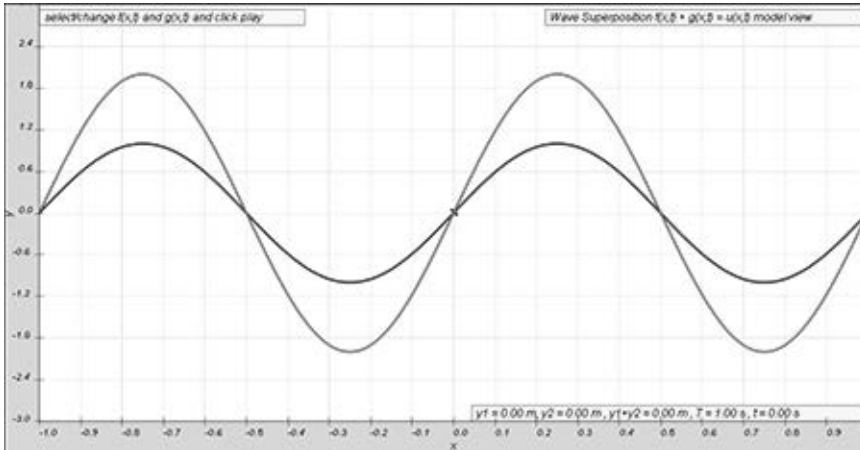


Figure 1-4a. Superposition of waves with different amplitudes at the same frequency (Credit: Wikimedia Commons).

Figure 1-4b is an example of wave superposition, amplitudes, and propagation produced by a tsunami 195km south of Apia, Samoa. It was triggered on September 9, 2009 by an 8.1 magnitude earthquake. Tsunami waves arrived at Pago Pago approximately 250km from the epicenter at 18:08 UTC. The movie traces the actual movement of waves and their diffraction patterns.

We hope you enjoyed this excerpt from Chapter 1 of the *Manual of Remote Sensing, 4th Ed.* Stay tuned for more to come.

ASPRS BOOKSTORE

visit asprs.org

available at
amazon

Digital Elevation Model Technologies & Applications, 3rd Ed

Co-Editors: David F. Maune, PhD, CP, CFM, PSM, PS, GS, SP and Amar Nayegandhi, CP, CMS-Remote Sensing
List Price: \$100 | **ASPRS Members:** \$80
ASPRS Student Members: \$50[†]
Also available for Amazon Kindle
Amazon Kindle Price:** \$85

Landsat's Enduring Legacy: Pioneering Global Land Observations From Space

Landsat Legacy Project Team
ISBN: ISBN 1-57083-101-7 · Hardcover · 586 pages · 2017 · Stock #4958
List Price: \$95 | **ASPRS Members:** \$65
Student Members: \$60
Amazon Price*: \$100

Manual of Airborne Topographic Lidar

Editor: Michael S. Renslow
ISBN: 1-57083-097-5 · Hardcover · 528 pages · 2012 · Stock #4587
List Price: \$150 | **ASPRS Members:** \$95
Student Members: \$75
Amazon Price (hardcover)*: \$135
Also available for Amazon Kindle
Amazon Kindle Price:** \$110

Manual of Photogrammetry, Sixth Edition

Editor: J. Chris McGlone
ISBN: 1-57083-099-1 · Hardcover · 1372 pages · 2013 · Stock #4737
List Price: \$175 | **ASPRS Members:** \$125
Student Members: \$98
Amazon Price*: \$175

Glossary of the Mapping Sciences

Co-published by ASPRS, ACSM and ASCE
ISBN: 1-57083-011-8
563 pp · Paperback · 1994 · Stock #5021
List Price: \$50 | **ASPRS Members:** \$35
Student Members: \$25 | **Amazon Price*:** \$50

Hyperspectral Remote Sensing for Forestry

Paul Treitz, Valerie Thomas, Pablo J. Zarco-Tejada, Peng Gong, and Paul J. Curran
ISBN: 1-57083-093-2
107 pp · Softcover · 2010 · Stock #4584
List Price: \$26 | **ASPRS Members:** \$21
Student Member: \$21 | **Amazon Price*:** \$26

Manual of Geographic Information Systems

Editor: Marguerite Madden, PhD
Foreword: Jack Dangermond, Esri
ISBN: 1-57083-086-X · Hardcover · 1352 pages + DVD · July 2009 · Stock #4650
List Price: \$53 | **ASPRS Members:** \$40
Student Members: \$40
Amazon Price*: \$55

Meeting Environmental Challenges with Remote Sensing Imagery

Editors: Rebecca Dodge & Russ Congalton
Published by American Geosciences Institute; Publishing Partners: AmericaView, USGS Land Remote Sensing Program, ASPRS
ISBN: 978-0-922152-94-0 · 82 pp · Softcover · 2013 · Stock #4589
List Price: \$7.50 | **ASPRS Members:** \$6
Bulk Orders (3 or more copies): \$4.50 each
Amazon Price*: \$9.95

MANUAL OF REMOTE SENSING, 3RD EDITION (A SERIES)

Earth Observing Platforms & Sensors

Volume 1.1
Volume Editor: Mark Jackson
ISBN: 1-57083-089-4
550 pp · Hardcover · 2009 · Stock #4582
List Price: \$95 | **ASPRS Members:** \$75
Student Members: \$55 | **Amazon Price*:** \$95

Remote Sensing of Human Settlements

Volume 5
Editor-in-Chief: Andrew B. Rencz
Volume Editors: Merrill K. Ridd & James D. Hipple
ISBN: 1-57083-077-0
747+ pp · Hardcover · 2005 · Stock # 4576
List Price: \$99 | **ASPRS Members:** \$80
Student Members: \$60
Amazon Price*: \$69.99

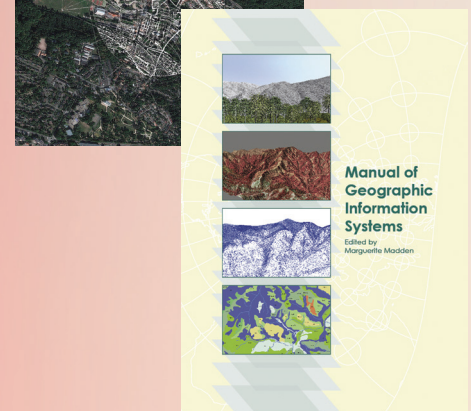
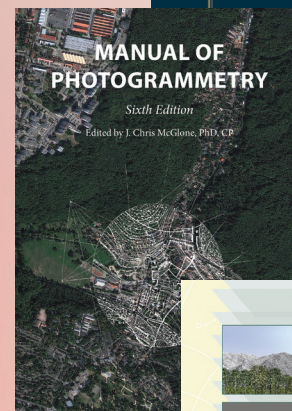
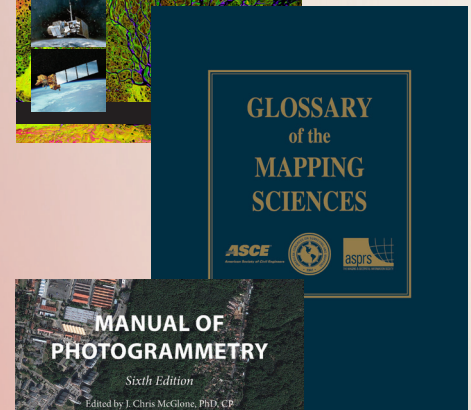
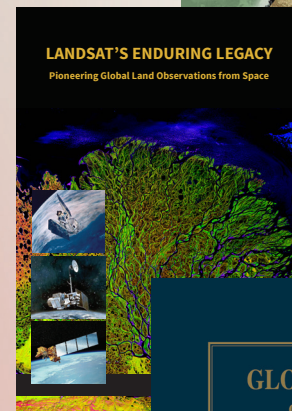
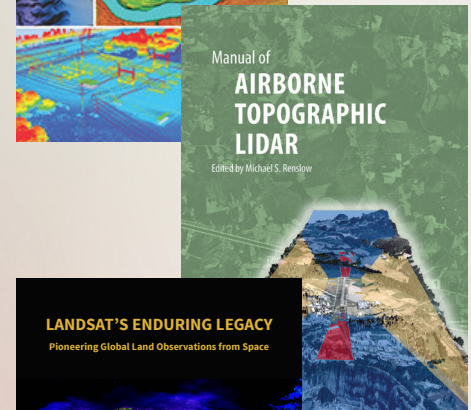
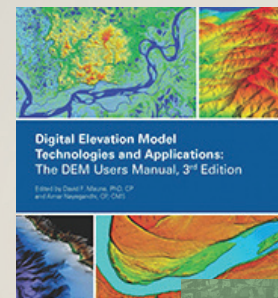
Remote Sensing of the Marine Environment

Volume 6
Editor-in-Chief: Andrew B. Rencz
Volume Editor: James F.R. Gower
ISBN: 1-57083-080-0 · 360 pp · Hardcover · 2006 · Stock # 4578
List Price: \$95 | **ASPRS Members:** \$75
Student Members: \$50 | **Amazon Price*:** \$95

*Member discounts are not available when ordering directly from Amazon.

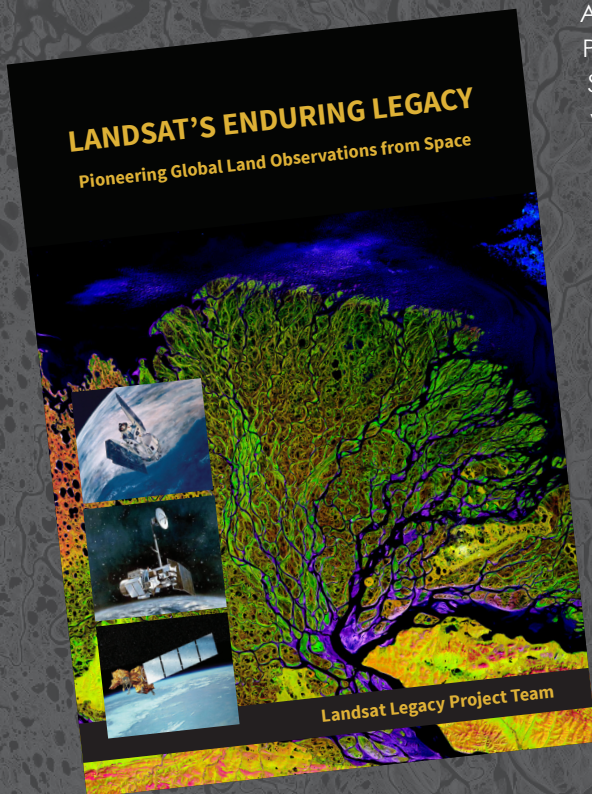
**Member discounts are not available on Amazon Kindle e-books,

[†]Students must order via the ASPRS Bookstore & a copy of your valid student ID must be submitted to be eligible for student pricing.



LANDSAT'S ENDURING LEGACY

PIONEERING GLOBAL LAND OBSERVATIONS FROM SPACE



After more than 15 years of research and writing, the Landsat Legacy Project Team is about to publish, in collaboration with the American Society for Photogrammetry and Remote Sensing (ASPRS), a seminal work on the nearly half-century of monitoring the Earth's lands with Landsat. Born of technologies that evolved from the Second World War, Landsat not only pioneered global land monitoring but in the process drove innovation in digital imaging technologies and encouraged development of global imagery archives. Access to this imagery led to early breakthroughs in natural resources assessments, particularly for agriculture, forestry, and geology. The technical Landsat remote sensing revolution was not simple or straightforward. Early conflicts between civilian and defense satellite remote sensing users gave way to disagreements over whether the Landsat system should be a public service or a private enterprise. The failed attempts to privatize Landsat nearly led to its demise. Only the combined engagement of civilian and defense organizations ultimately saved this pioneer satellite land monitoring program. With the emergence of 21st century Earth system science research, the full value of the Landsat concept and its continuous 45-year global archive has been recognized and embraced. Discussion of Landsat's future continues but its heritage will not be forgotten.

The pioneering satellite system's vital history is captured in this notable volume on Landsat's Enduring Legacy.

Landsat Legacy Project Team

Samuel N. Goward
Darrel L. Williams
Terry Arvidson
Laura E. P. Rocchio
James R. Irons
Carol A. Russell
Shaïda S. Johnston

Landsat's Enduring Legacy

Hardback, 2017, ISBN 1-57083-101-7
Student \$60*
Member \$80*
Non-member \$100*

* Plus shipping

Order online at
www.asprs.org/landsat